5-1999

The geochronology and geochemistry of the Bearhead Rhyolite, Jemez volcanic field, New Mexico

Leigh Justet
University of Nevada, Las Vegas

THE GEOCHRONOLOGY AND GEOCHEMISTRY OF THE BEARHEAD RHYOLITE, JEMEZ VOLCANIC FIELD, NEW MEXICO

by

Leigh Justet
Bachelor of Science
University of Nevada, Las Vegas
1996

A thesis submitted in partial fulfillment
of the requirements for the

Master of Science Degree
Department of Geoscience
College of Sciences

Graduate College
University of Nevada, Las Vegas
May 1999

ABSTRACT

The Geochronology and Geochemistry of the Bearhead Rhyolite, Jemez Volcanic Field, New Mexico

by

Leigh Justet

Dr. Terry L. Spell. Examination Committee Chair
Assistant Professor of Geoscience
University of Nevada. Las Vegas

Around 82% of mapped Bearhead Rhyolite (Main Cluster) and Peralta Tuff appears to have been derived from a relatively long-lived (~680 ka), large, shallow (≤ 10 km below Earth's surface) magma chamber that did not produce a caldera-forming eruption. Although volatile contents were great enough (~3 wt.% H_2O), no large-scale explosive eruptions occurred because magma may have been tectonically vented. The lack of systematic chemical variation within the Main Cluster with time during this ~680 ka interval may imply that erupted magmas were physically separated from each other by fault-formed cupolas in the roof of the magma chamber. These results are significant because Bearhead Rhyolite may represent a poorly documented style of silicic volcanism that may be more common than realized.

The remaining ~18% of mapped Bearhead Rhyolite is chemically and/or temporally distinct from the majority of Bearhead Rhyolite and is located in the southwest periphery of the field area.

TABLE OF CONTENTS

ABSTRACT iii

LIST OF TABLES viii

LIST OF FIGURES ix

ACKNOWLEDGEMENTS xii

CHAPTER 1 INTRODUCTION 1
The Problem 1
Objectives and Methods 2

CHAPTER 2 GEOLOGIC SETTING 4
Geology of the Jemez Volcanic Field 4
Geology of the Bearhead Rhyolite Dome Field 9

CHAPTER 3 PETROGRAPHY 15
Petrography of the Bearhead Rhyolite and Peralta Tuff Member 15
Felsic Phases 17
Mafic Phases 23
Accessory Phases 23
Matrix 27
Inferred Order of Crystallization 29

CHAPTER 4 GEOCHEMISTRY 30
Overview of Whole Rock Chemistry 31
Effect of Alteration on Bearhead Rhyolite Chemistry 31
Major Element Chemistry 34
Major Element Chemistry Versus Silica 34
Major Element Chemistry Versus Age 34
Trace Element Chemistry 35
Trace Element Chemistry Versus Niobium 35
Trace Element Chemistry Versus Age 39
REE/Chrondrite Diagrams 42
Main Cluster 42
Group 2 44
PN 44
Group 4 44

Group 5 45
Using Trace Element Ratios to Define Cogenetic Groups 45
Chemical Variations Within Sanidine Phenocrysts from the Peralta Tuff 47
Volatile Content of the Bearhead Rhyolite 47

CHAPTER 5 GEOCHRONOLOGY 50
Intercalibration of the $^{40}Ar/^{39}Ar$ Dating Laboratories 50
Data Treatment 51
Temporal Correlation of Bearhead Rhyolite Domes to the Peralta Tuff Member 58
Space and Time Trends in the Bearhead Rhyolite Dome Field 60

CHAPTER 6 INTERPRETATION 63
Not So Homogeneous Bearhead Rhyolite 63
The Isotopic Composition of the Crust and the Bearhead Rhyolite's Source 65
Was the Bearhead Rhyolite Derived from a Single Shallow Magma Chamber? 66
Crystal Fractionation 68
Trace Element Composition of the Upper Crust 70
Assimilation and Crystal Fractionation 74
AFC or Crystal Fractionation? 79
Was the Main Cluster Magma Chamber Derived from a Shallow Magma Chamber 79
The 680 ka Lifespan of the Bearhead Rhyolite Magma Chamber 81
Role of Tectonism in the Eruptive Style of the Bearhead Rhyolite 81
Explaining the Small Degree of Evolution in the Main Cluster's Chemistry 83
Is the Effusive Eruptive Style of the Bearhead Rhyolite Unusual? 84
Conclusions 85
Further Study 86

REFERENCES 88

APPENDIX A: SAMPLE LOCATIONS 97
Bearhead Rhyolite Sample Locations 97
Peralta Tuff Sample Locations 100

APPENDIX B: PETROGRAPHIC DESCRIPTIONS 102
Rhyolite 102
Vitrophyre 104
Tuff 106

APPENDIX C: WHOLE ROCK MAJOR AND TRACE ELEMENT DATA 108
Bearhead Rhyolite 108
Peralta Tuff 112

APPENDIX D: GEOCHEMICAL ANALYTICAL TECHNIQUES 115
Sample Collection 115
Bearhead Rhyolite 115
Peralta Tuff 115
Rock Powder Preparation 116
Bearhead Rhyolite 116
Peralta Tuff 116
Precision of Loss On Ignition Calculations 117
X-Ray Fluorescence Spectrometry 119
Instrumental Neutron Activation Analysis 120

APPENDIX E: PRECISION AND ACCURACY OF XRF ANALYSIS 122

APPENDIX F: PRECISION AND ACCURACY OF INA ANALYSIS 123

APPENDIX G: ION MICROPROBE DATA 124
Chemical Abundances of Glass Melt Inclusions in Quartz from the Peralta Tuff 124
Chemical Profiles of Sanidine from the Peralta Tuff 135

APPENDIX H: ELECTRON MICROPROBE ANALYTICAL TECHNIQUES 136
Electron Microprobe 136
Ion Microprobe 137

APPENDIX I: PRECISION AND ACCURACY OF ELECTRON MICROPROBE ANALYSIS 138

APPENDIX J: PRECISION AND ACCURACY OF ION MICROPROBE ANALYSIS 139

APPENDIX K: GEOCHRONOLOGICAL DATA 140
Geochronology of the Bearhead Rhyolite 140
Geochronology of the Bearhead Rhyolite from Previous Studies 146

APPENDIX L: $^{49}Ar/^{39}Ar$ ANALYTICAL TECHNIQUES 147
$^{40}Ar/^{39}Ar$ Sample Preparation 147
University of Houston Laboratory Methods 148
New Mexico Institute of Mining and Technology Laboratory Methods 149

APPENDIX M: PARTITION COEFFICIENTS FOR RHYOLITE 151

VITA 152

LIST OF TABLES

Table 1: Point count results for the Bearhead Rhyolite 18-19

Table 2: Summary of trace element trends with increasing Niobium by geochemical group 36

Table 3: Comparison of $^{40}Ar/^{39}Ar$ ages for sample 31B from the University of Houston and New Mexico Institute of Mining and Technology 52

Table 4: Summary of $^{40}Ar/^{39}Ar$ ages of the Bearhead Rhyolite 53

Table 5: Geochemistry of the Rabbit Mountain Rhyolite 64

Table 6: Sr, Nd, and Pb isotopic compositions of the Bearhead Rhyolite 67

Table 7: Bulk distribution coefficients for the Bearhead Rhyolite and Peralta Tuff 71

Table 8: Possible upper crustal reservoirs underlying the Jemez volcanic field 72-73

Table 9: AFC model for the Main Cluster using all trace elements 78

LIST OF FIGURES

Figure 1: Regional tectonic map showing the relationship between the Rio Grande rift, Jemez Lineament, and Jemez volcanic field 5

Figure 2: Schematic diagram depicting the spatial and temporal distribution of volcanic units found in the Jemez volcanic field 7

Figure 3: Geologic map of the study area in the south-central Jemez Mountains 10

Figure 4: Schematic stratigraphic column of Peralta Tuff samples collected for this study 12

Figure 5: Structural map of the study area 14

Figure 6: Map of Bearhead Rhyolite samples collected for this study 16

Figure 7a: Photomicrograph of sanidine and plagioclase 20

Figure 7b: Photomicrograph of sanidine, plagioclase, and biotite 20

Figure 7c: Photomicrograph of glomerocryst with accessory minerals 21

Figure 7d: Photomicrograph of oscillatory zoned sanidine 21

Figure 7e: Photomicrograph of embayed sanidine 22

Figure 7f: Photomicrograph of embayed quartz 24

Figure 7g: Photomicrograph of allanite, zircon, and magnetite 25

Figure 7h: Photomicrograph of glomerocryst with zircon 26

Figure 7i: Photomicrograph of apatite in biotite 26

Figure 7j: Photomicrograph of plagioclase- and biotite-rich lithic fragment... 28

Figure 8: Photomicrograph of biotite in embayed quartz 28

Figure 9: Total alkalis versus silica classification diagram 32

Figure 10: Trace element abundances versus Niobium: Part I 37

Figure 11: Trace element abundances versus Niobium: Part II 38

Figure 12: Trace element abundances versus age: Part I 40

Figure 13: Trace element abundances versus age: Part II 41

Figure 14: REE/Chondrite diagrams 43

Figure 15: Trace element ratio plots for defining petrogenetic groups 46

Figure 16: SEM image of unzoned sanidine from the Peralta Tuff: Part I 48

Figure 17: SEM image of unzoned sanidine from the Peralta Tuff: Part II 48

Figure 18: SEM image of zoned sanidine from the Peralta Tuff 49

Figure 19: Probability distribution diagrams for the Bearhead Rhyolite: Part I 55

Figure 20: Probability distribution diagrams for the Bearhead Rhyolite: Part II 56

Figure 21: Probability distribution diagrams for the Bearhead Rhyolite: Part III 57

Figure 22: Diagram comparing the $^{40}Ar/^{39}Ar$ ages of the Peralta Tuff and chemically related Bearhead Rhyolite 59

Figure 23: Probability distribution diagram depicting the eruptive periodicity of the Bearhead Rhyolite 61

Figure 24: Map of field area depicting time and space relationships between age-constrained chemical groups of the Bearhead Rhyolite 62

Figure 25: Pure fractional crystallization model of the Main Cluster 69

Figure 26: Map showing sample locations of upper crustal proxies..... 75

Figure 27: AFC model of the Main Cluster..... 76

Figure 28: Map showing spatial distribution of K/Ar hydrothermal Illite ages..... 80

Figure 29: Comparison of the water content of the Bearhead Rhyolite and Bandelier Tuff..... 82

ACKNOWLEDGEMENTS

I would like to thank the following people and institutions who, in various ways, helped me through the course of the project: Franchesca Cinacola and Jason Smith who helped prepare samples for chemical and petrographic analysis; the Bernada E. French Scholarship which funded field work and thin section preparation; the DoE EPSCoR/WISE Young Scholarship which funded research in Spring 1998; the Barrick Fellowship which funded research from Fall 1998 to Spring 1999; Dr. Frederick Bachhuber for making the Barrick Fellowship possible; Dr. Margaret Rees for funding me from Spring 1997 to Summer 1998 and for her role as mentor; committee members Dr.s Rodney Metcalf, Eugene Smith, Kathleen Robins, and Philip Kyle for their advice on the content and organization of my thesis; Dr. Gary Smith for volunteering to help me in my collection of Peralta Tuff samples and who kept me up to date on his ongoing work in the Jemez Mountains; Dr. William McIntosh for dating the rhyolite samples with little forewarning; Dr. Nelia Dunbar who hosted me during my visit to her microprobe lab at New Mexico Tech and who patiently stepped me through the probe process; Dr. Terry Spell, advisor extraordinaire, patient proof reader, and bearer of the MFT™; Dr. Clay Crow my sounding board and benevolent land lord; Jack the Dog for helping me maintain perspective; and, of course, Mom and Dad for doing what parents do.

CHAPTER 1

INTRODUCTION

The Problem

The most destructive volcanic eruptions known are associated with continental caldera forming event in which 100s to 1,000s km^3 of silicic magma are rapidly evacuated from upper crustal magma chambers. Because the volume of material erupted, such events imply/require a magma chamber as large as 10-15 km in diameter. Calderas and regionally extensive ignimbrites associated with them are easily recognized geologic features. Whereas caldera forming systems have been extensively studied, an alternate style of eruptions from large, shallow silicic magma chambers, intermittent venting of relatively small volumes of magma (a few km^3 per eruption) over extended timescales (100s ka) during which mo large caldera forming eruptions occur remains poorly documented. Only two examples of this end-member style of eruptive behavior have been described, the Coso volcanic field, California (Bacon et al., 1984) and the Taylor Creek Rhyolite, Mogollon-Datil volcanic field, New Mexico (Duffield and du Bray, 1990; Duffield and Dalrymple, 1990).

The high silica Bearhead Rhyolite/Peralta Tuff from the Jemez volcanic field, New Mexico, may represent another example of this poorly documented eruptive style

for the following reasons. First, reconnaissance geochemistry suggests that the Bearhead Rhyolite is chemically homogeneous (Guilbeau and Kudo, 1985; Ellisor, 1995). Second, initial $^{40}Ar/^{39}Ar$ dating (McIntosh and Quade, 1995; McIntosh, unpublished data 1995) suggests that the Bearhead Rhyolite was erupted over a relatively brief 200 ka interval. Third, Bearhead Rhyolite domes are distributed over a ~630 km^2 area (similar in area to calderas in continental silicic magma systems). The observations of chemically homogeneous (i.e., cogenetic) rhyolites erupted over a large (caldera-sized) area during a brief interval of time suggests that the Bearhead Rhyolite's source was a large, shallow, silicic magma chamber.

In cases where large shallow magma chambers do not produce caldera-forming eruptions an explanation must be sought to account for the effusive nature of the eruption. One possibility is that magma was leaked off by fault zones that intersect the magma chamber before it could explosively erupt. Another is that volatile contents were too low to be capable of producing a caldera-forming eruption. A final possibility is that such magmas were, in fact, not erupted from a single, large magma chamber, but from several smaller magma chambers that were not large enough to produce an explosive, caldera-forming eruption.

Objectives and Methods

This study has two main objectives: (1) to determine whether the Bearhead Rhyolite represents a cogenetic series of eruptions derived from a single magma chamber, and (2) if so, to examine the possibility that the Bearhead Rhyolite was vented by faults before it could explosively erupt. To test the single magma chamber hypothesis, this

study presents detailed geochemical, geochronologic, and petrographic data. If the Bearhead Rhyolite is chemically heterogeneous and/or was erupted over a large interval of time (> 1Ma), then more than one magma chamber may have been present or magma was injected into a single magma chamber. If the Bearhead Rhyolite appears to represent a cogenetic series and was erupted over a short interval of time, then the rhyolite may have been derived from a single magma chamber.

To test the tectonic venting versus volatile poor hypothesis it is necessary to examine the volatile content of the Bearhead Rhyolite. If the Bearhead Rhyolite was volatile rich then faulting may be a factor in the rhyolite's effusive eruption. If the Bearhead Rhyolite is volatile poor then the composition of the rhyolite may have been such that caldera-forming eruptions were not possible.

CHAPTER 2

GEOLOGIC SETTING

Geology of the Jemez Volcanic Field

Late Cenozoic tectonic and volcanic activity in New Mexico is concentrated along the Jemez Lineament and Rio Grande rift. The Jemez Lineament is a northeast trending array of volcanic centers that reaches from southeast Arizona to northeast New Mexico (Smith and Bailey, 1968; Aldrich, 1986). These volcanic centers correspond to a boundary that separates the relatively stable Colorado Plateau from the more actively extending Basin and Range Province to the east and Rio Grande rift region to the south and west (Mayo, 1958; Suppe et al., 1975; Laughlin et al., 1976; Olsen et al., 1987).

The Rio Grande rift is located in a region that experienced multiple episodes of deformation in the Paleozoic and early Mesozoic (Doell et al., 1968; Aldrich, 1986). The rift comprises a series of en-echelon sedimentary basins produced by extension of Precambrian basement and overlying Upper Paleozoic sedimentary strata (Doell et al., 1968; Aldrich, 1986). The Jemez volcanic field lies on the western flank of the Española Basin, at the intersection of the Rio Grande rift with the Jemez Lineament (Figure 1). The volcanic field straddles the west-bounding faults of the Española Basin; the Cañada de Cochiti and Pajarito fault zones.

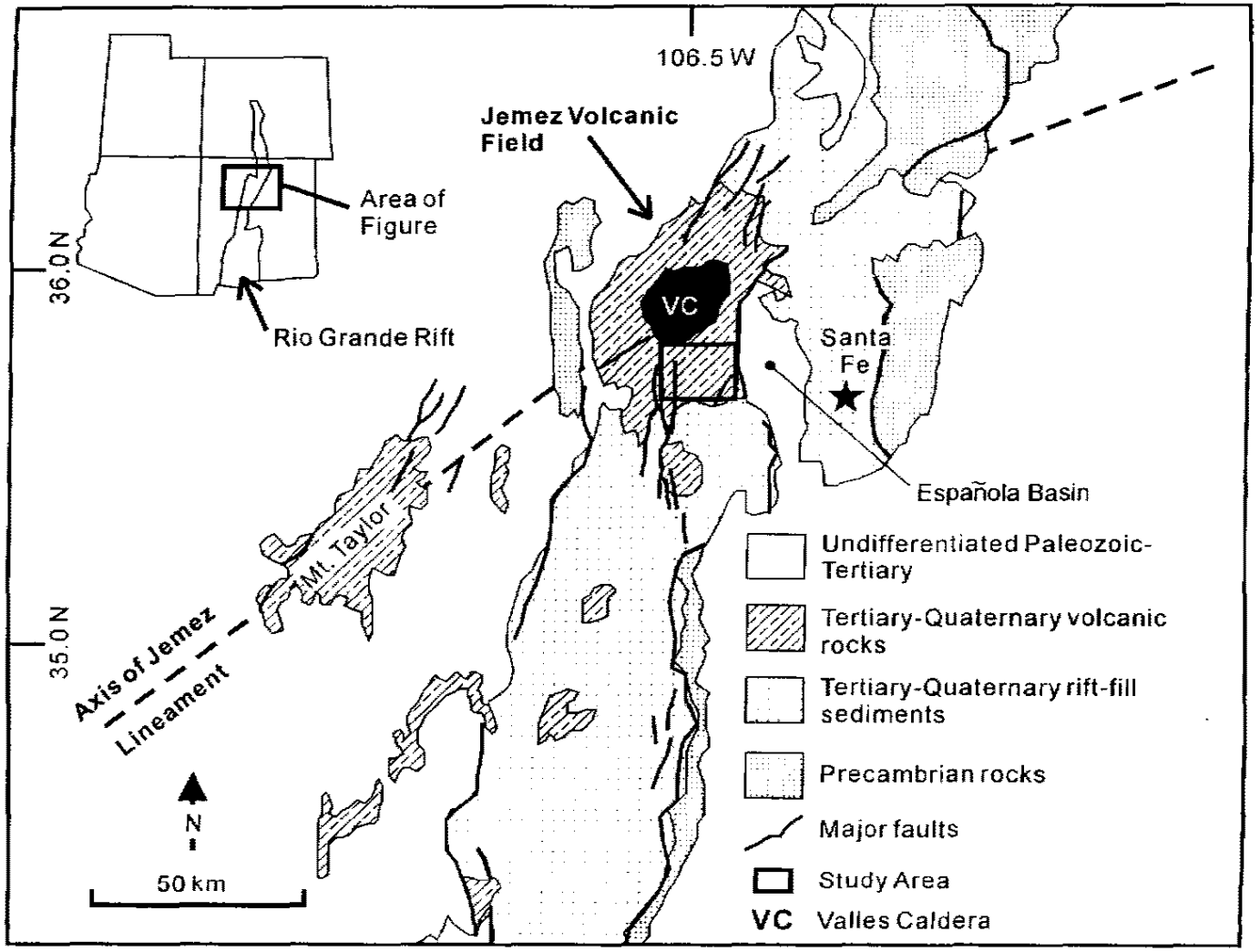

Figure 1. Regional tectonic map showing the relationship between the Rio Grande rift, Jemez Lineament, and Jemez Volcanic Field (after Baldridge et al., 1983; Gardner and Goff, 1984; Self et al., 1986).

Small-volume volcanic activity in the Jemez volcanic field began ~16.5 Ma (K/Ar dates) when alkali basalt was erupted in the Española Basin during deposition of rift-fill sediments of the Santa Fe Group (Figure 2) (Gardner and Goff, 1984). Between ~13 and ~6 Ma (K/Ar dates), coincident with extension along the Cañada de Cochiti fault zone, a large Paliza Canyon andesite-dominated volcanic ridge formed on the basin shoulder that accounts for approximately half the volume of the Jemez volcanic field. Andesitic volcanism of the Paliza Canyon Formation was accompanied by eruption of minor volumes of olivine tholeiite basalt, dacite, Canovas Canyon Rhyolite, and Bearhead Rhyolite (Gardner et al., 1986). These volcanic units comprise the Keres Group (Figure 2) (Smith et al., 1961; Smith and Bailey, 1968; Bailey et al., 1969; Smith et al., 1970). The Paliza Canyon Formation was erupted between ~13 and ~6 Ma (K/Ar dates) while the Canovas Canyon Rhyolite (~12.5 to ~ 6 Ma, K/Ar dates) and Bearhead Rhyolite (~7 to 6.7 Ma, K/Ar dates) represent a continuum of high-silica rhyolite volcanism that range across a similar time interval. The boundary between the Canovas Canyon Rhyolite and Bearhead Rhyolite is arbitrarily marked by the stratigraphically prominent Peralta Tuff Member of the Bearhead Rhyolite (Gardner et al., 1986). Volcanic rocks of the Keres Group are exposed in the southern part of the volcanic field where they have not been eroded or buried by younger volcanic eruptions and/or alluvium shed into the Española Basin (Gardner et al., 1986; Lavine et al., 1996).

Volcanic rocks of the Polvadera Group are exposed in the northern part of the Jemez volcanic field. The Polvadera Group is subdivided into the Lobato Basalt,

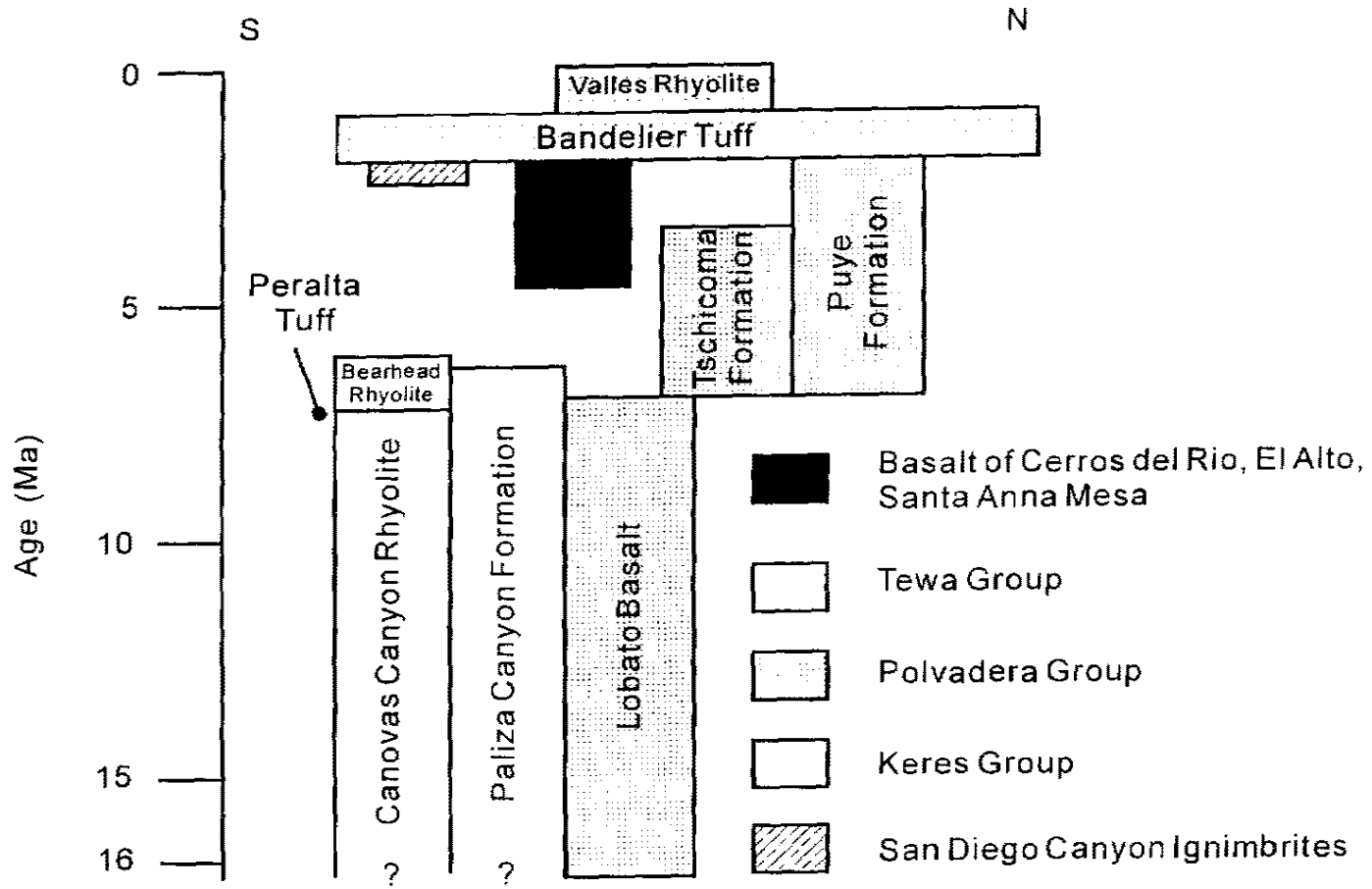

Figure 2. Schematic diagram depicting the temporal and spatial distribution of units found in the Jemez volcanic field (modified from Gardner and Goff, 1984; Gardner, 1985).

Tschicoma Formation, and Puye Formation (Figure 2) (Bailey et al., 1969). The Lobato Basalt (~11 to ~8 Ma, K/Ar dates) represents the earliest activity of the Polvadera Group and was accompanied by eruptions of andesite and dacite from ~8 to ~7 Ma (K/Ar dates) (Goff et al., 1989).

Large volumes of andesite, dacite, and rhyodacite of the Tschicoma Formation were erupted between 6.9 and 2.2 Ma (K/Ar dates) during a lull in tectonic activity (Gardner et al., 1986; Goff et al., 1989). This pulse of volcanism in the north and northeast coincided with the last of Keres Group volcanism in the south. By 4 to 2 Ma (K/Ar dates), the predominantly rhyolitic magmas erupted around the northern, eastern, and southern margins of the volcanic field (Smith et al., 1970; Baldridge, 1979; Turbeville et al., 1989) and were accompanied by small-volume basaltic volcanism of Santa Anna Mesa (Dunker et al., 1991; Heikoop et al., in prep).

The rhyolitic Tewa Group is the youngest volcanic suite in the Jemez volcanic field, ranging from ~1.85 ($^{40}Ar/^{39}Ar$ dates) Ma to 60 ka (^{14}C, electron spin resonance, and thermoluminescence dating), and unconformably overlies or intrudes most older units (Gardner et al., 1986; Izett and Obradovich, 1994; Reneau et al., 1996; Spell et al., 1996). During this interval of the large-volume (250 to 400 km^3) Bandelier Tuff eruptions, the Toledo caldera and, later, the Valles caldera and its resurgent dome were formed. The Tewa Group contains the volumetrically dominant Bandelier Tuff (consisting of two events at ~1.6 and ~1.2 Ma) and the Valles Rhyolite Formation (Figure 2) (< 1.21 Ma, $^{40}Ar/^{39}Ar$ dates) (Bailey et al., 1969).

Geology of the Bearhead Rhyolite Dome Field

The Bearhead Rhyolite dome field, located in the southeastern portion of the Jemez volcanic field, is distributed across a ~300 km^2 area as a series of 23 domes, composite domes (at Bearhead Peak), flows, shallow intrusions (e.g., eroded volcanic plugs and conduits to domes), and the volumetrically dominant Peralta Tuff (Figures 1 and 3). Bearhead Rhyolite domes appear to be concentrated in the central portion of the field area and appear to extend in a northeast-southwest trend. Exposures of the Peralta Tuff are primarily concentrated in the southeastern portion of the field area in Peralta, Bland, and Cochiti Canyons where they have been preserved in the Bearhead Basin but are nearly as widespread as the Bearhead Rhyolite (G.A. Smith, personal communication, 1998). Remnanats of pyroclastic-flow aprons and tuff rings are found around most of the Bearhead Rhyolite vents and likely represent local accumulations of pyroclastic debris from each dome eruption (Bailey et al., 1969; Smith et al., 1991; Gay and Smith, 1993; G.A. Smith, personal communication, 1998). Distribution, thickness, and grain size of the Peralta Tuff fall deposits imply that energetic sub-plinian to low-rank plinian eruptions were associated with the emplacement of the ignimbrites (G.A. Smith, personal communication, 1998).

Smith et al. (1991) and Gay and Smith (1993) have studied a section of Peralta Tuff in Peralta and Colle Canyons that represents the upper ~50% of Bearhead Basin fill in that area. This section of Peralta Tuff contains a record of 38 eruption episodes. Each eruptive unit is composed of pyroclastic fall, and/or surge deposits. Only about a dozen

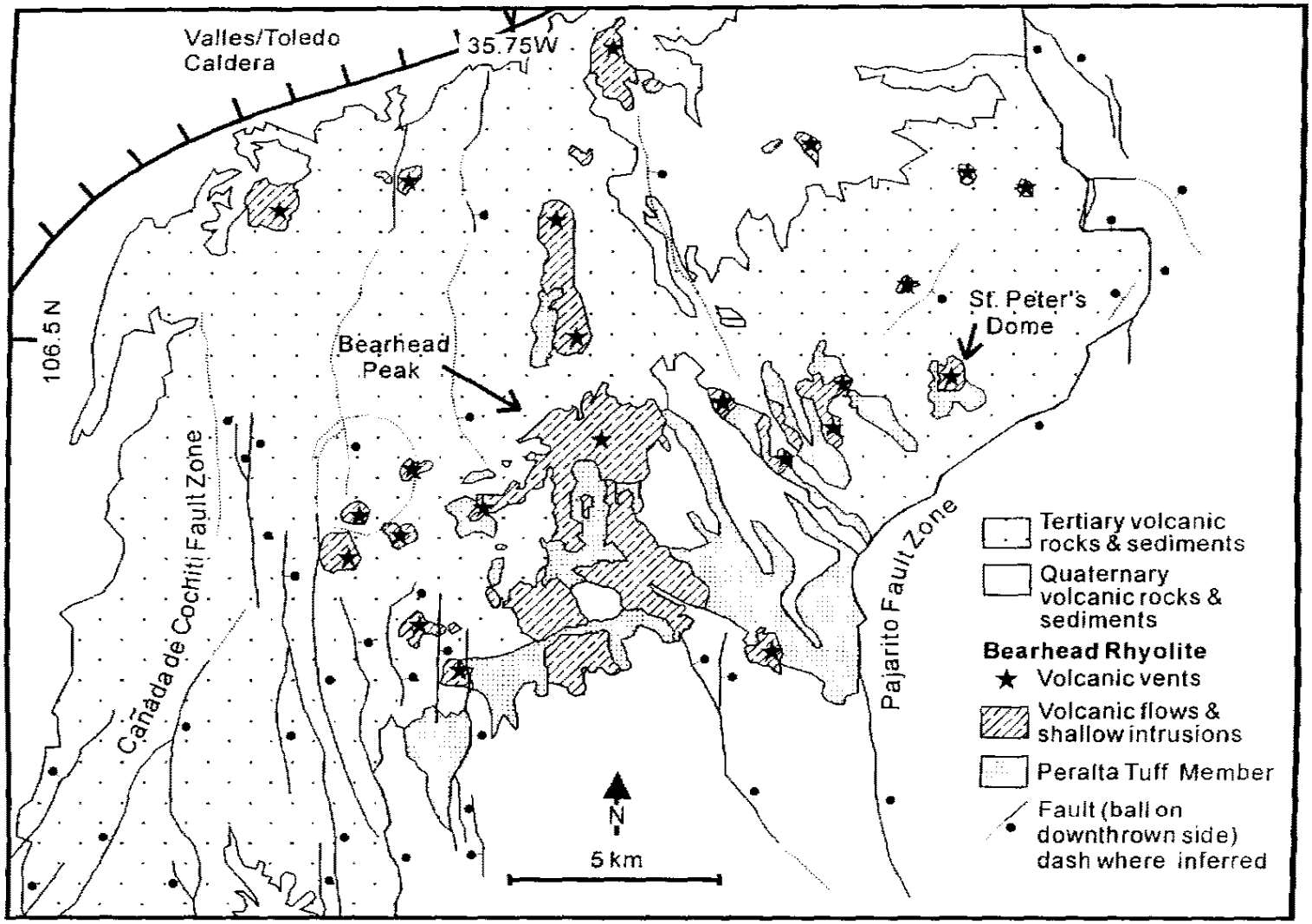

Figure 3. Geologic map of the study area in the south-central Jemez Mountains (after Smith et al., 1970).

of these eruptive units are represented by flow and/or surge deposits; the remainder are fall deposits (Smith et al., 1991; Gay and Smith, 1993; G.A. Smith, personal communication, 1998). Seven eruptive units were informally defined by Smith et al. (1991) and Gay and Smith (1993) in the Peralta/Colle Canyon area that were sampled during this study (Figure 4). These units have been named, from stratigraphically lowest to highest: (1) Tuff of West Mesa; (2) Tuff of Lower Peralta Canyon; (3) Tuff of Bearjump; (4) Tuff of Albemarle; (5) Tuff of Colle Canyon; (6) Tuff of Tent Rocks; and (7) Tuff of Cañada Camada. Gay and Smith (1993) suggest that the Tuff of Lower Peralta Canyon and West Mesa were erupted at the same time from different vents under phreatomagmatic and magmatic eruptive conditions, respectively. The Tuff of Lower Peralta Canyon was emplaced at temperatures up to 300° C based on paleomagnetic data whereas the Tuff of West Mesa was emplaced at or near 600° C (Gay and Smith, 1996). The Peralta Tuff is overlain by volcaniclastic sedimentary rocks that overlie the Keres Group and correlative volcaniclastic sediment south of the Jemez volcanic field known as the Cochiti Formation (Smith and Lavine, 1996).

The dome field also lies at the intersection of two fault zones that are related to the Rio Grande rift and Jemez Lineament (Gardner, 1985; Smith et al., 1970); the Cañada de Cochiti and Pajarito fault zone, respectively. Most faults in the north-striking Cañada de Cochiti fault zone are normal faults with a down-to-the-east sense of displacement and greater than 500 m of offset. The faults are concentrated in the western portion of the dome field. The Cañada de Cochiti fault zone is thought to have been active during Keres Group time because Keres deposits are cut by the faults and thicken to the east

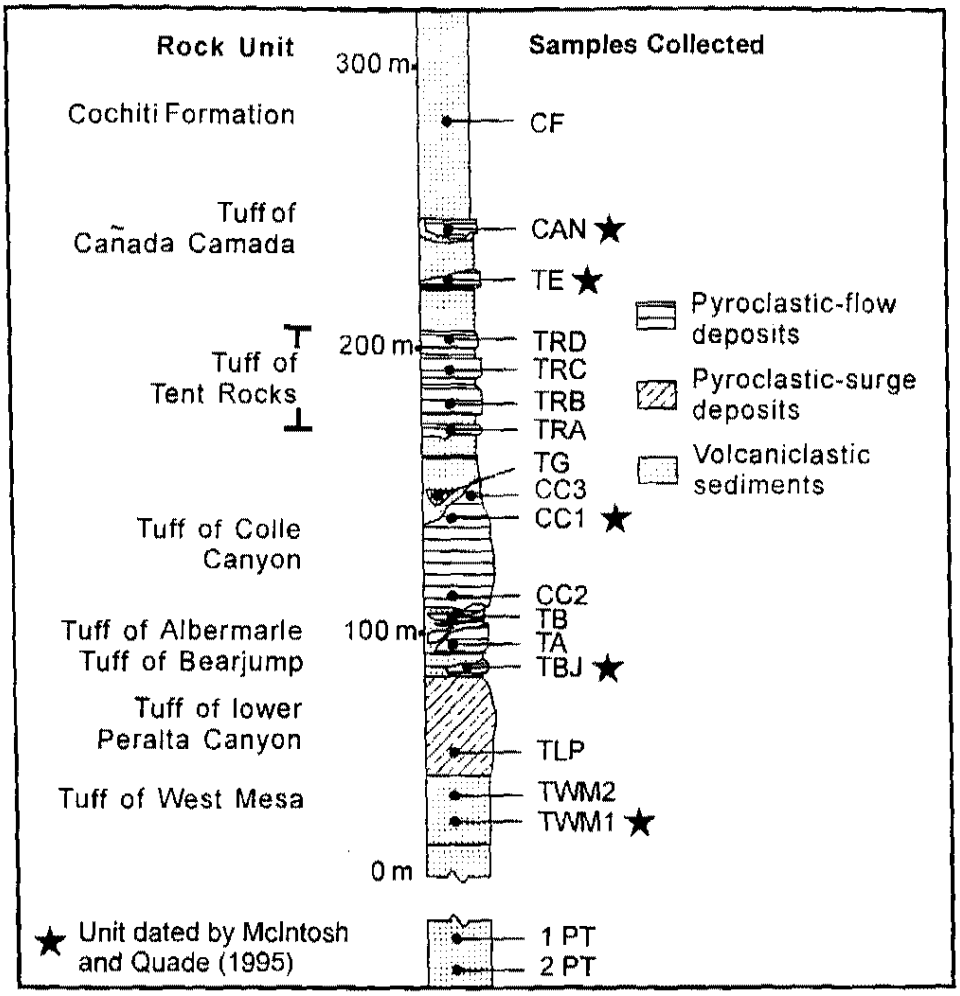

Figure 4. Schematic stratigraphic column of Peralta Tuff samples collected for this study. Stratigraphy worked out by G.A. Smith, R.J. Abitz, and K.R. Gay (1988-1994).

across the fault zone (Gardner, 1985). The Bearhead Rhyolite appears to be intruded along these faults but is seldom faulted itself (except domes corresponding to samples CY, CYF, and GBR of this study) (Smith and Kuhle, 1998).

The segment of the Pajarito fault zone located in the southeastern portion of the dome field is characterized by northeast-striking normal faults (Griggs, 1964; Smith et al., 1970; Golombek, 1981). Faults of this segment are predominantly down-to-the-east and show evidence of episodic or multiple phases of motion (Griggs, 1964). Gardner (1985) suggested that this segment of the fault zone became active around 5 Ma, implying that fault activity is at least as old as the lower Santa Fe Group. From this observation Gardner (1985) further suggested that the western margin of the Española Basin shifted from the Cañada de Cochiti fault zone to the Pajarito fault zone ~6-5 Ma (see also Manley, 1976, 1979; Golombek 1981, 1983; Golombek et al., 1983).

The overlapping fault geometries of the Cañada de Cochiti and Pajarito fault zones resulted in rectilinear fault blocks that underwent differential subsidence during late Miocene rhyolitic volcanism (Figure 5) (Smith and Kuhle, 1998). The Bearhead Basin, one of these subsidence features, is a west-tilted basin that accumulated at least 0.7 km of lava, tuff, and coeval volcaniclastic rocks between ~7 to 6.7 Ma (Smith and Kuhle, 1998). The basin occupies a 7.5 by 6 km area that extends from the intrusive rocks of the Bland Mining District in the north and Peralta Canyon in the west to Bland Canyon in the east and the Española Basin in the south. Smith and Kuhle (1998) estimate >1 km of footwall uplift along the northern boundary of the basin and suggest that this large amount of uplift explains the anomalously low structural level of exposure in this portion of the Jemez volcanic field.

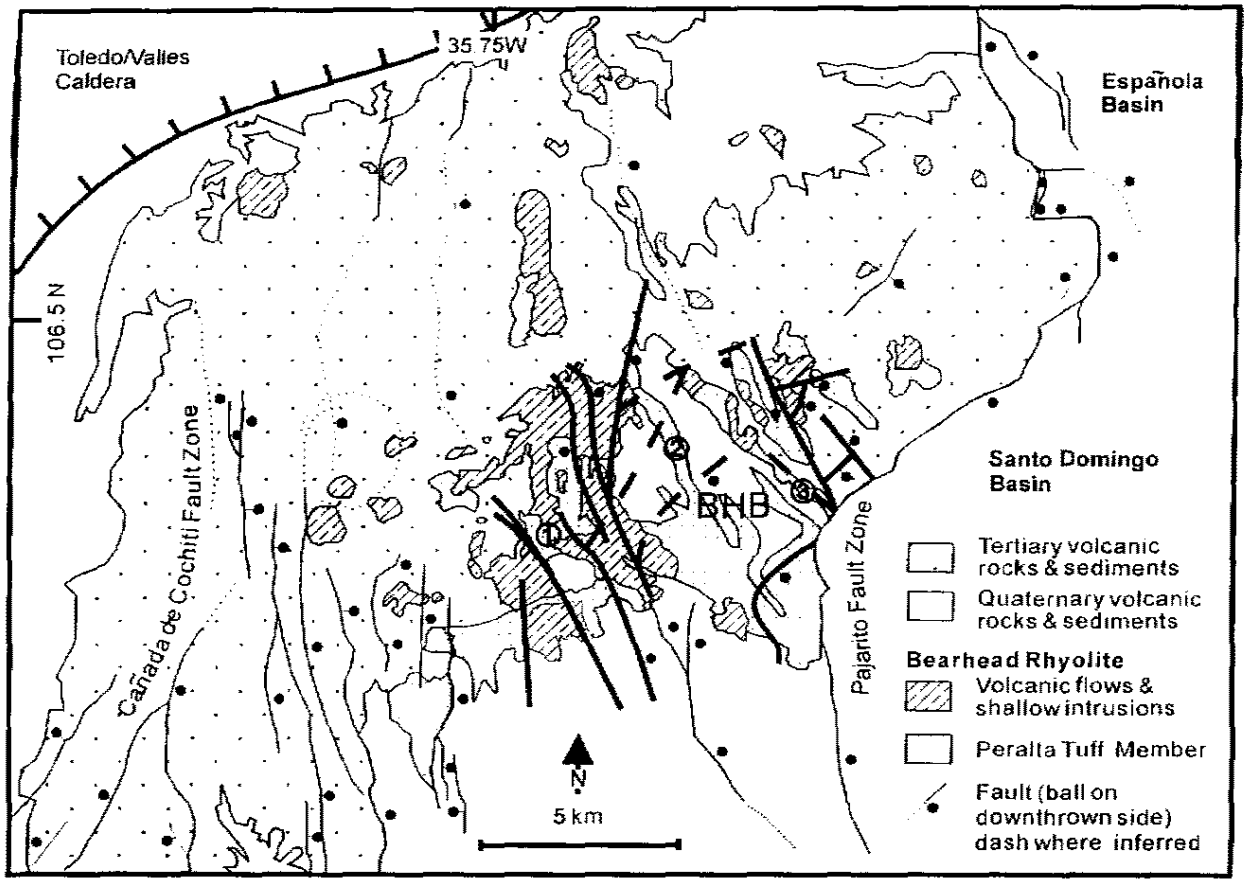

Figure 5. Structural map of the study area in the south-central Jemez Mountains. Thin fault lines based on the mapping of Smith et al. (1970). Thick fault lines based on the mapping of Smith and Kuhle (unpub.) depict the geometry of Bearhead Basin (BHB). (1) Peralta Canyon, (2) Colle Canyon, (3) Bland Canyon.

CHAPTER 3

PETROGRAPHY

A total of 43 thin sections were examined that represent all Bearhead Rhyolite domes (28), flows (4), and tuff (1) dated in this study, and 10 of the 11 mapped units from the Peralta Tuff, five of which were dated by McIntosh and Quade (1995) (Figures 4 and 6) (For sample locations see Appendix A). Approximately 600 points were counted per thin section. Detailed petrographic descriptions are presented in Appendix B.

Petrography of the Bearhead Rhyolite and Peralta Tuff Member

The Bearhead Rhyolite is massive to continuously flow banded, and includes vitrophyre and pumiceous rhyolite (31A and ERP2). The Peralta Tuff Member of the Bearhead Rhyolite is composed of primary and reworked pyroclastic fall deposits, pyroclastic flow deposits, distal fall deposits, and surge deposits. Most Bearhead Rhyolite units are aphyric to sparsely porpyritic (containing an average of 4 ± 3% phenocrysts). Samples SH1 and SH2 are aphanitic whereas phenocryst-rich domes and flows in the far northwest and southwest of the field area (CY, CYF, NECY, PN, and SHC) contain a significantly higher average of 21 ± 4% phenocrysts. Based on a ≤ 5%

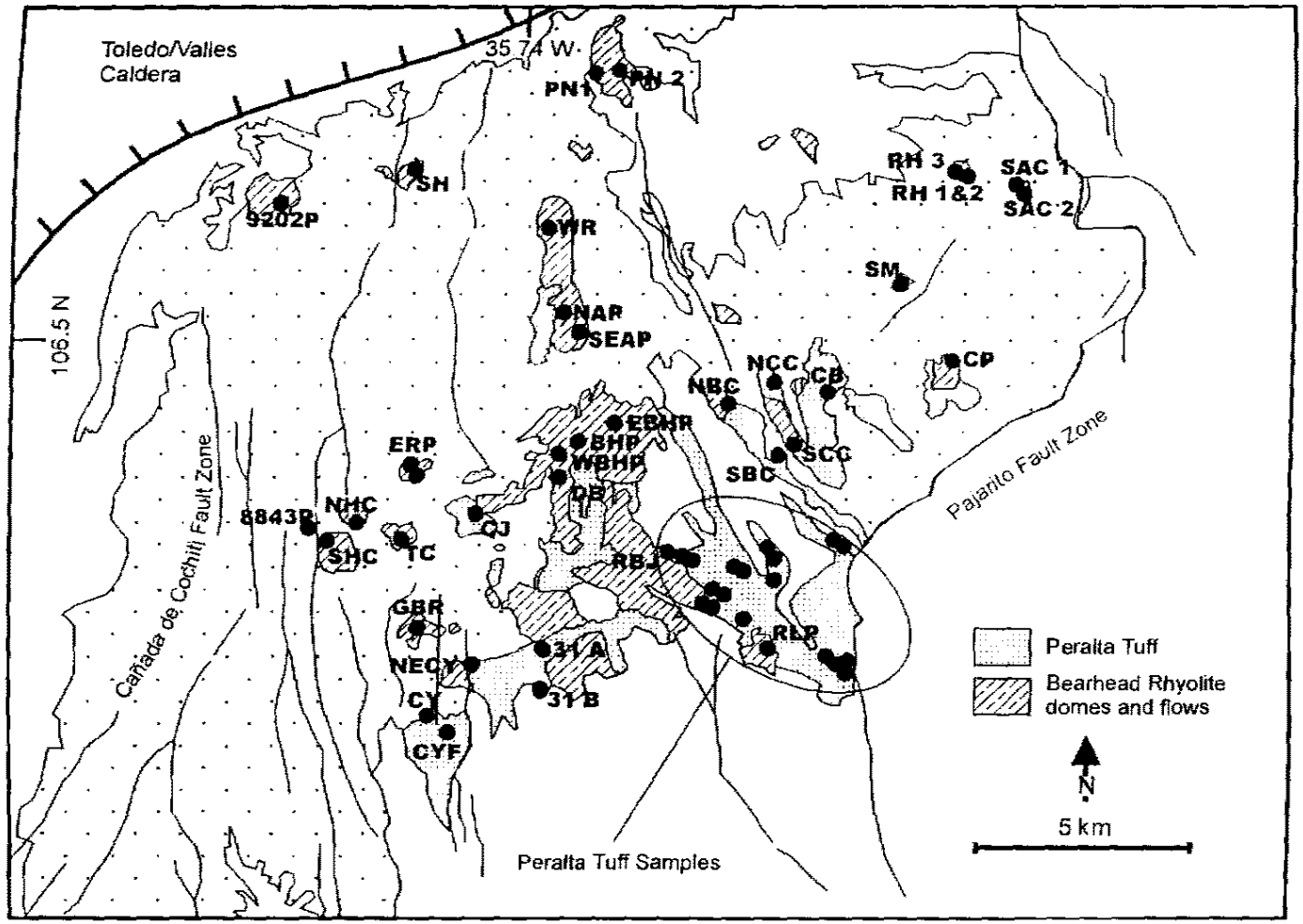

Figure 6. Map of Bearhead Rhyolite samples collected for this study. Peralta Tuff sample locations lie within the oval. Map after Smith et al. (1970).

variation observed in 13 sets of duplicate thin sections, there appears to be little variation in phenocryst content within individual dome and flow units. A summary of the point count results is given in Table 1.

Felsic Phases

Quartz, sanidine, and plagioclase occur together as individual phenocrysts, phenocryst fragments, and poly- and mono-glomerocrysts. Exceptions are samples CC3 and NCC which contain no sanidine and samples PN, TE, and TRD which do not contain plagioclase. Felsic phases comprise 81 to 100% of all phenocryst assemblages. The relative amounts of each phase vary significantly from sample to sample. Most samples contain 2 to 8 times more feldspar than quartz. Samples CYF, RH2, SM, SBC, CP, WBHP, 9202P1, NBC and NHC, however, contain equal amounts of feldspar and quartz while CAN, PN, TRD, and SAC contain 2 to 5 times more quartz than feldspar.

Most felsic phenocrysts range from < 0.1 to 2.5 mm. Within a single thin section, phenocrysts and phenocryst fragments are euhedral to anhedral, and are commonly embayed. Sanidine may be untwinned, or show carlsbad twins (Figure 7a), baveno twins (Figure 7b), oscillatory zoning along phenocryst rims (Figure 7c), and continuous zoning from core to rim (Figure 7d). Many samples contain embayed sanidine (31A, CB, CP, CY, DB, ERP2, GBR, CYF, EBHP, NBC, RBJ3, BHP, CJ, NAP, SAC, CAN, TRB, and RH2) (Figure 7e). Less commonly, plagioclase is moderately embayed, and exhibits polysynthetic twins, carlsbad twins, discontinuous, continuous, and oscillatory zoning

Table 1. Point Count Results for the Bearhead Rhyolite

Sample	Rock Type	% Phenocrysts						% Matrix				
		Qtz	San	Plag	Bio	Mag	Zirc	Total Matrix	Devitrified	Undevitrified	Vesicles	Lithics
CAN	pumice	2.06	0.19	0.38	0	0.19	0	97.19	14.86	85.14	12.34	NA
TE	pumice	0.74	0.74	0	0	0	0	98.52	36.33	63.67	11	NA
TRD	pumice	1.04	0.21	0	0	0	0	98.75	0	100	19.16	NA
TRC	pumice	0.17	0.69	0.69	0	0	0	98.45	0	100	NA	NA
TRB	pumice	0.74	0.98	0.49	0.25	0	0	97.54	12.59	87.41	41.03	NA
TG	pumice	0.28	0.28	0.28	0	0	0	99.15	6.53	93.47	27.25	NA
CC 3	pumice	0	0	0.2	0	0	0	99.8	0	100	19.09	NA
CC 2	pumice	0.53	0.26	0.53	0	0	0	98.68	10.43	89.57	NA	NA
TB	pumice	0	0.49	0.97	0	0	0	98.54	4.94	95.06	17.47	NA
TA	pumice	0	0.57	0.38	0.19	0	0	98.85	0	100	7.86	NA
1 PT	pumice	0	0.32	0.48	0	0	0	99.2	91.9	8.1	NA	NA
9202P 1	rhyolite	0.58	0.19	0.58	0	0	0	98.64	100	0	NA	NA
9202P 2	rhyolite	0	0.4	1.01	0	0	0	98.59	100	0	NA	NA
CB	rhyolite	1.9	2.06	1.12	0	0.16	0	94.94	100	0	NA	NA
CP	rhyolite	2.04	0.93	1.49	0.19	0.19	0	95.17	0	100	NA	NA
CY	rhyolite	7.78	5.63	5.79	0.5	0	0	80.3	0	100	NA	NA
CYF	rhyolite	7.49	5.23	2.22	0.79	0	0	84.31	100	0	NA	NA
DB	rhyolite	0	1.98	0.66	0	0	0	94.88	100	0	NA	1.31
ERP 2	rhyolite	0.16	0.97	1.46	0.16	0	0	97.73	18.77	81.23	NA	NA
GBR	rhyolite	0.32	0.96	0.96	0.64	0.16	0	96.96	100	0	NA	NA
NBC	rhyolite	3.05	1.97	2.15	0.18	0	0	92.65	100	0	NA	NA
NCC	rhyolite	0.16	0	1.13	0	0	0	98.71	100	0	NA	NA
NHC	rhyolite	1.57	0.79	0.47	0	0	0	97.17	100	0	NA	NA
NECY	rhyolite	1.07	1.07	15	3.04	0.54	0	79.29	86.94	0	NA	NA
PN	rhyolite	14.24	5.19	0	0	0.67	0	79.9	100	0	NA	NA
RBJ 3	rhyolite	0.49	1.8	0.82	0	0	0	96.9	73.52	26.48	NA	NA
RH 2	rhyolite	3.68	2.51	1	0.17	0	0	92.64	100	0	NA	NA
RPL 1	rhyolite	0.91	3.32	1.66	0.15	0	0	93.96	100	0	NA	NA
SH 1	rhyolite	0	0	0	0	0	0	100	99.84	0	NA	NA

Table 1. Point Count Results for the Bearhead Rhyolite (cont.)

	Rock	% Phenocrysts						% Matrix				
Sample	Type	Qtz	San	Plag	Bio	Mag	Zirc	Total Matrix	Devitrified	Undevitrified	Vesicles	Lithics
SH 2	rhyolite	0	0	0	0.35	0	0.17	99.48	99.83	0	NA	NA
SHC	rhyolite	0	11.6	12.38	1.88	0.94	0	73.2	100	0	NA	NA
SM	rhyolite	3.01	2.22	0.95	0.48	0	0	93.34	100	0	NA	NA
BHP	vitrophere	1.56	1.39	1.39	0	0	0	95.67	0	100	NA	NA
CJ	vitrophere	0.9	1.2	1.05	0	0	0	96.84	0	100	NA	NA
EBHP	vitrophere	3	3	2	0	0	0	92	0	100	NA	NA
NAP	vitrophere	2.85	2.01	3.35	1.34	0	0	90.45	33.7	66.3	NA	NA
NBC	rhyolite	3.05	1.97	2.15	0.18	0	0	92.65	100	0	NA	NA
RBJ 1	vitrophere	2.6	2.6	0.97	0	0	0	93.83	100	0	0	0
RH 3	vitrophere	3.26	3.54	1.27	0.28	0	0	91.5	26.93	73.07	NA	NA
SAC 1	vitrophere	4.64	0.52	1.72	0.52	0	0	91.41	11.87	86.83	NA	0.51
SBC	vitrophere	0.99	0.33	0.82	0	0	0	97.87	0.17	99.83	NA	NA
TC 2	vitrophere	2.21	2.72	0.85	0.17	0	0	94.05	19.89	80.11	0	0.17
WBHP	vitrophere	2.33	1.25	1.61	0	0	0	94.81	7.92	92.08	NA	NA

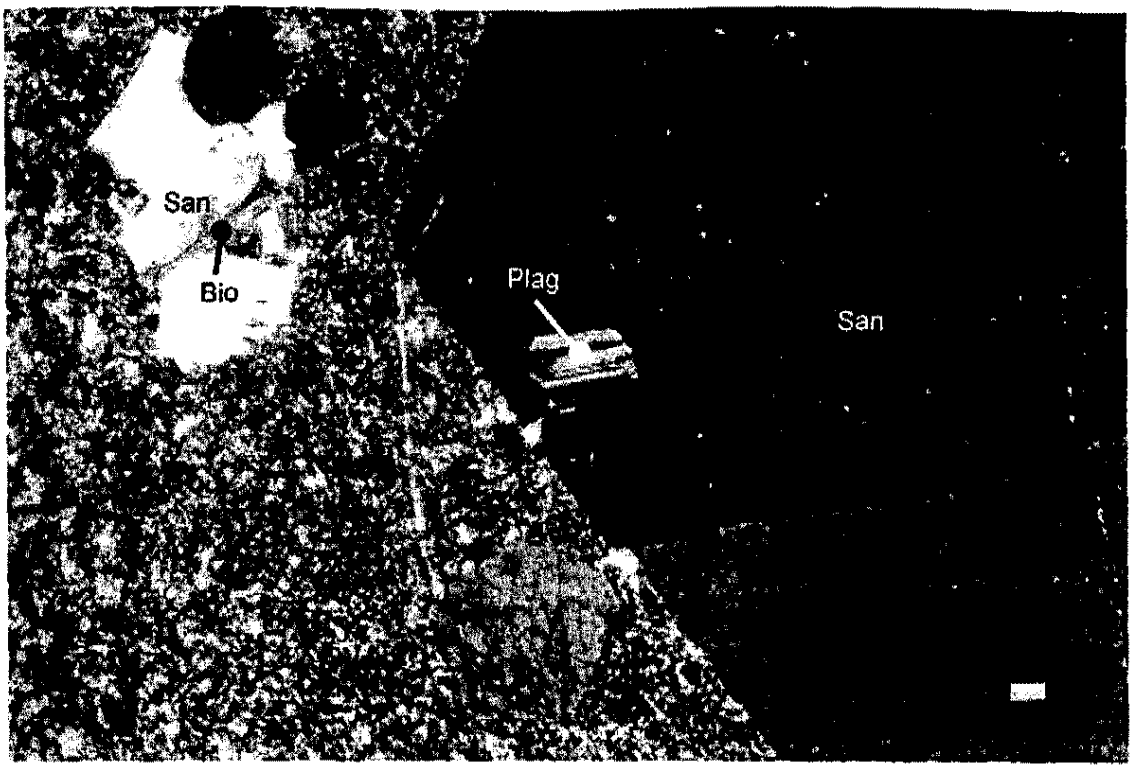

Figure 7a. Sample NECY. Euhedral, carlsbad twinned sanidine overgrowing polysynthetic twinned plagioclase. Carlsbad twinned plagioclase overgrown on biotite. Cross polarized light, bar = 10 μm.

Figure 7b. Sample EBHP. Baveno twinned sanidine overgrowing polysynthetic and carlsbad twinned, zoned plagioclase. Plagioclase overgrown on biotite. Cross polarized light, bar = 10 μm.

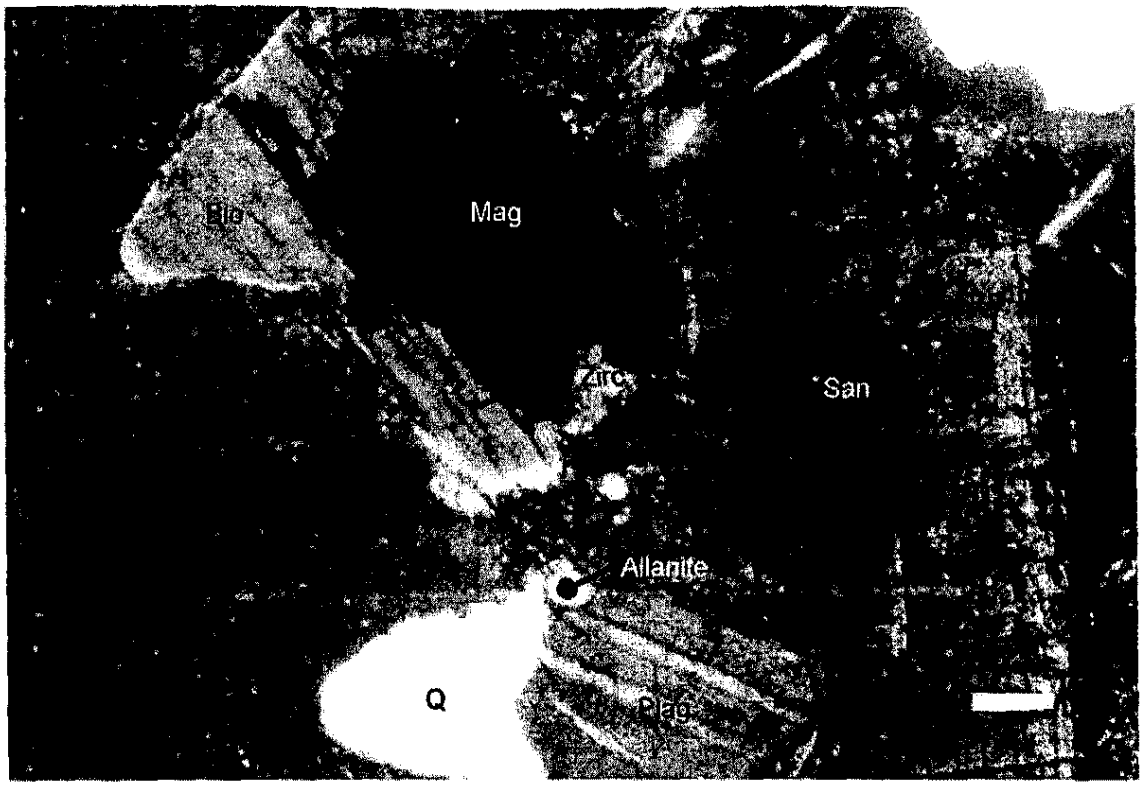

Figure 7c. Sample EBHP. Sanidine overgrowing polysynthetic twinned plagioclase and quartz, allanite, magnetite, biotite, and zircon. Note that magnetite overgrown on zircon, but is overgrown by biotite. Cross polarized light, bar = 10 μm.

Figure 7d. Sample NAP. Oscillatory zoned sanidine phenocryst. Cross polarized light, bar = 10 μm.

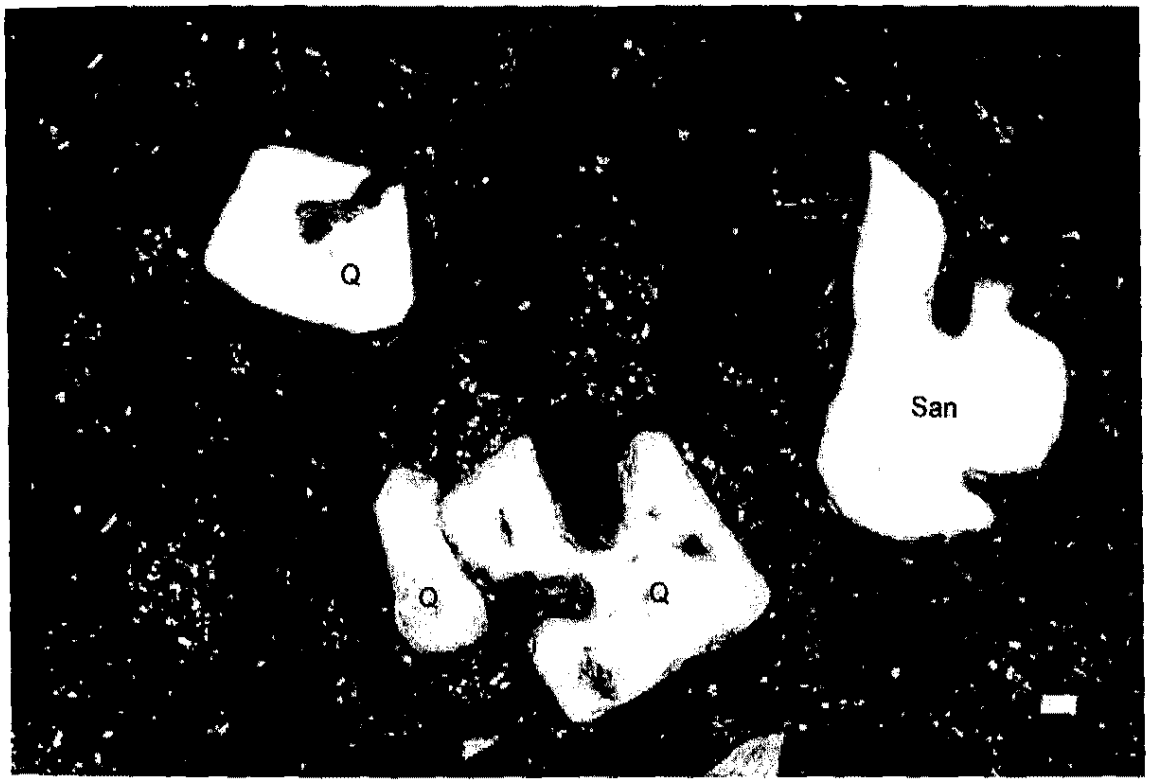

Figure 7e. Sample NAP. Embayed sanidine and quartz. Cross polarized light, bar = 10 μm.

(Figure 7a). Highly embayed quartz is also common, especially in fractured phenocrysts where embayments appear to follow cracks (Figure 7f).

Mafic Phases

Biotite is the only major mafic phase present in all Bearhead Rhyolite samples examined in this study. The typical ratio of mafic to felsic phenocrysts is about 1 to 20. Most samples contain trace amounts (< 1%) of biotite, but samples NAP, NECY, and SHC contain an average of 2 ± 0.1%. Biotite phenocrysts range from 0.1 to 2.5 mm. Biotite phenocrysts and crystal fragments are generally euhedral and unaltered (Figure 7b).

Accessory Phases

Allanite was observed in samples CB, CP, CY, GBR, CYF, BHP, CJ, BHP, CAN, and CC3. Phenocrysts are typically < 0.2 mm in diameter, equant, and euhedral. Allanite occurs as separate phenocrysts in the matrix as well as within glomerocrystic sanidine, biotite, and magnetite.

Zircon is the second most common accessory phase. Zircon phenocrysts are commonly equant, euhedral, and unresorbed. Zircon occurs as separate phenocrysts in the matrix and in clusters associated with biotite, opaque oxides, and, less commonly, feldspars (Figures 7g and 7h). Equant zircon crystals range from 0.3 to 0.4 mm in diameter.

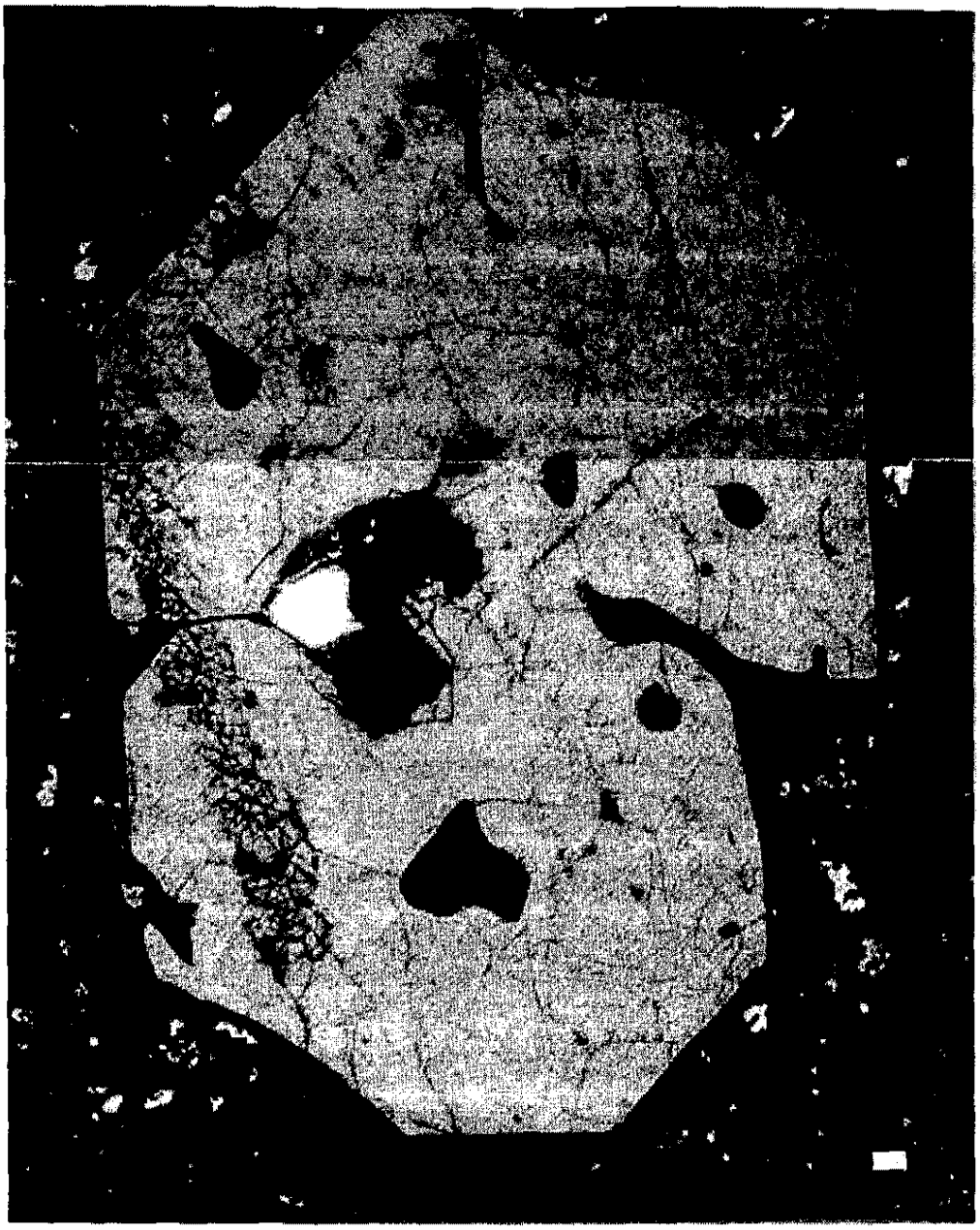

Figure 7f. Sample 31A. Euhedral and embayed quartz. Embayments appear to form along fractures. Cross polarized light, bar = 10 μm.

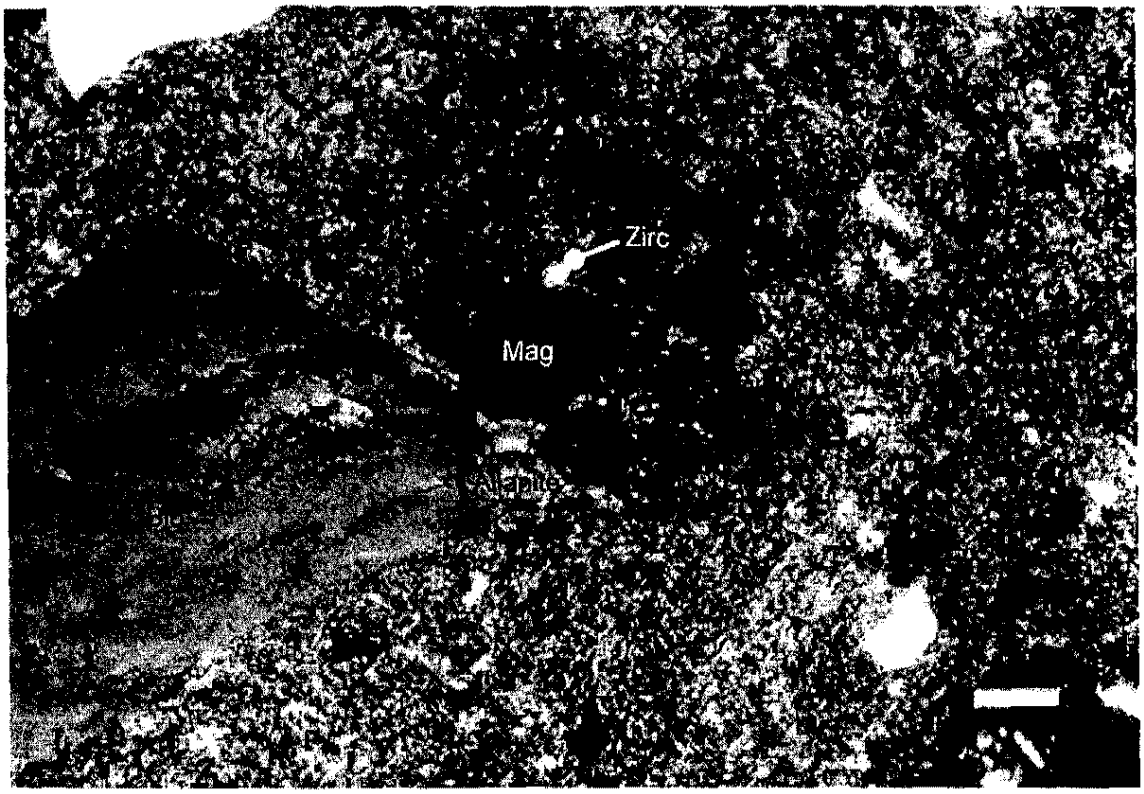

Figure 7g. Sample TA. Allanite, magnetite, and zircon overgrown by biotite. Magnetite overgrown on zircon. Cross polarized light, bar = 10 μm.

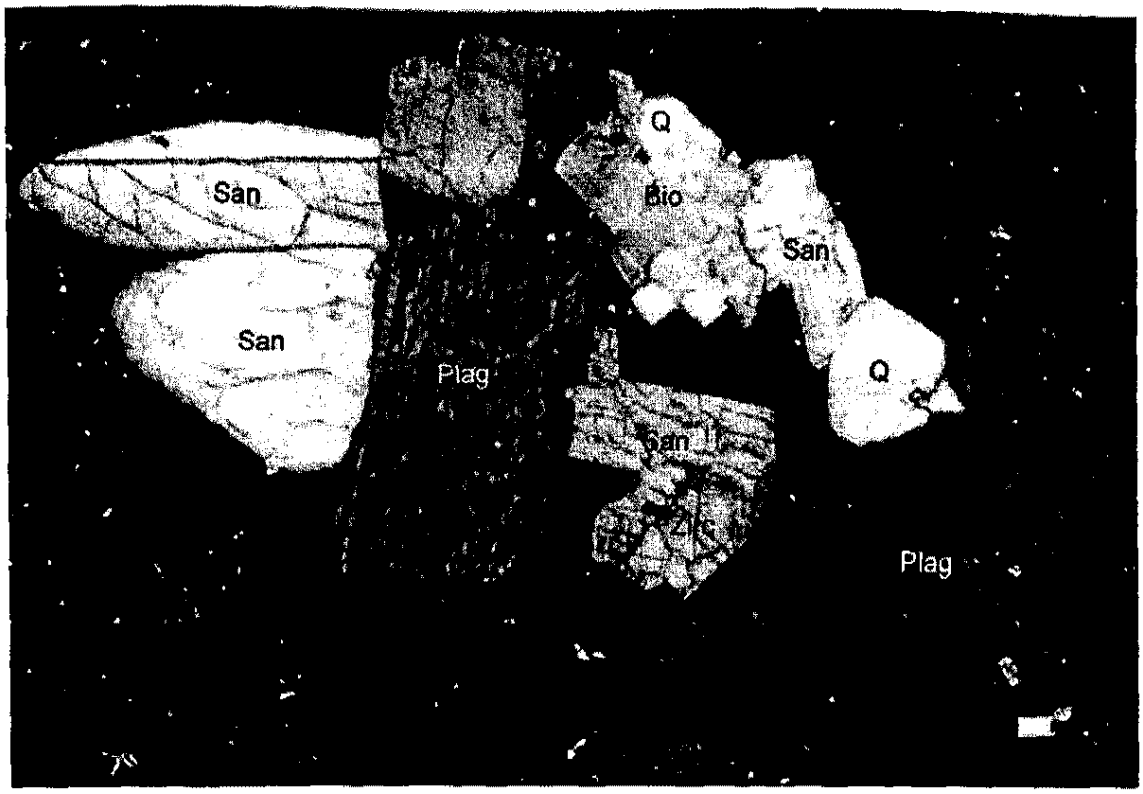

Figure 7h. Sample SAC. Glomerocryst containing polysynthetic twinned, zoned plagioclase, untwinned and carlsbad twinned sanidine, biotite, quartz, and zircon. Biotite is overgrown by plagioclase and quartz. Plagioclase is overgrown by quartz and sanidine. Cross polarized light, bar = 10 μm.

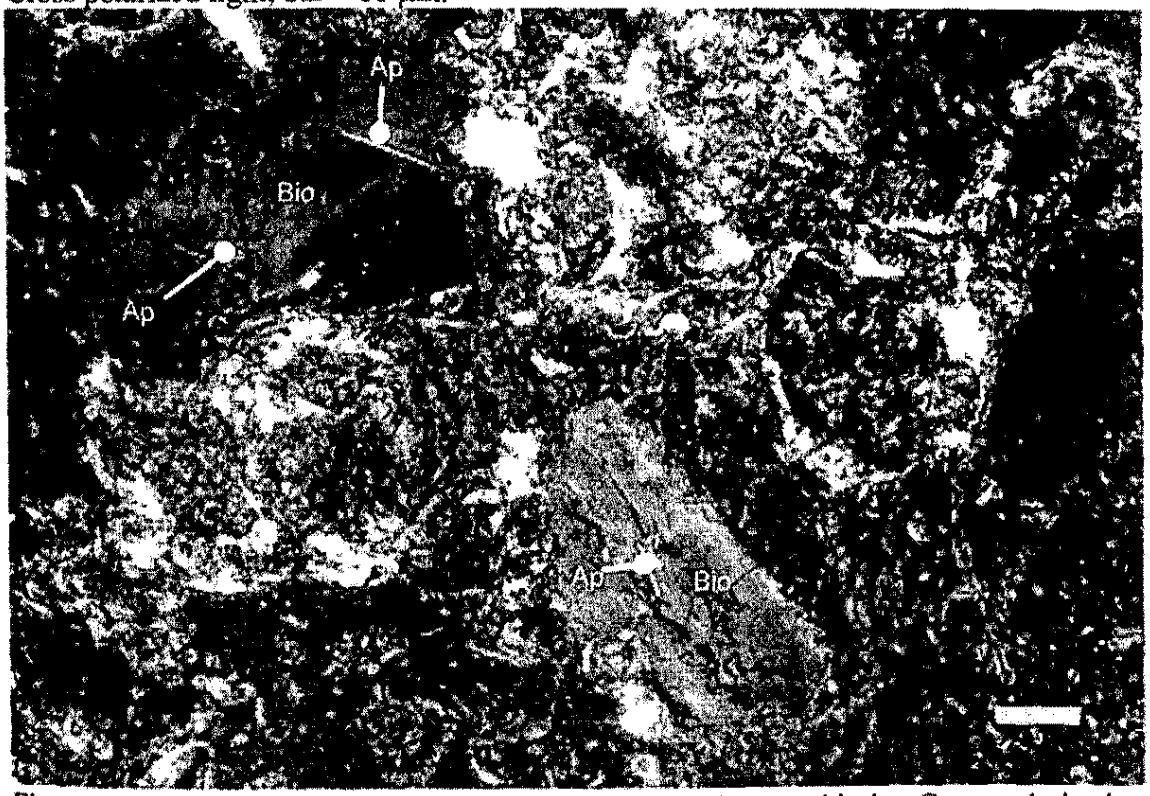

Figure 7i. Sample CY. Apatite overgrown by green and brown biotite. Cross polarized light, bar = 10 μm.

Apatite appears to be the least abundant accessory phase. It was difficult to see apatite and may have been missed even if present. Apatite was identified in EBHP and NAP (Figure 7i) and tentatively identified in NBC, 1 PT, and TWM2.

Magnetite is the most common accessory phase. Phenocrysts are anhedral and range from 0.25 to 0.075 mm in diameter. Magnetite commonly overgrows small portions of glomerocrysts and biotite and appears by itself in the matrix.

Matrix

Aphanitic Bearhead Rhyolite samples contain on average 92% glassy matrix and 20% devitrification features (spherulites), and sometimes are hydrated to the point of forming perlite. Rhyolite samples DB, 31A, and ERP2 and vitophyre samples SAC and TC2 contain < 1% feldspar and < 1% lithic fragments (0.13 to 3.25 mm long) in the matrix. Generally the lithic fragments in these samples possess the same mineralogy as Bearhead Rhyolite samples and may represent magma chamber or vent wall rock fragments. One vitrophyre sample (SAC) contains lithic fragments with a coarser-grained feldspar matrix and abundant biotite (Figure 7j).

Peralta Tuff samples have an average of 99% vesicular matrix. In thin section, most samples display discontinuous to continuous alignment of bubble walls even when not apparent in hand sample. The matrix in the tuffs contain an average of 16% devitrification marked by secondary, fibrous quartz. The 25 to 370 μm long vesicles are equant to elongate and account for an average of 13 ± 9% of 9 thin sections.

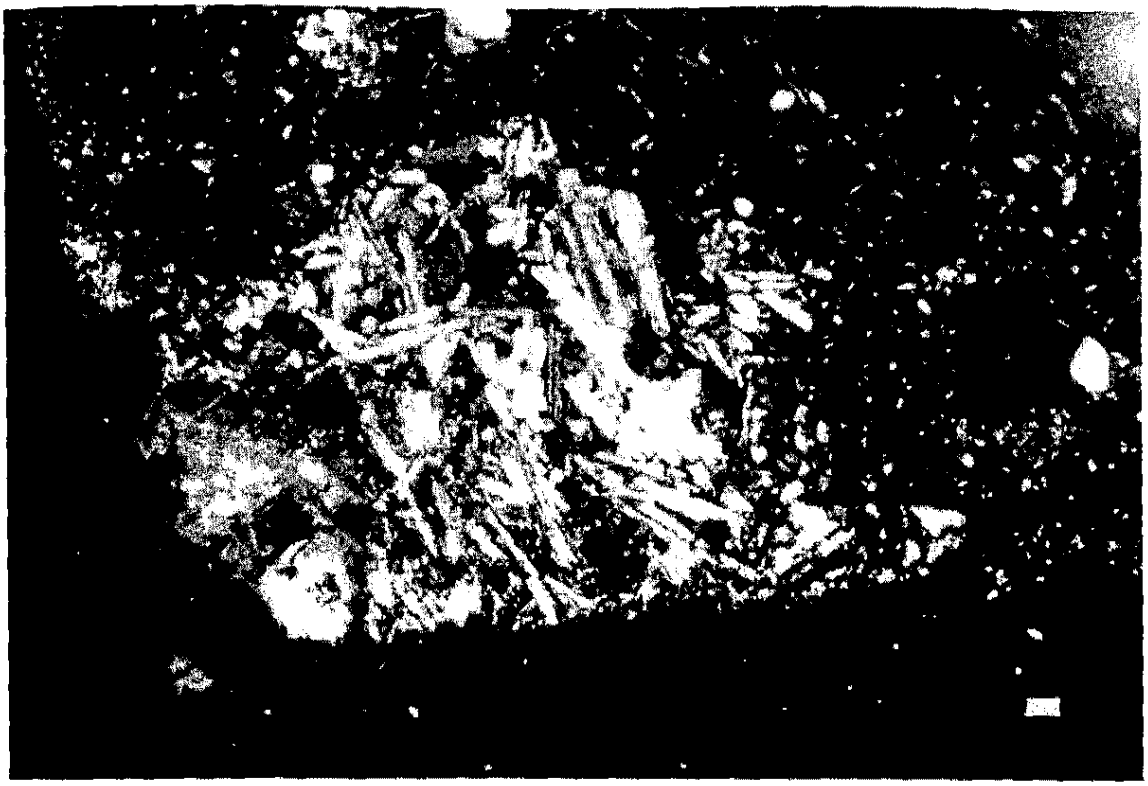

Figure 7j. Sample NHC. Plagioclase lath and biotite rich lithic fragment. Cross polarized light, bar = 10 μm.

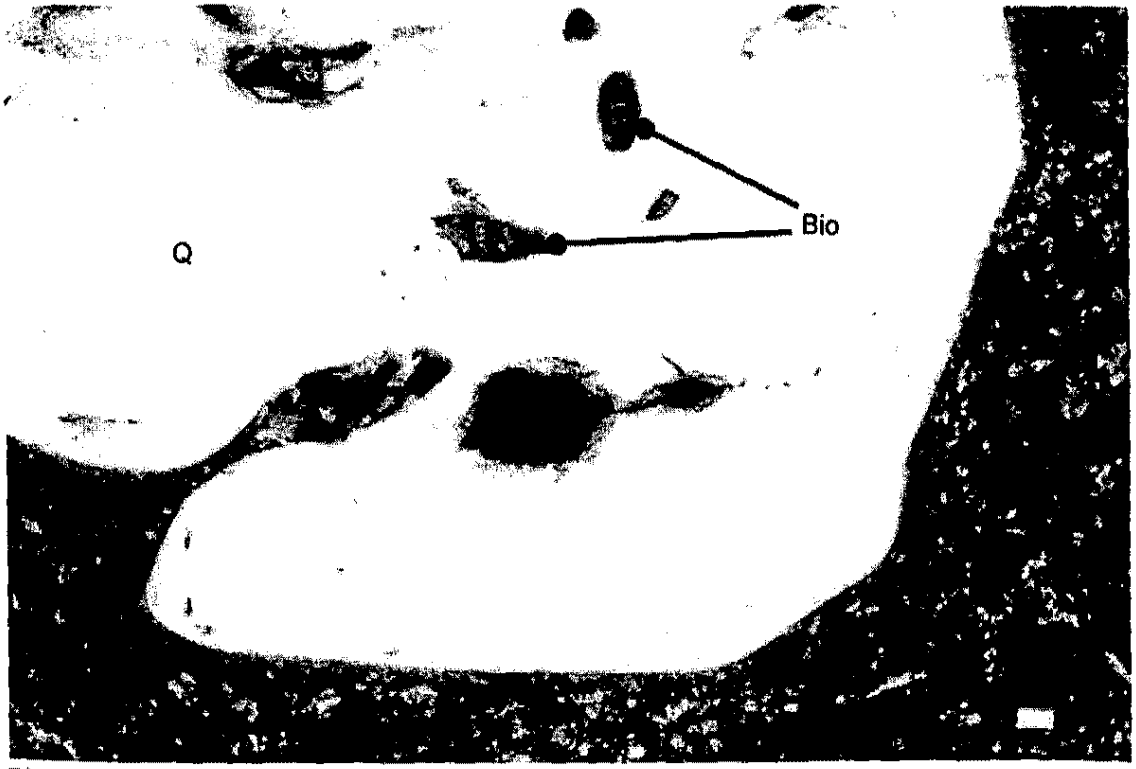

Figure 8. Sample CYF. Embayed, anhedral quartz overgrown on biotite fragments. Cross polarized light, bar = 10 μm.

Inferred Order of Crystallization

Petrographic evidence suggests that the order of crystallization from earliest to latest. was (1) allanite and zircon, (2) magnetite, (3) apatite sometime before biotite, (4) biotite, (5) plagioclase, (6) quartz, and (7) sanidine. It is not possible to determine when allanite crystallized relative to zircon because the two do not occur directly in contact with each other (although both are found within phenocrysts of magnetite). Allanite and zircon (Figures 7g and 7c, respectively) occur within magnetite and biotite phenocrysts. Magnetite (Figures 7g and 7c) is also found within biotite phenocrysts. Apatite (Figure 7i), found within biotite phenocrysts, began crystallizing before biotite, but because apatite is not found associated with allanite, zircon, or magnetite it is not possible to further refine when it crystallized. Biotite is commonly included in plagioclase (Figures 7a, 7b, 7d, and 7h), quartz (Figure 8), and sanidine (Figure 7c). Plagioclase occurs as inclusions in quartz (Figure 7c) and sanidine (Figures 7a and 7b). Finally, quartz is found within sanidine phenocrysts (Figures 7b and 7c).

CHAPTER 4

GEOCHEMISTRY

Samples of Bearhead Rhyolite (37) and Peralta Tuff (21) were collected from each rhyolite dome, flow, and tuff unit for major and trace element analysis (Appendices A and C). Based on the Le Bas et al. (1986) classification system, 2 of the 58 samples are trachydacites, 3 are low-silica rhyolites, and the remainder are high silica rhyolites (Figure 9). The trachydacites are distinct in major and trace element chemistry from the rhyolites. The low-silica rhyolites are distinct in their REE chemistry when compared to the high-silica rhyolites. Four high-silica rhyolites are distinguished from the majority of the Bearhead Rhyolite by their ages and secondarily by their REE chemistry. The remaining 49 high-silica rhyolite samples display remarkable chemical homogeneity and no systematic chemical variation with time ($^{40}Ar/^{39}Ar$ ages discussed in Chapter 5) supporting the reconnaissance geochemical data of Gardner (1985), Guilbeau and Kudo (1985), and Ellisor (1996). See Appendix D for a description of sample collection and analytical methods.

Melt inclusions in Peralta Tuff quartz phenocrysts from 7 locations in Peralta and Colle Canyons (G.A. Smith et al., 1991; Gay and Smith, 1993) were analysed for their major element and volatile contents while sanidine phenocrysts from 4 were analysed for

their major element contents using electron and ion microprobe analysis (Appendix G). A series of electron microprobe analyses across sanidine phenocrysts indicate that they are chemically homogeneous. Ion microprobe analyses indicate that the Bearhead Rhyolite contained an average of 3.27 ± 0.85% H_2O prior to eruption, enough to be considered water saturated. See Appendices H and I for a description of electron and ion microprobe analytical methods and uncertainty.

Overview of Whole Rock Chemistry

All except two of the samples analyzed in this study (major elements recalculated to 100% anhydrous) are rhyolites according to the Le Bas et al. (1986) classification (Figure 9). All rhyolite samples, except GBR (74.8 wt.% SiO_2), are high-silica rhyolites (> 75 wt.% SiO_2) containing an average of 78.0 ± 0.8 wt.% SiO_2. The remaining 2 samples (SHC and NECY) are trachydacites containing 69.0 and 67.7 wt.% SiO_2, respectively (Figure 9). All samples contain Al_2O_3 mole% > ($CaO + Na_2O + K_2O$) mole% making them peraluminous (Shand, 1927). In summary, the Peralta Tuff and most of the Bearhead Rhyolite are peraluminous, high-silica rhyolites. GBR is a peraluminous low-silica rhyolite while and SHC and NECY are peraluminous trachydacites.

Effect of Alteration on Bearhead Rhyolite Chemistry

Many studies have demonstrated the effect of hydration and devitrification on major and minor element abundances of rhyolitic glass (Lipman, 1965; Ewart, 1971;

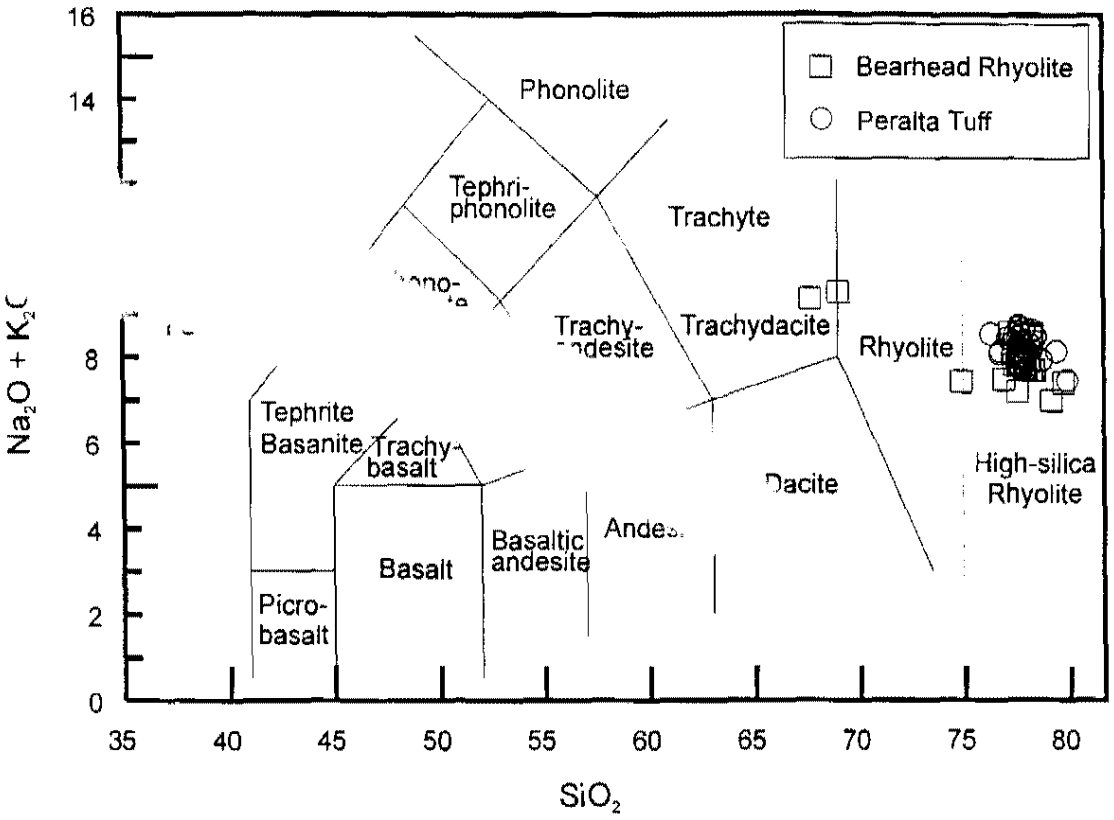

Figure 9. Total alkalis ($Na_2O + K_2O$) vs SiO_2 classification diagram for the Bearhead Rhyolite (modified from LeBas et al., 1986). All analyses recalculated to 100% anhydrous and expressed in wt.%.

Kochnar, 1977; Zielinski et al., 1977; Jezek and Noble, 1978). The samples collected for this study show a wide variation in hydration with total LOI (loss on ignition) ranging from 0.33 to 4.85 wt.% for rhyolite and vitrophyre and 3.33 to 5.87 wt.% for pumice (Appendix B). Highly hydrated samples, such as SCC (rhyolite) and 2 PT (pumice) (13.91 and 8.16% LOI, respectively), are not considered further in this study. The variability of LOI values suggest that the gain or loss of elements by hydration must be considered.

Major elements such as sodium and potassium are the most affected by hydration. Increasing hydration causes progressive loss of sodium and gain of potassium (Kochnar, 1977; Jezek and Noble, 1978). Some studies found that highly porous vitric rocks such as tuffs may lose as much as 3 wt.% Na_2O (Kochnar, 1977) while other studies report significantly smaller losses (Jezek and Noble, 1978). Trace elements affected by hydration include Li, F, Sr, Ba, and U (Zielinski et al., 1977). Of these elements, Sr, Ba, and U were analyzed for this study. Generally, U becomes depleted while Sr and Ba become enriched with increasing hydration (Zielinski et al., 1977).

It is possible to assess the effects of hydration on samples collected for this study using a sample of relatively unhydrated rhyolite (RH2, 0.33% LOI) and a coexisting hydrated rhyolite (RH3, 2.55 %LOI) which were collected from the same rhyolite dome less than 10 meters apart. If these samples are assumed to have had the same original composition then any changes in major and trace element chemistry can probably be attributed to the difference in degree of hydration. Major (calculated anhydrous) and minor elements for these two samples are identical within analytical uncertainty except for Na_2O and K_2O. Na_2O decreases, as expected, from 3.8 to 3.6 wt.% while K_2O

decreases from 4.5 to 4.2 wt.% with increasing hydration (even though previously mentioned work suggests gain). The difference between Na_2O and K_2O between these two samples is well above analytical uncertainty and must represent real differences. Other samples (e.g., SH1 and 2) with lower degrees of hydration (0.66 and 0.87% LOI, respectively) display decreasing Na_2O and increasing K_2O abundances with increasing hydration as predicted. The lack of major, minor, or trace element variation (even elements that are typically highly affected) between variably hydrated sample pairs suggests that hydration has not significantly altered the chemistry of the samples used in this study.

Major Element Chemistry

Major Element Chemistry Versus Silica

Most Bearhead Rhyolite samples display little major element variation with respect to SiO_2. The trachydacites (NECY and SHC) and, to a lesser extent, the low-silica rhyolite (GBR) contain greater concentrations of Al_2O_3, Na_2O, CaO, Fe_2O_3, TiO_2, and P_2O_5 than the high silica rhyolites. The high silica rhyolites are essentially chemically homogeneous with respect to major element chemistry.

Major Element Chemistry Versus Age

Plots of major elements versus age also fail to yield significant patterns ($^{40}Ar/^{39}Ar$ ages discussed in Chapter 5) . SiO_2 and Al_2O_3 show more chemical variation between samples of the same age than samples of different ages. Alternatively, K_2O, Na_2O, CaO, Fe_2O_3, and TiO_2 do not vary between samples of the same age or samples of different

ages. Samples CY and CYF tend to plot away from the other Bearhead Rhyolite samples on CaO and TiO_2 versus age plots but these variations lie within analytical error. Sample PN tends to lie with the other samples in terms of chemistry, but is distinguished from all other Bearhead Rhyolite samples by its significantly younger age (1.47 ± 0.01 Ma, discussed in Chapter 5). Due to a lack of age constraints, the trachydacites NECY and SHC and the low-silica rhyolites GBR, SH1, and SH2 are not considered here.

Trace Element Chemistry

Trace Element Chemistry Versus Niobium

To establish trace element trends, it is necessary to choose an incompatible trace element that is accurately analyzed and relatively immobile. An incompatible element is chosen because the last stage in the evolution of rhyolitic magmas is likely in an upper crustal magma chamber prior to eruption. The dominant mechanism in this situation (750 °C magma surrounded by ~200-300 °C wallrock) will probably be fractional crystallization. Based on these observations/assumptions, a trace element that behaves incompatibly during fractional crystallization and that is immobile is chosen as an index of differentiation. While Cs and Rb are highly incompatible and have good analytical precision, Nb is incompatible, has good analytical precision, and is less mobile.

For a summary of the trace element geochemistry of the Bearhead Rhyolite see Table 2. The trachydacite samples (SHC and NECY) are characterized by higher concentrations of Hf, Sc, Y, Tb, Ba, Lu, Nd, Zn, La, Ce, Eu, Yb, Sr, Zr, and Sm than all of the other samples (Figures 10 and 11). Sample PN also contains higher concentrations

Table 2. Summary of Trace Element Trends with Increasing Nb

Samples	All Others	SHC, NECY	GBR, SH1 and 2	CY, CYF, CF		PN
Decreasing Trend		Ba, Sr, U	Ba, Sc	Ba, Ce, Sm	Enriched*	Hf, Ta, La, Ce, U, Sm, Zr
Increasing Trend	Y, Lu, Nb	Eu, Zr, Ta, Tb, Hf, Sm, Yb, Y, Sc, Nb, Lu, La, Ce, Zn	Th, Zr, U, Nd, Nb, Sr	Ta, Sc, Lu, Zn, Nb	Depleted*	Sc, Cs, Eu
					Same as SHC, NECY	Th, Tb, Nd, Lu, Yb, Rb
Invariant Trend	Zr, Sr, Th, La, Hf, Ce, Eu, Rb, Sm, Sc	Cs, Th, Nd**, Rb	Y, Sm, Lu, Yb, Ta, Tb, Cs, Eu, Zn**, Rb	Rb, Sr, Th, Tb**, Eu	Same as GBR, SH 1and 2	Zn, Y, Rb, Sr
Scattered Trend	Ta, Cs, Nd, U, Tb, Zn, Ba, Yb		La, Ce	Yb, Y, U, La		
					Accessory Phases	Zircon
Accessory Phases	Allanite Apatite Zircon	Zircon	Allanite Zircon Apatite	Allanite Zircon		

** variation within analytical uncertainty

* relative to the majority of Bearhead Rhyolite and Peralta Tuff samples

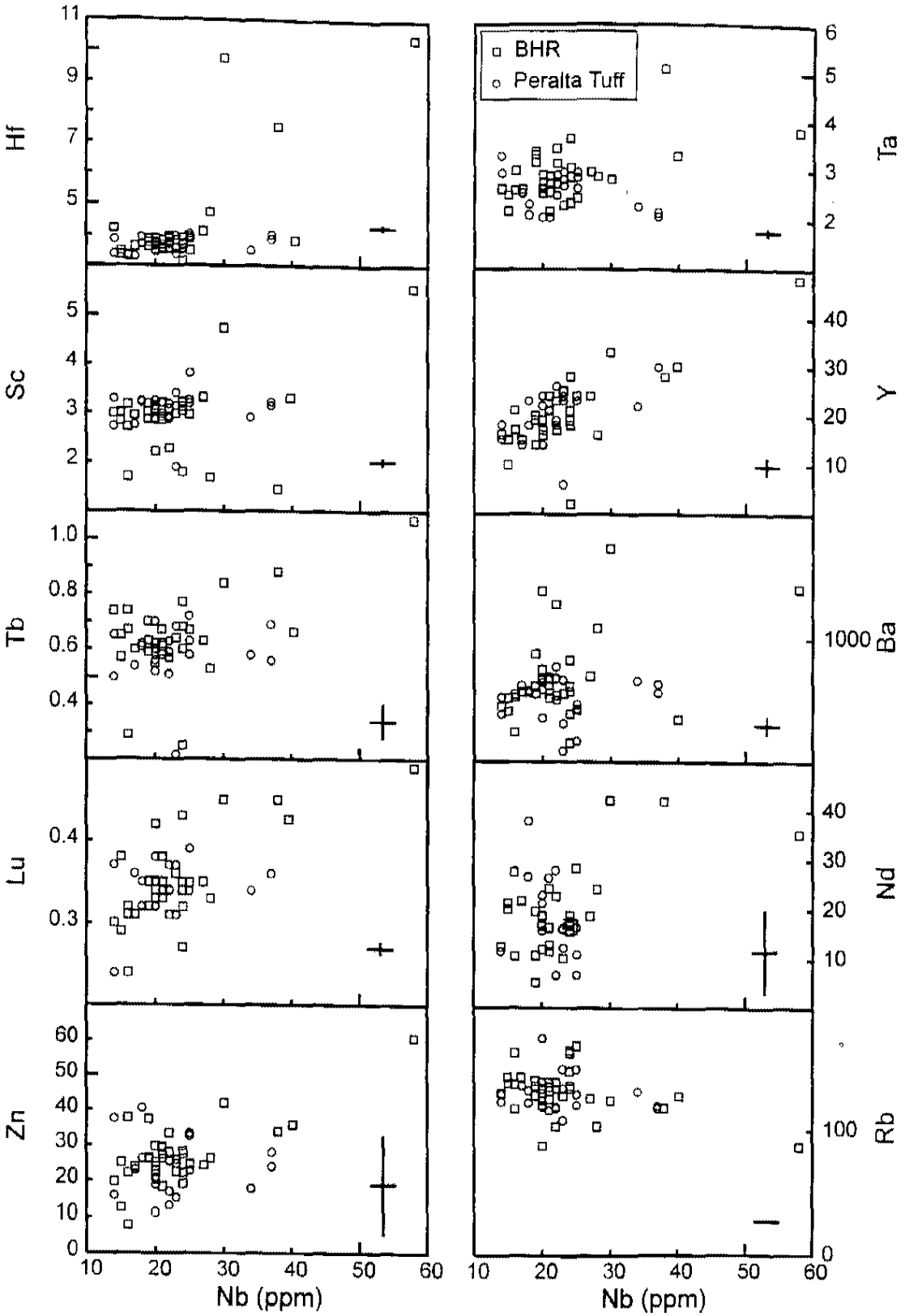

Figure 10. Plots of trace elements versus Nb. All elements are expressed in ppm. Bars depict ± 1σ uncertainty. BHR = Bearhead Rhyolite.

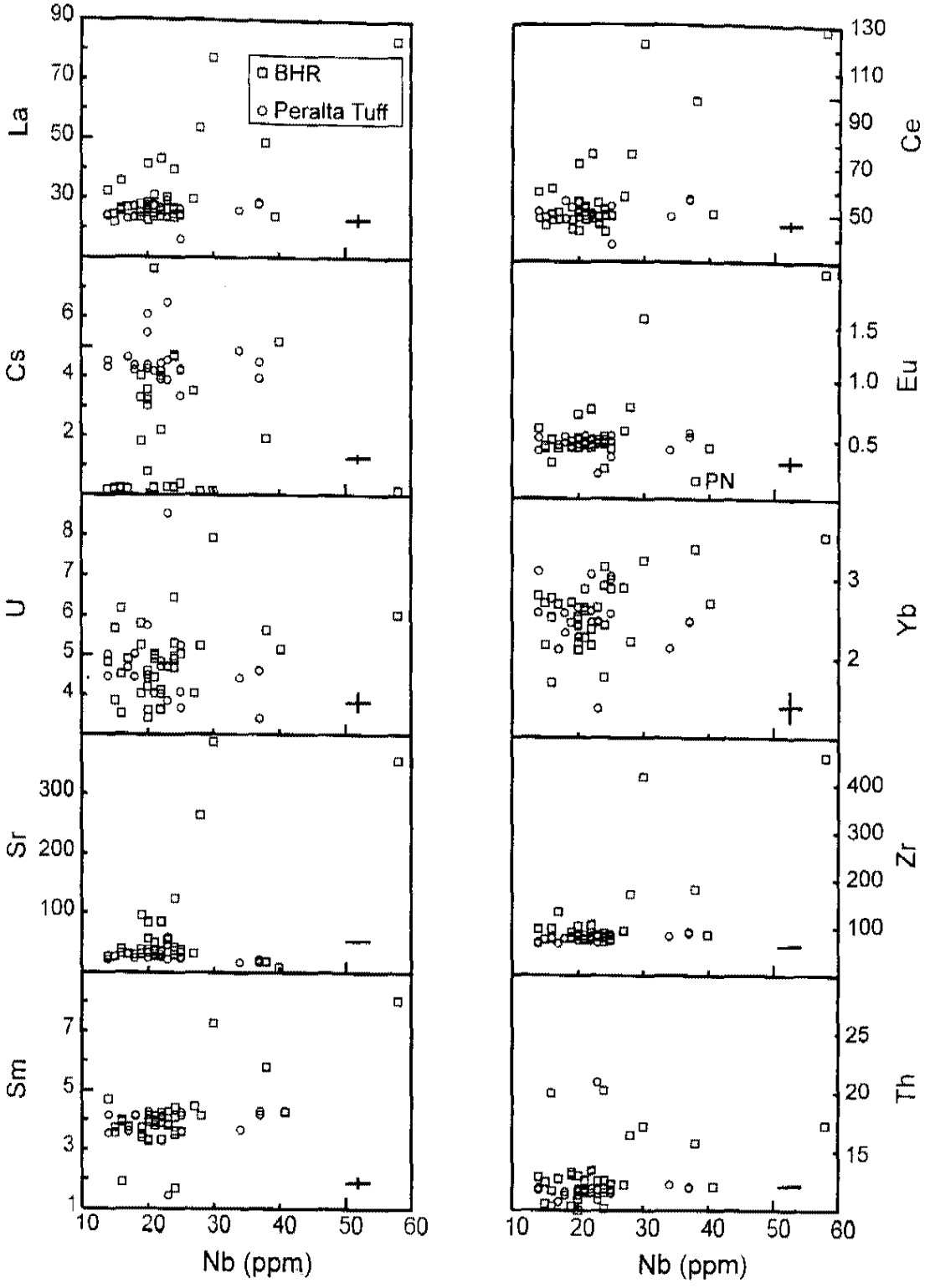

Figure 11. Plots of trace elements versus Nb. All elements are expressed in ppm. Bars depict $\pm 1\sigma$ average uncertainty. Zr and Th's uncertainty is less than the thickness of the horizontal bar. BHR = Bearhead Rhyolite.

of Y, Tb, Lu, Nd, Zn, Rb, and Yb as SHC and NECY but to a lesser extent for Hf, La, Ce, and Sm. Additionally, PN contains lower concentrations of Eu and Sc than most of the other samples. The low-silica rhyolites GBR, SH1, and SH2 are characterized by slightly lower concentrations of Sc and Rb and slightly higher concentrations of Ba, La, Ce, Eu, Sr, Zr, and Th compared to most of the Bearhead Rhyolite and Peralta Tuff samples. High-silica rhyolite samples CY, CYF, and CF are characterized by lower concentrations of Sc, Y, Tb, Ba, Lu, Zn, Eu, Yb, and Sm and higher concentrations of Rb, Th, and U compared to all other samples. The remaining Bearhead Rhyolite and Peralta Tuff samples have scattered or invariant trace element patterns with increasing Nb concentrations. Y and Lu increase with increasing Nb while Zr, Sr, Th, La, Hf, Ce, Eu, Rb, Sm, and Sc do not vary with changing Nb. Ta, Cs, Nd, U, Tb, Zn, Ba, and Yb scatter about an average value or vary greatly with little change in Nb such that no trends are discernable.

Trace Element Chemistry Versus Age

There is little variation of trace element chemistry with time (see Chapter 5 for a discussion of the geochronology) in the Bearhead Rhyolite (Figures 12 and 13). Hf, Zn, La, Ce, Eu, Sr, and Zr display no variation between samples of the same age or samples of different ages. Ta, Lu, Nd, Rb, Cs, and U do not vary over a 1.0 Ma interval, but show slight to significant amounts of scatter within samples of the same age. Alternatively, Ba appears to increase slightly over a ~1.0 Ma interval while Yb appears to decrease slightly over the same time interval. Samples CY, CYF, and CF, which were erupted ~200 ka

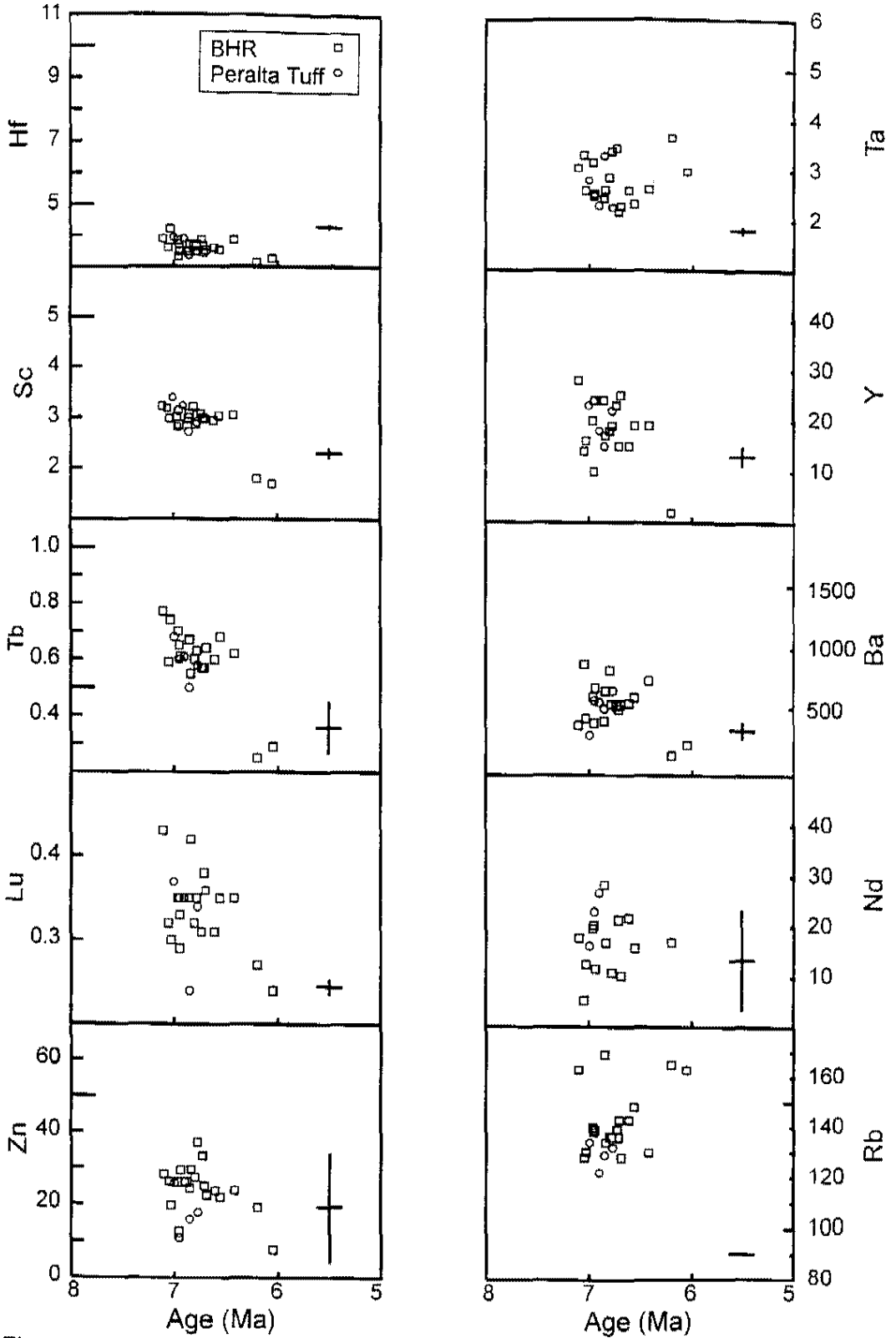

Figure 12. Plots of trace elements versus age (Ma). All elements are expressed in ppm. BHR = Bearhead Rhyolite. Bars depict average 1σ uncertainty. Rb's uncertainty is less than the thickness of the horzontal bar. An average uncertainty is reported for the age data.

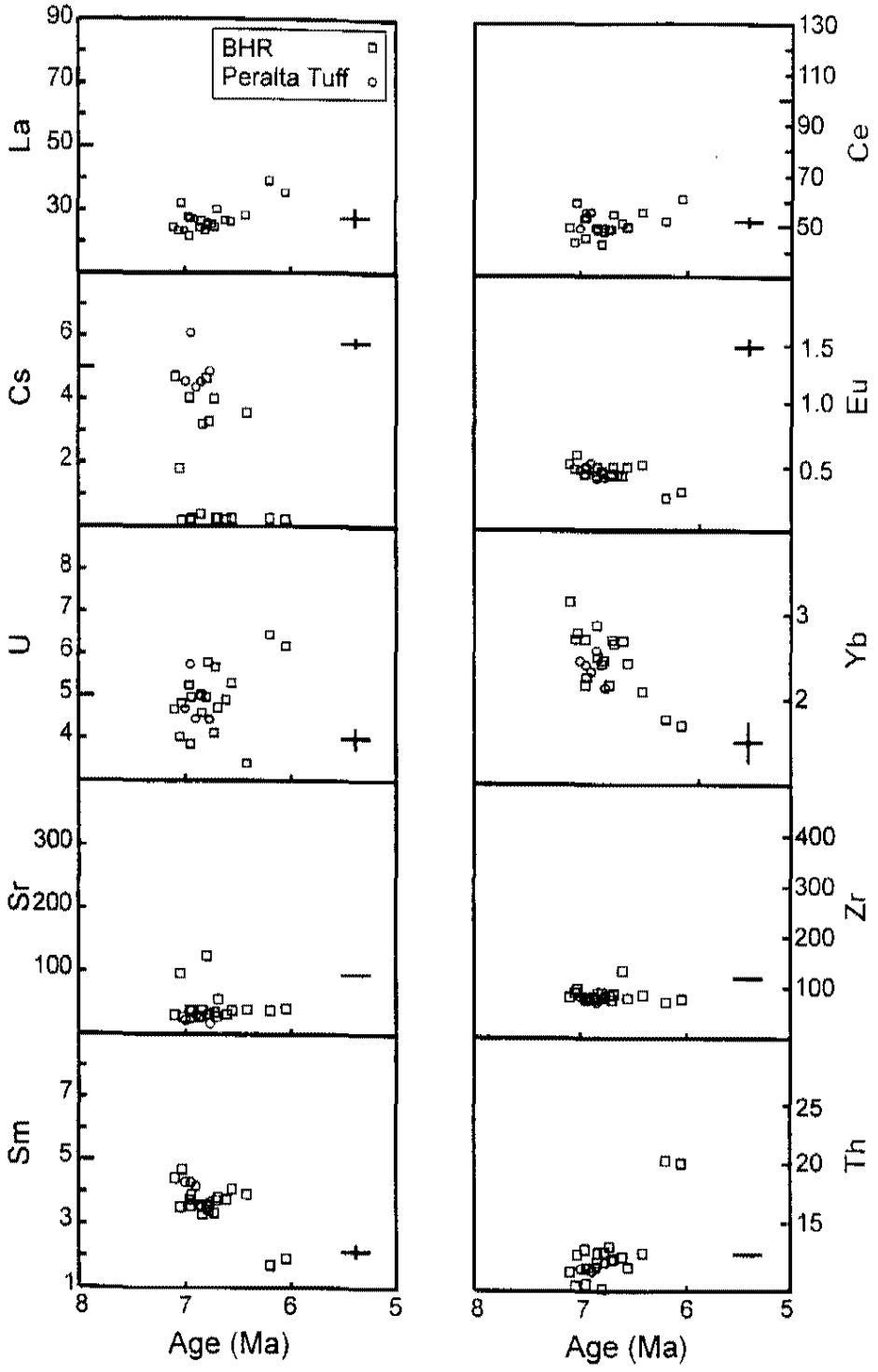

Figure 13. Plots of trace elements versus age (Ma). All elements are expressed in ppm. BHR = Bearhead Rhyolite. Bars depict 1σ uncertainty. An average uncertainty is reported for the chemical and age data. Sr, Zr, and Th's uncertainty is less than the thickness of the horizontal bar.

after the majority of Bearhead Rhyolite eruptions, contain lower abundances of Sc, Y, Tb, and Sm and higher abundances of Th compared to most other samples. Furthermore, PN was erupted ~5 Ma after all of the other eruptions implying that it is not Bearhead Rhyolite.

REE/Chrondrite Diagrams

Chondrite normalized REE diagrams suggest five geochemical groups within the Bearhead Rhyolite (Figure 14). These groups are defined as follows: (1) the Main Cluster contains 24 rhyolite samples and the Peralta Tuff; (2) Group 2 contains trachydacite samples SHC and NECY; (3) sample PN; (4) Group 4 contains rhyolite samples GBR, SH1, and SH2; and (5) Group 5 contains rhyolite samples CY, CYF, and CF.

Main Cluster

The Main Cluster forms a tight group on the chondrite normalized diagram. All REEs are enriched relative to chondrite. The LREEs are enriched 30 to 100 times chondrite while the HREEs are enriched uniformly 10 to 20 times chondrite. The Main Cluster has an average Eu/Eu* of 0.5. There is considerable variation in Nd on the chondrite plots (8 to 60 times enrichment) which is probably due to analytical error as there are no minerals that selectively incorporate Nd relative to other REEs. Nd, therefore, is not further considered.

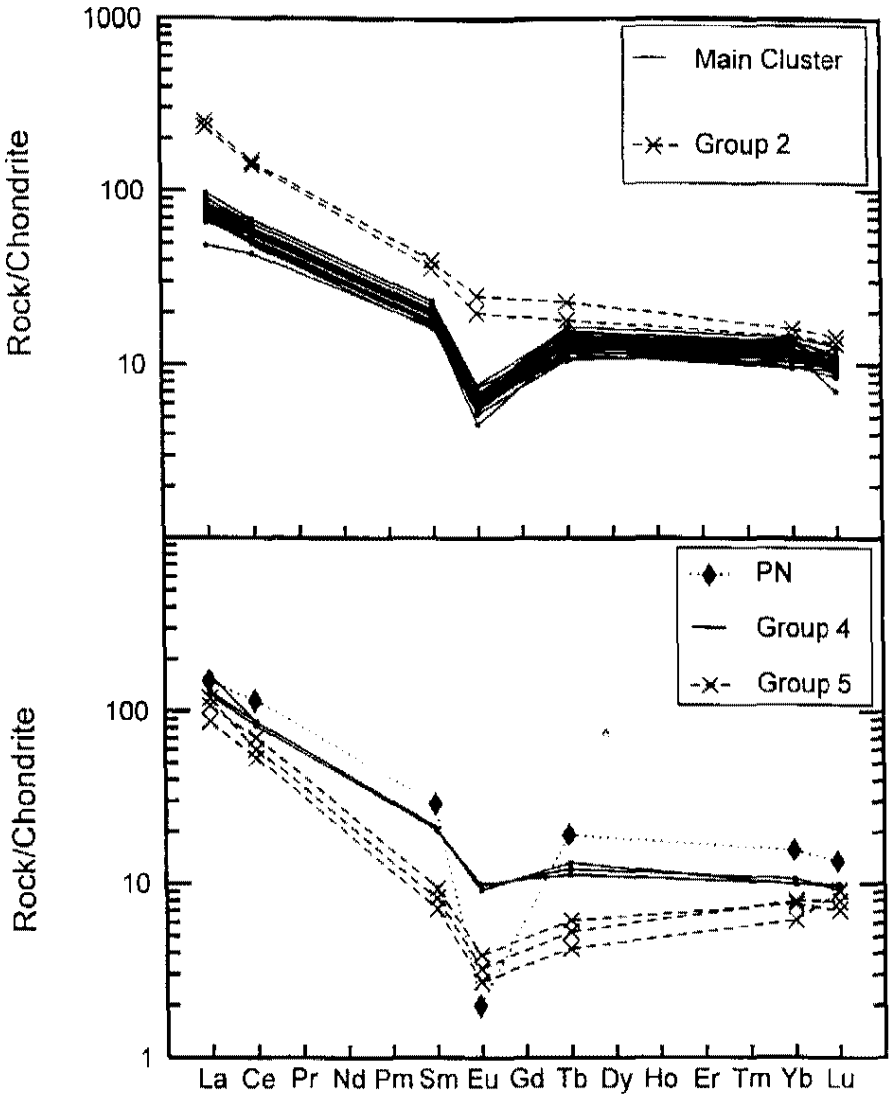

Figure 14. REE/Chondrite plots for the Main Cluster, Group 2 (SHC, NECY); Group 4 (GBR, SH1, SH2); and Group 5 (CY, CYF, CF). Chondrite values from Nakamura (1974). Nd values not included due to analytical error in the analysis.

Group 2

The second group containing the trachydacite samples (SHC and NECY) is distinguished from all other groups by its enrichment in all REEs and its small negative Eu anomaly (Eu/Eu* = 0.9). The LREEs are enriched from 40 to 250 times chondrite and 10 to 150 times Main Cluster LREEs. The HREEs are also enriched compared to chondrite (20 times) but only slightly enriched relative to the Main Cluster (~ 3 times).

PN

Sample PN is distinguished from all other groups by a large negative Eu anomaly (Eu/Eu* = 0.1). The LREEs are enriched from 30 to 105 times chrondrite and ~ 10 times the Main Cluster. The HREEs are also enriched compared to chondrite (20 times) but only slightly enriched relative to the Main Cluster and are similar to Group 2.

Group 4

The fourth group (GBR, SH1, and SH2) is characterized by its Eu anomaly (Eu/Eu* = 0.6) that lies between that of the Main Cluster and Group 2 (10 times enriched relative to chondrite, 3 times enriched relative to the Main Cluster, and 30 times depleted relative to Group 2). While the LREEs and HREEs are enriched from 10 to 100 times and 10 times chondrite, respectively, they overlap Main Cluster values.

Group 5

The fifth group (CY, CYF, and CF) is characterized by a small Eu anomaly ($Eu/Eu^* = 0.5$), LREE and HREE values. The LREEs are enriched 90 to 10 times chondrite and are depleted 10 to 50 times relative to all other groups. The HREEs are enriched 6 to 8 times chondrite and are depleted 4 to 10 times relative to all other groups.

Using Trace Element Ratios to Define Cogenetic Groups

Plots of trace element ratios that are similarly compatible or incompatible in rhyolitic magma are useful in resolving cogenetic groups. Ratios of similarly behaving trace elements are not effected by upper crustal magmatic processes such as fractional crystallization and thus may reflect the composition of magma produced in the original melting event that produced parental magmas. Therefore, rock suites that are derived from different sources in the middle to lower crust may display distinct trace element ratios that do not change as the magmas evolve in upper crustal magma chambers prior to eruption. Substantiating the REE/Chondrite plots in Figure 14, Figure 15 suggests that the Bearhead Rhyolite contains five cogenetic groups. Groups 4 and 5 display similar Nb values to the Main Cluster, but consistently plot away from the Main Cluster in most other trace elements. Group 2 consistently is enriched in Nb and other trace elements relative to the Main Cluster. On two of the three ratio plots, PN plots between the most evolved samples of the Main Cluster and Group 2 reinforcing the interpretation that it is chemically distinct from the Bearhead Rhyolite.

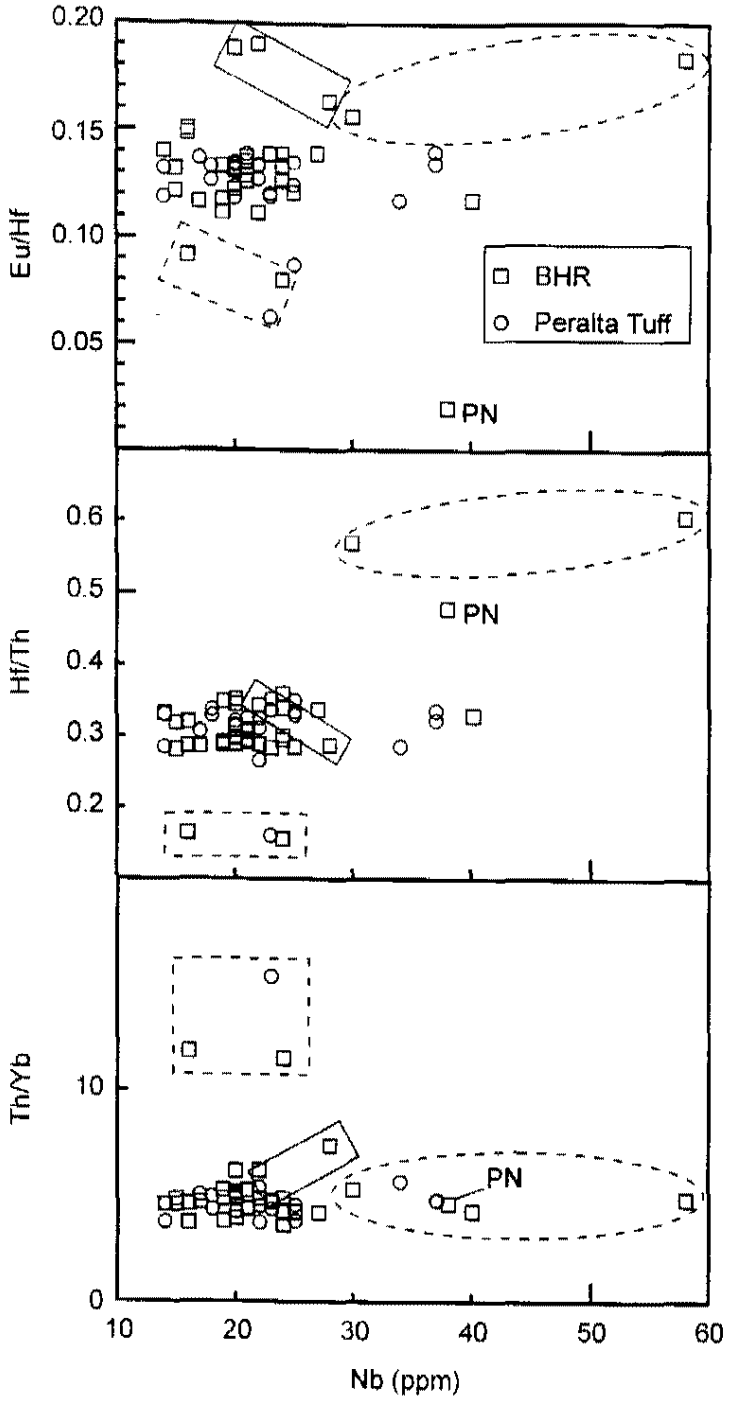

Figure 15. Ratios of similarly incompatible or compatible elements versus Nb to resolve different petrogenetic groups. Abundances expressed in ppm. BHR = Bearhead Rhyolite. Main Cluster (all samples not contained in rectangles or ovals); Group 2 contains SHC and NECY (dashed oval); Group 4 contains GBR, SH1, and SH2 (solid rectangle); and Group 5 contains CY, CYF, and CF (dashed rectangle).

Chemical Variations Within Sanidine Phenocrysts from the Peralta Tuff

Electron microprobe analyses across two sanidine phenocrysts from Peralta Tuff samples TWM1 and 2 reveal that these phenocrysts do not vary in composition from $Or_{59}Ab_{40}An_1$ (Figures 16 and 17). One more series of electron microprobe analyses across a sanidine phenocryst from Peralta Tuff sample CC3 reveals an initial increase in Na_2O and decrease in K_2O from core to rim ($Or_{67}Ab_{31}An_1$ to $Or_{56}Ab_{43}An_1$) followed by a composition similar to samples TWM1 and 2 (Figure 18).

Volatile Content of the Bearhead Rhyolite

A total of 28 ion microprobe analyses of melt inclusions from 6 quartz phenocrysts from Peralta Tuff samples 1PT, TWM1, TWM2, TA, CC3, and CAN indicate that the Bearhead Rhyolite magma contained an average of 3.27 ± 0.85 % H_2O prior to eruption. The lowest sample in the stratigraphic section (1PT) contains a higher percentage of water than the other samples (~5.4 %H_2O) while the remainder of the section displays little variation in water content from the mean. See Appendix G for the volatile contents of quartz melt inclusions.

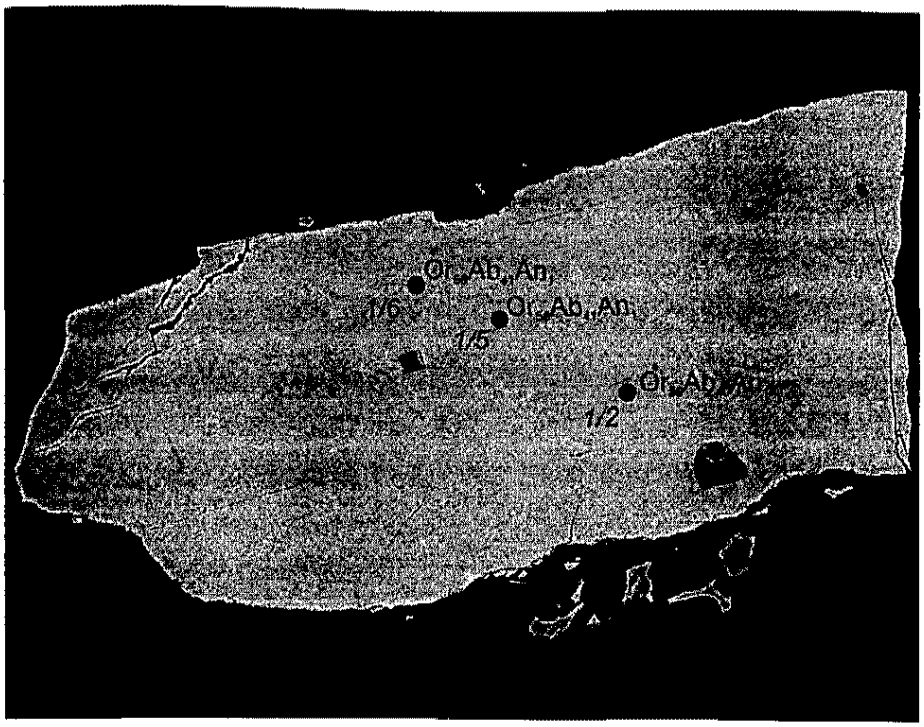

Figure 16. SEM image of a sanidine phenocryst from Peralta Tuff sample TWM1. Dots mark locations of electron microprobe analyses and sample numbers in italics. Width of view is 200 μm.

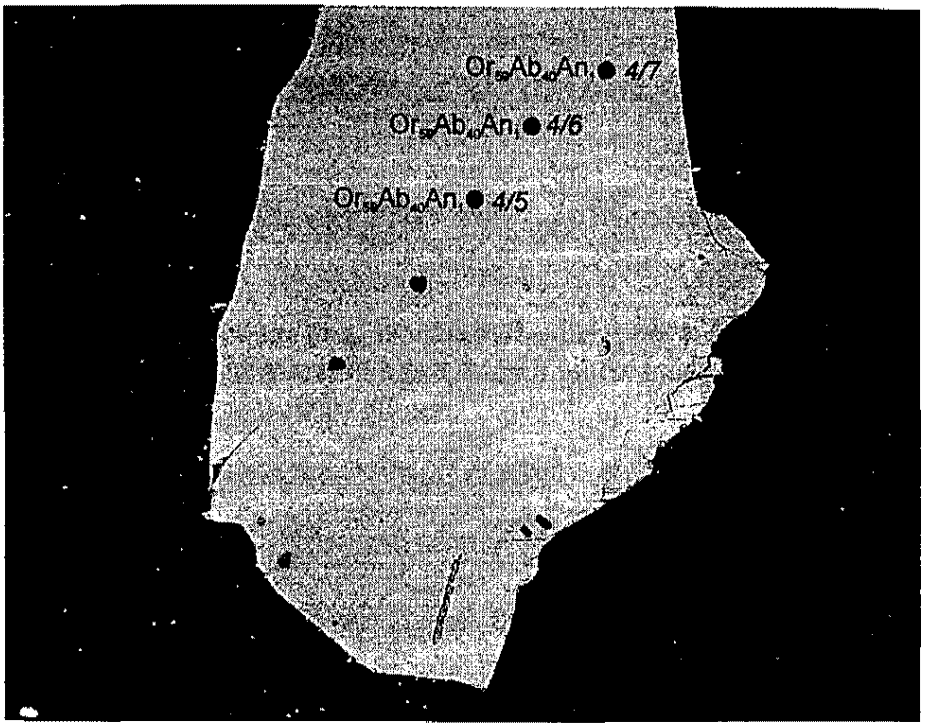

Figure 17. SEM image of a sanidine phenocryst from Peralta Tuff sample TWM2. Dots mark locations of electron microprobe analyses and sample numbers in italics. Width of view is 200 μm.

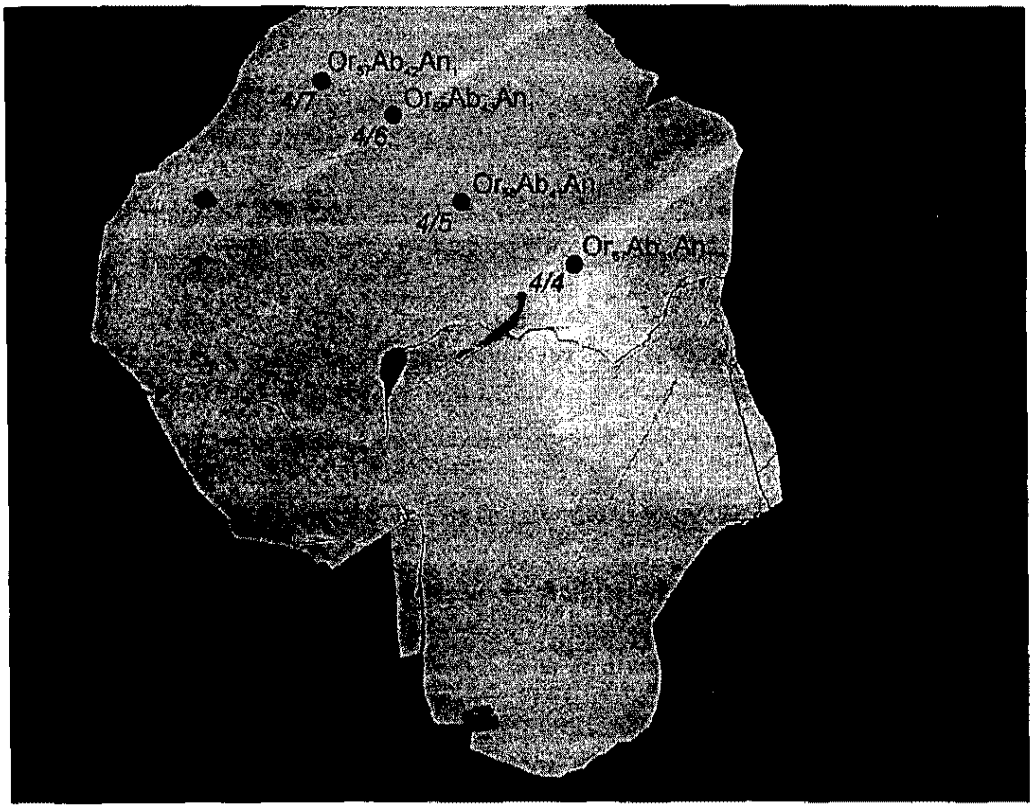

Figure 18. SEM image of a zoned sanidine phenocryst from Peralta Tuff sample CC3. Dots mark locations of electron microprobe analyses and sample numbers in italics. Width of view is 200 μm.

CHAPTER 5

GEOCHRONOLOGY

A total of 20 new single and multiple phenocryst laser fusion $^{40}Ar/^{39}Ar$ ages were obtained on 28 mapped Bearhead Rhyolite domes at the University of Houston and New Mexico Institute of Mining and Technology. The ages compliment 5 previously determined $^{40}Ar/^{39}Ar$ ages on the Peralta Tuff (McIntosh and Quade, 1995), and 9 K/Ar ages on the Bearhead Rhyolite (Leudke and Smith, 1978; Gardner and Goff, 1984; Gardner et al., 1986) (Appendix K). These new dates suggest that chemically homogeneous Main Cluster samples were erupted between ~7.1 and 6.4 Ma whereas Group 5 (CY, CYF, CY) was erupted ~6.0 Ma. A dome at Paseo del Norte (PN), in the northern portion of the field area, was erupted ~ 1.5 Ma and is, therefore, too young to be Bearhead Rhyolite. Appendix H gives details on the analytical methods.

Intercalibration of the $^{40}Ar/^{39}Ar$ Dating Laboratories

Intercalibration of the University of Houston $^{40}Ar/^{39}Ar$ data with those from the New Mexico Institute of Mining and Technology was accomplished by analyzing sample 31B at both laboratories. The fluence monitor for samples run in both labs was Fish Canyon Tuff sanidine (Australian National University #92-176) with an age of 27.9 Ma (Steven et al., 1967; Cebula et al., 1986). Analyses dome at New Mexico Tech yielded

an average age of 6.85 ± 0.05 Ma while the University of Houston laboratory yielded an average age of 6.93 ± 0.09 Ma for sample 31B (Table 3). These two populations overlap at 1σ suggesting that $^{40}Ar/^{39}Ar$ ages from each laboratory are directly comparable. Table 4 summarizes the $^{40}Ar/^{39}Ar$ age determinations for Bearhead Rhyolite domes (discussed below).

Data Treatment

When possible, individual sanidine phenocrysts from each Bearhead Rhyolite dome were dated. By dating individual phenocrysts it is possible to identify components of mixed phenocryst populations containing juvenile phenocrysts, altered phenocrysts (younger ages), and xenocrysts (older ages). Ideally, this allows an accurate eruptive age to be calculated based on the ages of the juvenile phenocrysts alone. Several Bearhead Rhyolite samples (WBHP, CP, 31B, CB, SM, CY, NAP, NBC, SEAP, 9202P, and TC) contained <150 to 350 μm diameter phenocrysts that are too small to date individually as the $^{40}Ar^*$ (radiogenic ^{40}Ar) is too small to measure. In this instance groups of 4 to ~80 phenocrysts were combined to obtain a sufficient amount of $^{40}Ar^*$ for analysis (see Appendix K for details on which analysis used single crystals or groups of crystals). These multiple phenocryst analyses yield comparable precisions to the single crystal analyses suggesting that it is a viable technique for obtaining age data from small crystals. However, the problem of potential xenocrystic contamination is reintroduced.

Table 3. Comparison of $^{40}Ar/^{39}Ar$ Ages for Sample 31B from University of Houston and New Mexico Institute of Mining and Technology

NMT	Age (Ma)* (+/- 1σ)	UH	Age (Ma)* (+/- 1σ)
	6.76 +/- 0.05		6.81 +/- 0.09
	6.81 +/- 0.06		6.82 +/- 0.10
	6.82 +/- 0.05		6.86 +/- 0.09
	6.84 +/- 0.06		6.87 +/- 0.09
	6.87 +/- 0.06		6.90 +/- 0.09
	6.87 +/- 0.06		6.95 +/- 0.10
	6.89 +/- 0.06		6.95 +/- 0.11
	6.90 +/- 0.06		7.03 +/- 0.11
Average:	6.85 +/- 0.05		7.04 +/- 0.01
			7.07 +/- 0.10
		Average:	6.93 +/- 0.09

* Ages at each laboratory lie within 1σ of each other

Table 4. Summary of $^{40}Ar/^{39}Ar$ Ages of the Bearhead Rhyolite

Sample	Location	Geochemical Group	Age (Ma) (+/- 1σ*)
DB	west Bearhead Peak	Main Cluster	6.91 +/- 0.05
EBHP	east Bearhead Peak	Main Cluster	7.06 +/- 0.10
8843P	west Hondo Canyon	Main Cluster	6.88 +/- 0.04
9202P	east of Cerro Pelado	Main Cluster	6.38 +/- 0.09
CB	west of Cerro Belitas	Main Cluster	6.69 +/- 0.04
CP	Cerro Picacho	Main Cluster	6.92 +/- 0.05
CY	Cerrito Yelo	Group 5	6.01 +/- 0.05
CYF	south of Cerrito Yelo	Group 5	6.16 +/- 0.04
NAP	north Aspen Peak	Main Cluster	6.76 +/- 0.10
NBC	north Bland Canyon	Main Cluster	6.74 +/- 0.06
NHC	north Hondo Canyon	Main Cluster	6.57 +/- 0.04
SEAP	southeast Aspen Peak	Main Cluster	7.01 +/- 0.08
TC	east of Tres Cerros	Main Cluster	6.81 +/- 0.05
WBHP	west Bearhead Peak	Main Cluster	6.52 +/- 0.04
31B	southwest Peralta Canyon	Main Cluster	6.99 +/- 0.10
ERP	east Ruiz Peak	Main Cluster	6.67 +/- 0.03
CJ	Cerro La Jara	Main Cluster	6.90 +/- 0.04
PN	Paseo del Norte	Group 3	1.47 +/- 0.04
RH	Rabitt Hill	Main Cluster	6.65 +/- 0.03
SM	San Miguel Mountain	Main Cluster	6.80 +/- 0.05

* 0.5% error in J included

Two methods are used to assess the homogeneity of analyzed crystal populations and identify juvenile phenocrysts. First, sample means and population standard deviations are calculated. Any samples having an age greater than 2σ from the mean are excluded and a new mean calculated. In this study all analyses of each sample lie within 2σ of each other except: 31B, CJ, RH (possible xenocrysts) and ERP (possible altered sanidine) (Figures 19, 20, and 21). For these samples, either the oldest (for the former) or the youngest (for the latter) analysis is excluded to yield a refined data set. Weighted means of these data sets are then calculated using the inverse of the variance as the weighting factor (Young, 1962). Weighted means are initially calculated using analytical errors only, then a 0.5% J factor error is incorporated by quadratically combining it with the weighted standard error. All phenocryst populations appeared to be comprised of juvenile sanidine except TC, WBHP, 31B, and CJ.

Second, isochron ages are typically calculated to assess the possibility of non-atmospheric trapped Ar. In this study, however, all samples did not have a sufficient spread in radiogenic yield among analyses to define reliable isochrons. For all samples, the weighted mean is thus taken to represent the crystallization age. Because all samples from this study are highly radiogenic ($\%^{40}Ar^* > 95\%$), the correction for atmospheric argon is too insignificant to affect the calculated age (the radiogenic argon drowns out atmospheric argon).

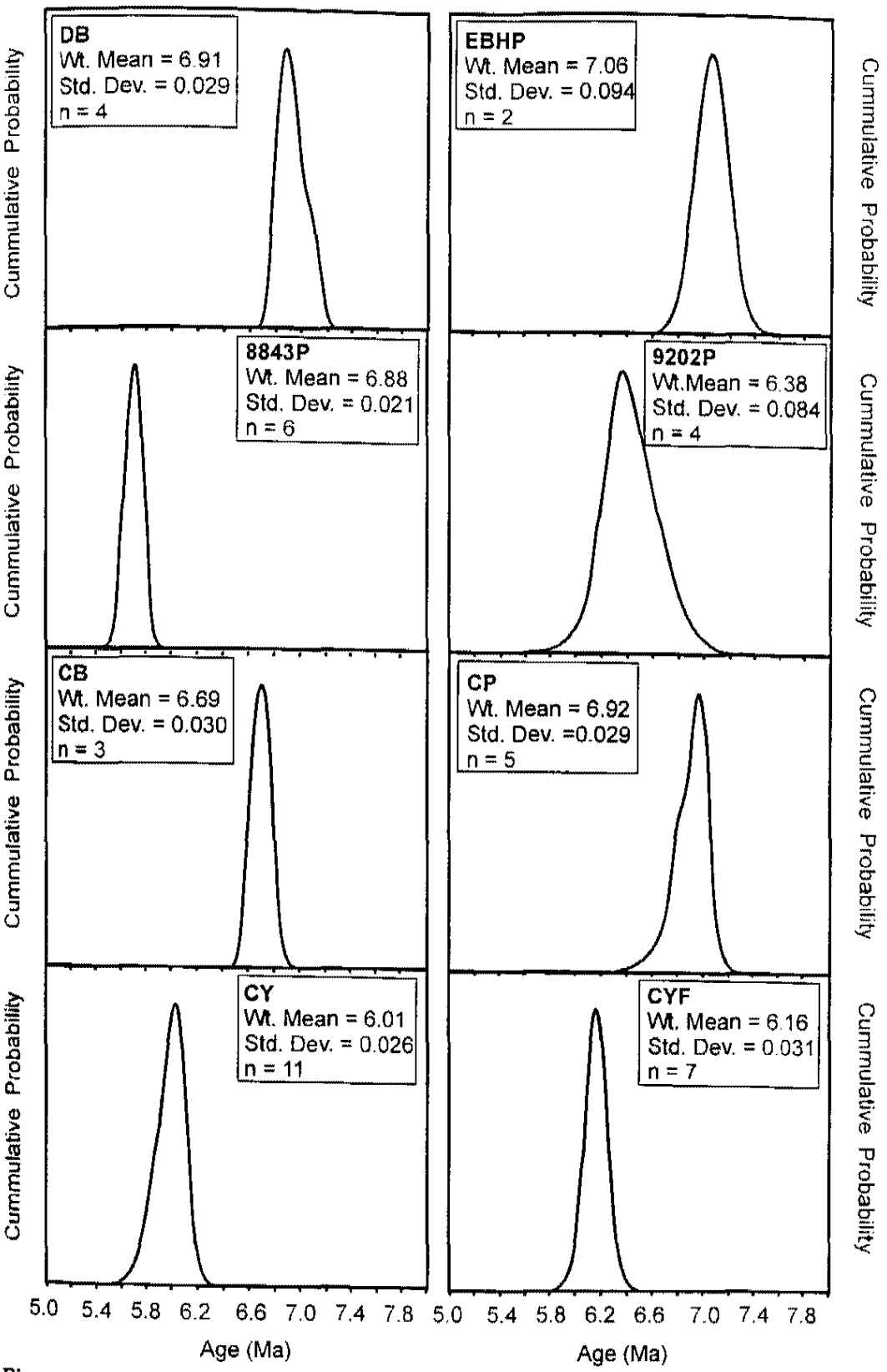

Figure 19. Probability distribution diagrams for the Bearhead Rhyolite $^{40}Ar/^{39}Ar$ analyses. Weighted mean expressed in Ma. Addition of 0.5% error in J not included.

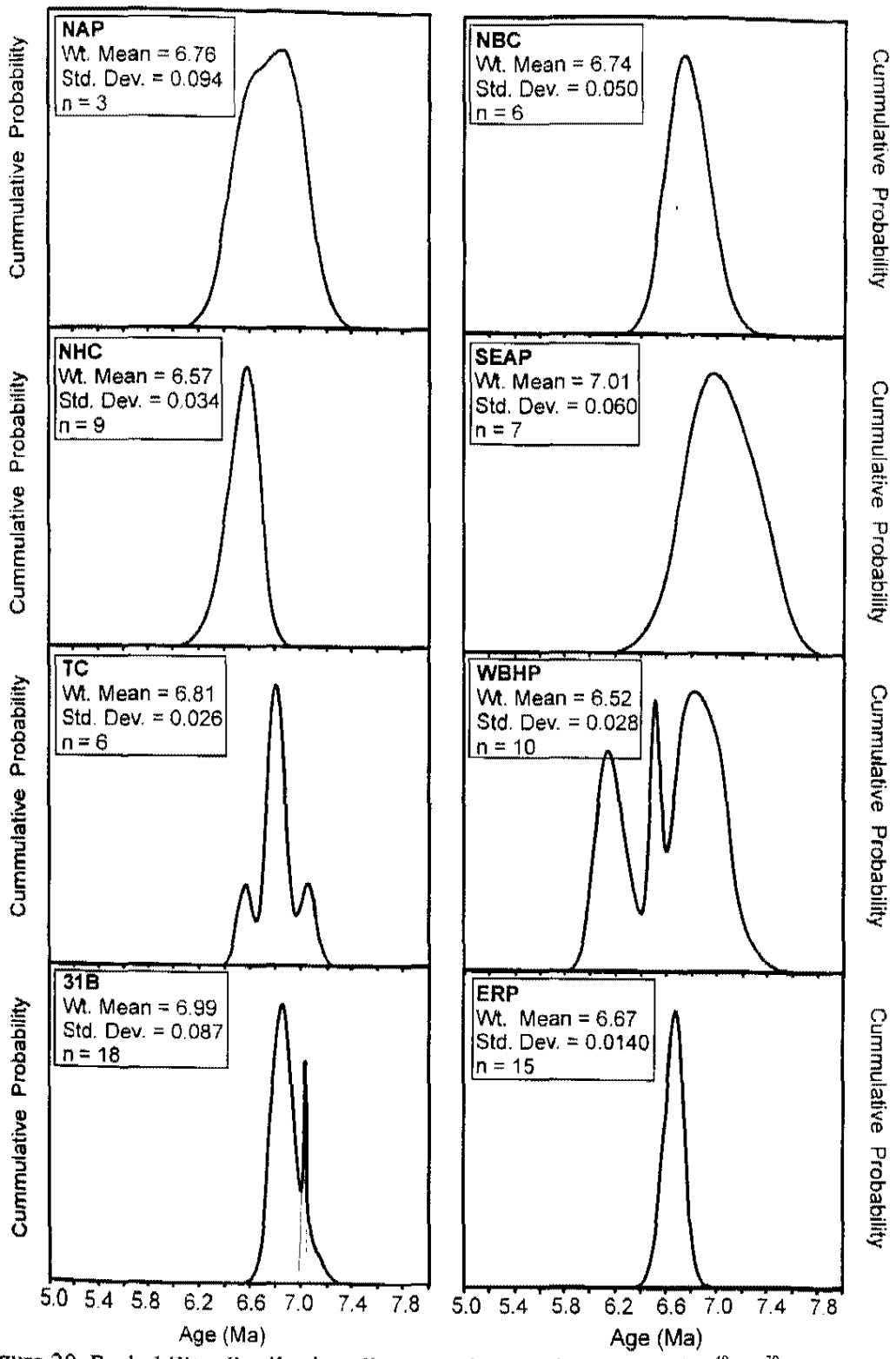

Figure 20. Probability distribution diagrams for Bearhead Rhyolite $^{40}Ar/^{39}Ar$ analyses. Note that sample 31B was analyzed at the University of Houston and New Mexico Institute of Mining and Technology. Weighted mean expressed in Ma. Addition of 0.5% error in J not included. The thin line for sample 31B depicts the sample that lies outside of 2σ of the mean age and was, therefore, omitted from the final age calculation.

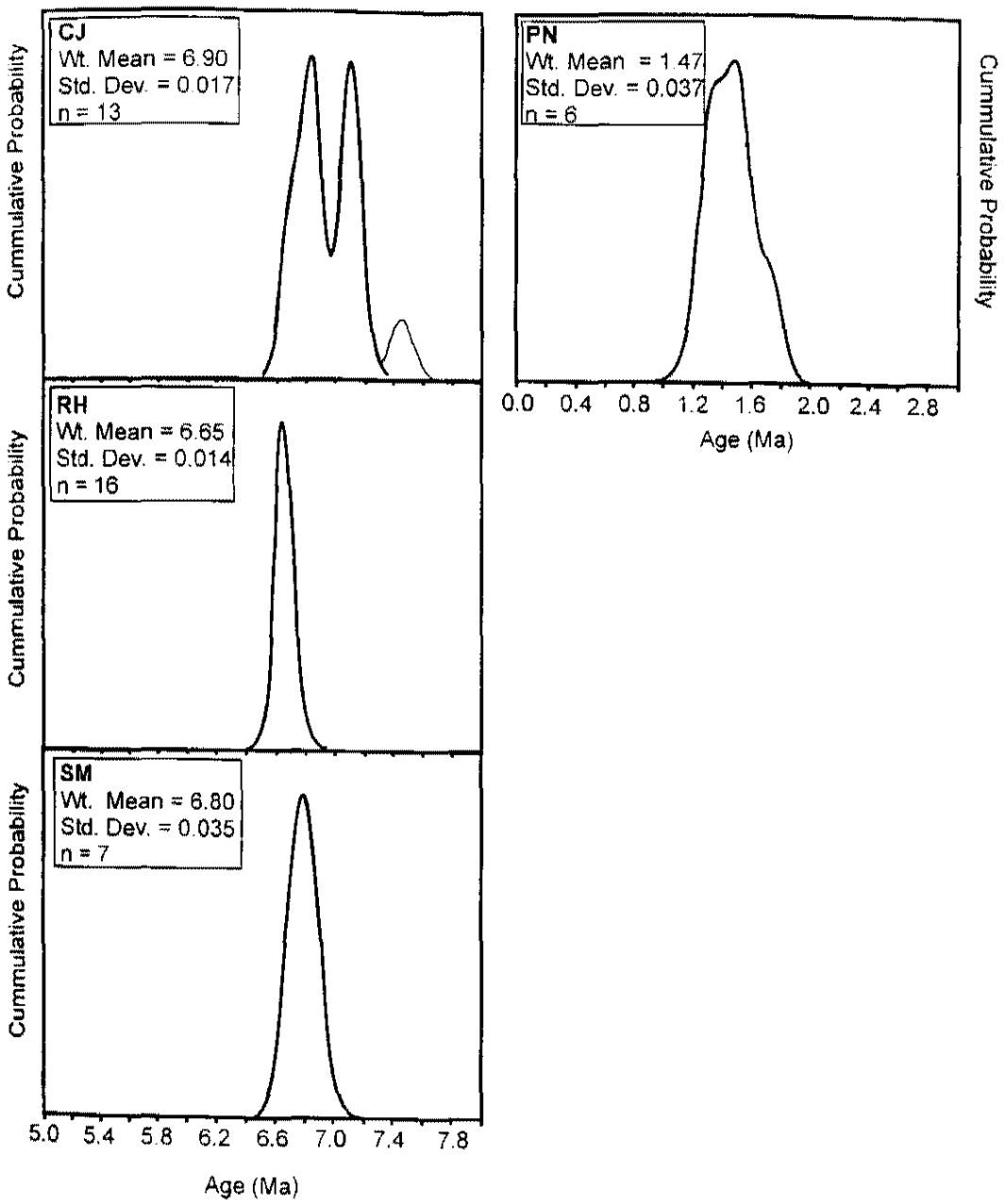

Figure 21. Probability distribution diagrams for the Bearhead Rhyolite $^{40}Ar/^{39}Ar$ analysis. Note that sample PN is too young to be Bearhead Rhyolite. Thicker curved line is data that lies within 2σ of the mean age of the sample. The thinner curved line depicts an analysis that lies outside of 2σ and was, therefore, omitted from the final age calculation. Weighted mean expressed in Ma. Addition of 0.5% error in J not included.

Temporal Correlation of Bearhead Rhyolite Domes to the Peralta Tuff Member

It is often difficult to discern which rhyolite domes and tuffs in a volcanic field are related to each other using field relationships alone because of the lack of stratigraphic relations. One of the goals of this study was to use $^{40}Ar/^{39}Ar$ dating to correlate the Peralta Tuff, whose timing relationships are well constrained stratigraphically, to Bearhead Rhyolite domes that are chemically related to the Peralta Tuff. However, this study is unable to correlate a specific Bearhead Rhyolite dome to a specific Peralta Tuff unit because the resolution of the $^{40}Ar/^{39}Ar$ dating technique is not high enough for ~6 Ma rocks (Figure 22). With a fair amount of confidence, though, it is possible to correlate some Bearhead Rhyolite domes with the lower or upper portion of the Peralta Tuff section. Samples EBHP, SEAP, 31, CJ, CP, DB, and 8843P (7.06 ± 0.10, 7.01 ± 0.08, 6.99 ± 0.10, 6.90 ± 0.04, 6.92 ± 0.05, 6.91 ± 0.05, and 6.88 ± 0.04 Ma, respectively) correlate with samples TWM and CC located in the lower portion of the Peralta Tuff (6.96 ± 0.10 Ma). Samples TC, SM, NBC, CB, ERP, and RH (6.81 ± 0.05, 6.80 ± 0.05, 6.74 ± 0.06, 6.69 ± 0.04, 6.67 ± 0.03, and 6.65 ± 0.03 Ma, respectively) correlate with samples CAN, TE, and CC located in the upper portion of the Peralta Tuff (6.75 ± 0.09 Ma). Samples NHC, WBHP, and 9202P (6.57 ± 0.04, 6.52 ± 0.04, and 6.38 ± 0.09 Ma, respectively; located in the western part of the dome field) are too young to correlate with the dated Peralta Tuff section. Alternatively, samples NAP and RLP (6.76 ± 0.10 and 6.91 ± 0.06 Ma, respectively) may be correlated with all Peralta Tuff units.

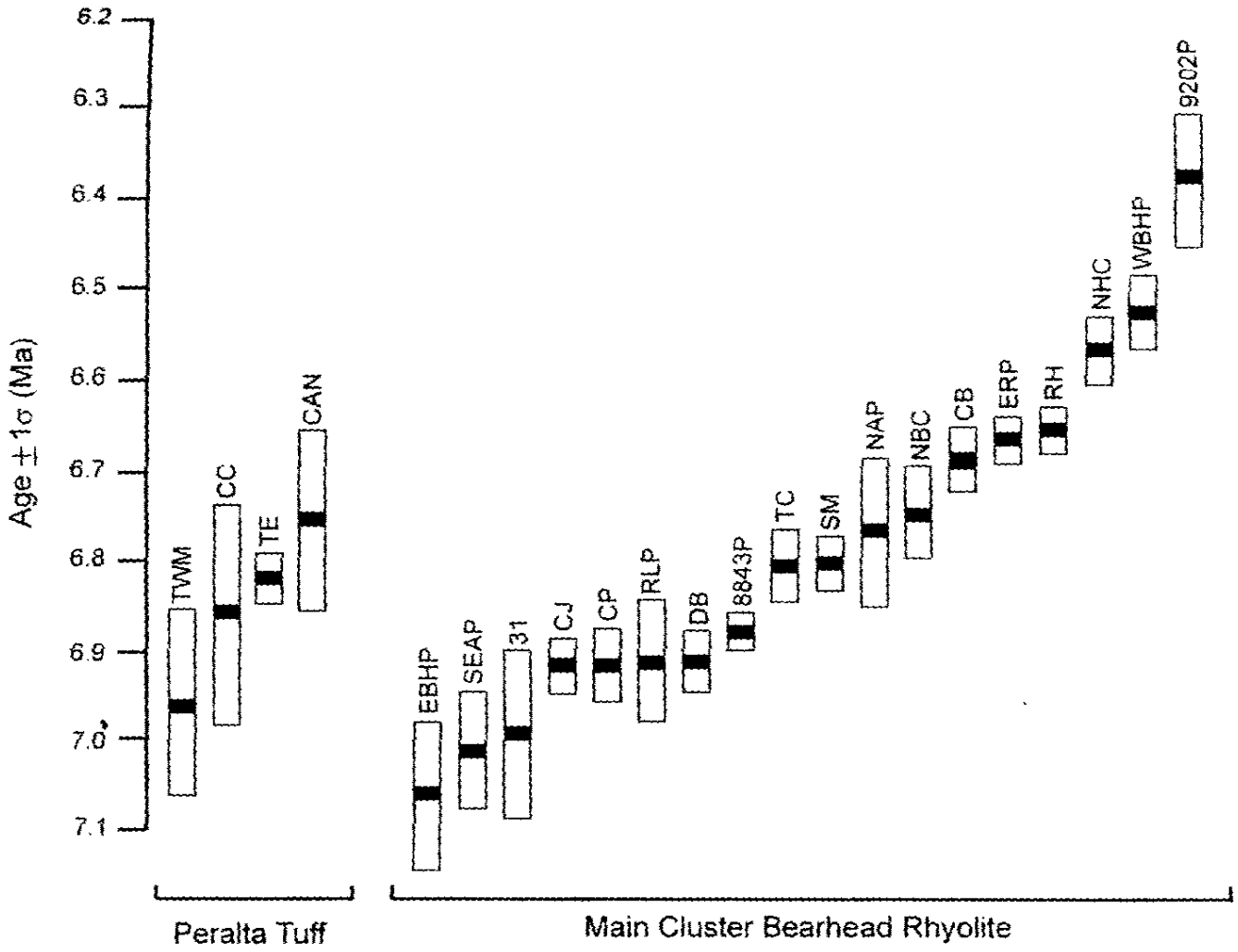

Figure 22. Diagram comparing the $^{40}Ar/^{39}Ar$ ages of the Peralta Tuff to Bearhead Rhyolite of the Main Cluster. Sample means are labled in black. White boxes report 1σ uncertainty. The location [illegible] on the diagram do not imply spatial relationship to the other samples.

Space and Time Trends in the Bearhead Rhyolite Dome Field

While not all geochemical groups discussed in chapter 4 were dated, $^{40}Ar/^{39}Ar$ dates of the Main Cluster, Group 5, and PN indicate that they were erupted at different times. Figure 23 shows the timing of Bearhead Rhyolite dome eruptions based on the ages given in Table 4. The first Main Cluster eruptions, during the interval ~7.06 to 6.80 Ma, occurred more frequently than all later eruptions and includes all dated Peralta Tuff samples. During this interval of time, volcanism geographically spanned the length of the dome field (Figure 24). After this initial period, volcanic activity rapidly decreased until about 6.35 Ma when Main Cluster volcanism had nearly ceased. During this 500 ka interval of time, volcanic activity appears to have shifted northward in four 100 ka eruptive intervals. After a ~250 ka period of quiescence, Group 5 rhyolite domes erupted over a ~200 ka interval in the southwestern portion of the dome field. Without knowing the timing of eruption for Groups 2 and 4, it appears that volcanism in the dome field completely stopped after Group 5 erupted. The dome near Paseo del Norte (PN) was erupted ~5.5 Ma later during Toledo caldera-related volcanism and is thus related to a significantly younger phase of volcanism in the Jemez volcanic field.

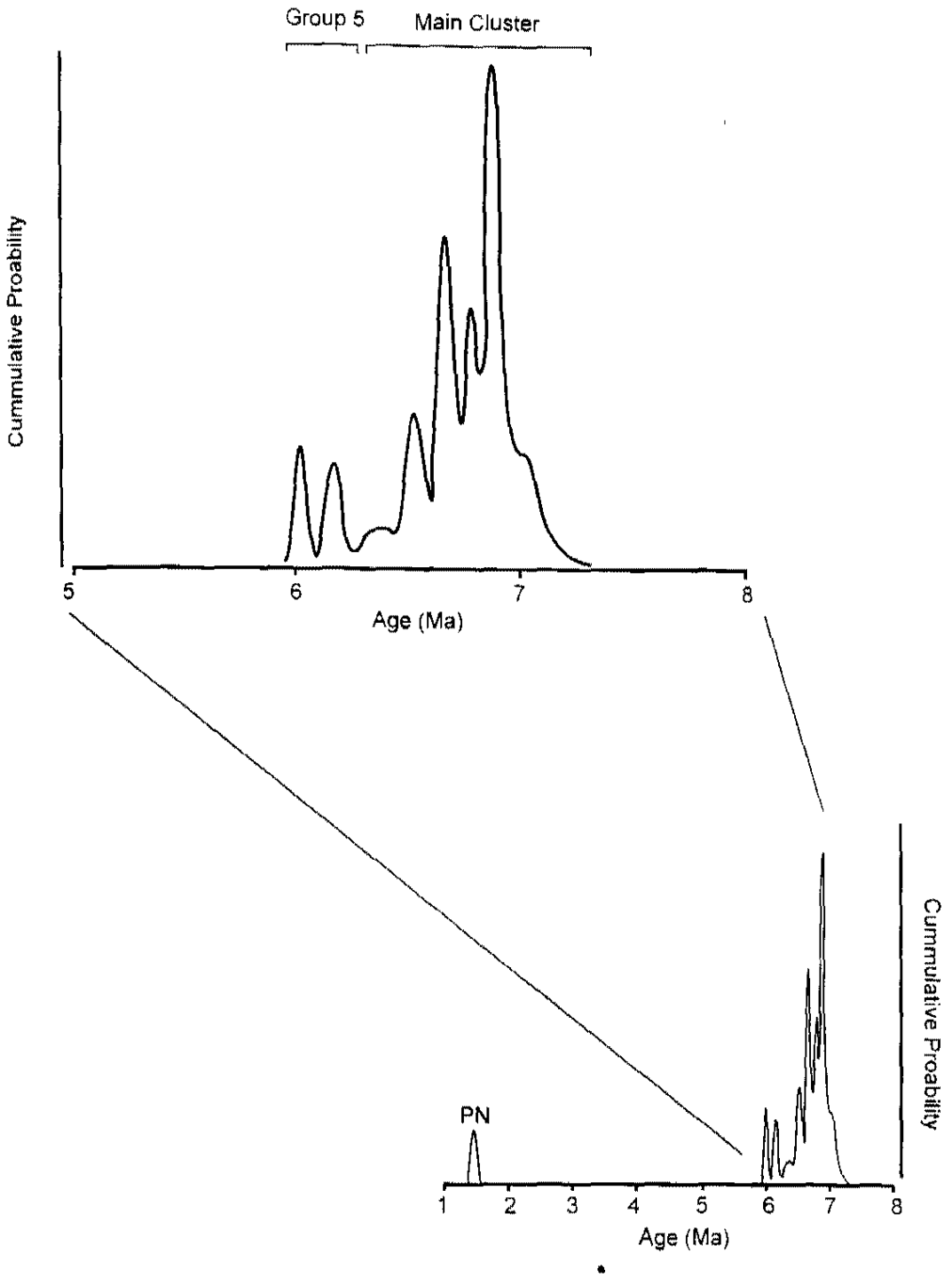

Figure 23. Probability distribution diagram depicting the eruptive periodicity of the Bearhead Rhyolite. Sample ages and standard deviations used are preferred $^{40}Ar/^{39}Ar$ ages and associated errors from Table 4.

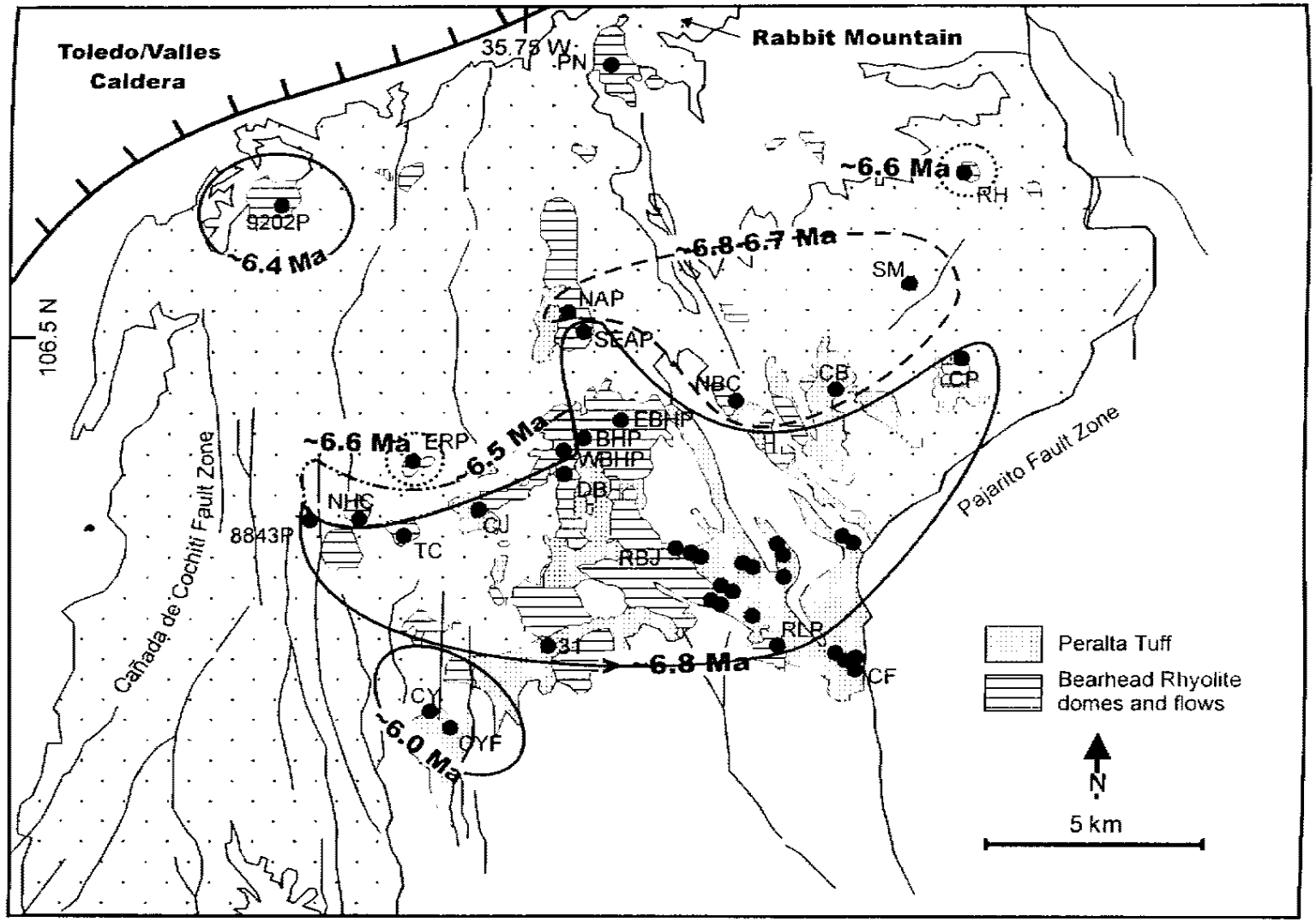

Figure 24. Map of field area depicting space and time relationships between age-constrained BearheadRhyolite. Map after Smith et al. (1970).

CHAPTER 6

INTERPRETATION

The Not So Homogeneous Bearhead Rhyolite

The geochemical (Figures 9, 12, 13, 14, and 15) and geochronologic (Table 4) data presented in chapters 4 and 5 suggests that ~18% of Bearhead Rhyolite samples are chemically and/or temporally not related to the majority of the Bearhead Rhyolite (Main Cluster). These chemically distinct groups are concentrated on the western and southwestern periphery of the dome field (Figure 6). The trachydacites of Group 2 (SHC and NECY) are located on the southwestern periphery and are distinctly phenocryst-rich (27 to 21%). The Toledo-aged (1.47 ± 0.04 Ma) high-silica rhyolite (PN) is located on the northern periphery of the dome field, near the rim of the Toledo/Valles caldera. While PN is temporally related to Toldeo-aged rocks, it is chemically distinct from adjacent Rabbit Mountain (1.43 ± 0.04 to 1.52 ± 0.06 Ma, K/Ar dates on glass and sanidine, Stix et al., 1988) that lies ~1 km east of PN. PN contains significantly higher LREE and significantly lower HREE, LIL, and HFSE concentrations (Table 5). The low-silica rhyolites of Group 4 (GBR, SH1, and SH2) lie along a 10 km N-S trend in the western periphery of the dome field, near the Cañada de Cochiti fault zone. These rhyolites are distinguished from other Bearhead Rhyolite by higher Eu, Hf and Zr

Table 5. Comparison of the Geochemistry of Sample PN With the Rabbit Mountain Rhyolite

	PN	Rabbit Mountain*
SiO_2	75.6	76.9
Al_2O_3	12.5	12.1
TiO_2	0.11	0.08
Fe_2O_3	1.3	1.03
MgO	< 0.1	0.03
CaO	< 0.3	0.3
Na_2O	4.0	4.51
K_2O	4.4	4.42
MnO	0.04	0.07
P_2O_5	< 0.04	0.005
% LOI	1.07	0.59
Total	99.0	100.0
Rb	118	195
Sr	18	<1
Y	28	68
Zr	181	173
Nb	38	97
Cs	1.9	6.9
La	48.7	43
Ce	97.9	83
Nd	42.0	23
Sm	5.8	8.7
Eu	0.15	0.1
Yb	3.4	7.9
Lu	0.45	1
Hf	7.5	8.9
Th	15.7	22
U	5.6	8
Age (Ma)	1.3	1.4

* Sample F80-36 from Stix et al. (1988)

concentrations. The chemically distinct high-silica rhyolites of Group 5 (CY, CYF, and CF) that lie on the southwestern periphery of the dome field are further distinguished by their young age. These rhyolites (6.01 ± 0.05 to 6.16 ± 0.04 Ma) are ~400 ka younger than the Main Cluster. These younger ages agree with CF's stratigraphic position above the Peralta Tuff (Figure 4). In addition to their younger ages, these rocks are more phenocryst-rich than most other Bearhead Rhyolite (16 to 20%, compared to most other units that contain < 6% phenocrysts) (Table 1).

The Isotopic Composition of the Crust and the Bearhead Rhyolite's Source

Alkali and tholeiite basalt from the Jemez, Taos, Mount Taylor, and Zuni-Bandera volcanic fields (which is taken to approximate the composition of mantle-derived magma) contain ε_{Nd} that ranges from -5 to +7.5 and $^{87}Sr/^{86}Sr$ that ranges from 0.7035 to ~0.706 (DePaolo and Wasserburg, 1976; Perry et al., 1987, 1990; Loeffler et al., 1988; Menzies and Kyle, 1990; Dunker et al., 1991; Dungan et al., 1991; Menzies et al., 1991). Exposed Proterozoic granitic rocks in the western United States of the age typical for New Mexico (~1.4 to 1.7 Ga) (which is thought to represent the composition of the lower crust) are characterized by ε_{Nd} of -10 to -15 (DePaolo, 1981; Nelson and DePaolo, 1985; Bennett and DePaolo, 1987) while non-cumulate xenoliths in basalt from southeastern Arizona have $^{87}Sr/^{86}Sr$ 0.706 to 0.710 (Kempton et al., 1990). 1.0 to 1.8 Ga granitic rocks in Colorado, New Mexico, and Arizona have present-day ε_{Nd} between -10 and -15, Nd = 15 to 42 ppm (DePaolo, 1981; Nelson and DePaolo, 1981; Bennett and DePaolo, 1985; Farmer and DePaolo, 1983, 1984; DePaolo et al., 1992) and $^{87}Sr/^{86}Sr$ 0.71 to 1.92

and Sr 480 to 10 ppm, with 95% having $^{87}Sr/^{86}Sr > 0.72$ (Spell et al., 1993). The isotopic range seen in the mantle-derived component, lower, and upper crust imply that the crust is chemically heterogeneous.

Ellisor (1995) reported that the Bearhead Rhyolite contains 0.7075 to 0.7093 $^{87}Sr/^{86}Sr$, 8 to 28 ppm Sr, 0.51235 to 0.51257 $^{144}Nd/^{144}Nd$, 0.022 to 21.81 ppm Nd, 37.13 to 37.68 $^{208}Pb/^{204}Pb$, 15.42 to 15.52 $^{207}Pb/^{204}Pb$, 17.50 to 18.07 $^{206}Pb/^{204}Pb$, and 22 to 28 ppm Pb (Table 6). Based on Sr, Nd, and Pb isotopic modeling Ellisor (1995) concluded that the Bearhead Rhyolite possess an OIB-like mantle source that contains 40 to 80% lower crustal component and was slightly contaminated in the upper crust.

Was the Bearhead Rhyolite Derived from a Single Shallow Magma Chamber?

A fundamental question posed by this study is whether the Bearhead Rhyolite was derived from a single shallow magma chamber or from a series of small batches of unrelated magma that ascended from deeper in the crust. First, was Main Cluster magma derived from a single magma chamber?

The petrologic and geochemical homogeneity (Figure 14) of Main Cluster samples suggest that Main Cluster magma may be derived from a single magma chamber. Because the middle and lower crust underlying the Jemez volcanic field appears to be chemically heterogeneous it seems very unlikely that the Main Cluster was produced from a series of melting events that produced separate but chemically similar batches of Bearhead Rhyolite magma. Another way to examine whether the Main Cluster was derived from a single magma chamber is to try to relate each Main Cluster

Table 6. Sr, Nd, and Pb Isotopic Compositions of the Bearhead Rhyolite from Ellisor (1995)

Sample*	Mg#	$(^{87}Sr/^{86}Sr)_i$	$^{143}Nd/^{144}Nd$	$^{208}Pb/^{204}Pb$	$^{207}Pb/^{204}Pb$	$^{206}Pb/^{204}Pb$	Pb	Sr	Nd	ε_{Nd}
73	10.87	0.7087	0.51235	37.53	15.47	17.85	24	26	18	-5.6
139	5.51	0.7085	0.51257	37.13	15.42	18.07	28	47	0.152	-1.3
144	7.35	0.7088	0.51237	37.68	15.52	17.86	22	16	0.022	-5.2
180	7.45	0.7075	0.51238	37.16	15.52	17.50	25	25	18.88	-5.1
251	0.35	0.7093	0.51236	37.61	15.50	17.84	24	8	21.81	-5.5

ε_{Nd} calculated relative to $(^{143}Nd/^{144}Nd)_{CHUR} = 0.512638$. * = sample number from Ellisor (1995). Corresponding Bearhead Rhyolite samples from this study are TC, NBC, TWM, and TF or TLP.

sample by a geologically reasonable petrogenetic model. The two possbile petrogenetic models are (1) fractional crystallization or (2) assimilation/fractional crystallization.

The following models concentrate on relating the trace element compositions of the Main Cluster because the fractionating phenocryst assemblage of a high silica rhyolite is similar to the remaining melt in major element composition, thus major element composition of the residual melt is not expected to vary during crystallization. In modeling the trace element evolution of the Main Cluster it is important to model the fractionation of allanite, apatite, and zircon because trace elements, in general, and La, Ce, Zr, Hf, and Th, in particular, tend to be strongly partitioned by these accessory minerals (Appendix M) (Cameron and Hanson, 1982; Cameron, 1983; Michael, 1983; Christiansen et al., 1983, 1984, 1986).

Crystal Fractionation

The chemical evolution of Main Cluster samples may be modeled by crystal fractionation alone. For crystal fractionation the invariance of typically strongly compatible or incompatible elements may be viewed as the result of the fractionation of small amounts of allanite, zircon, and magnetite. In this model, allanite, zircon, and magnetite fractionate so that La, Ce, Zr, Hf, and Th cease to behave incompatibly (as they do in less silicic magmas) but do not fractionate in sufficient amounts that La, Ce, Zr, Hf, and Th behave compatibly. Figure 25 shows Rayleigh fractionation trends through the Main Cluster that predicts ~32% fractionation of parental liquid (sample CAN) to account for the most evolved rhyolite (RLP). CAN is modeled as the parental composition because it is the least evolved (i.e., highest concentrations of compatible elements

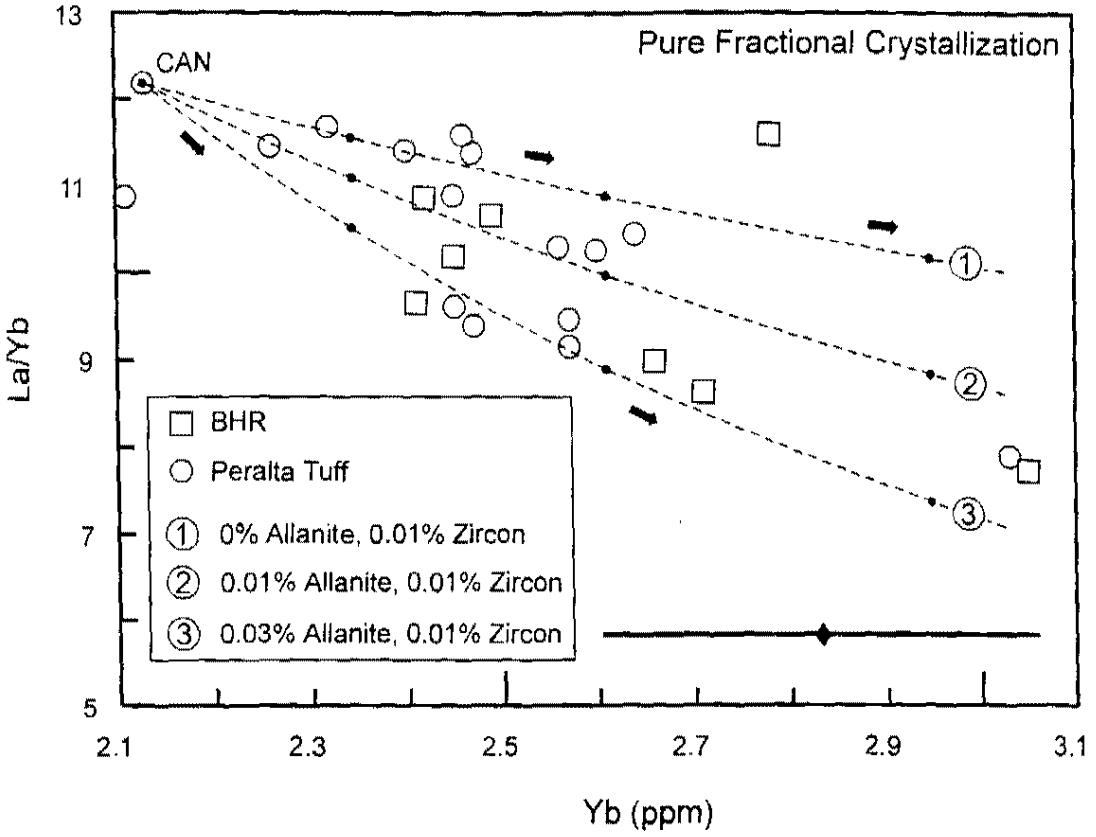

Figure 25. Plot of La/Yb versus Yb showing the relationship between Peralta Tuff and Bearhead Rhyolite within the Main Cluster. BHR = Bearhead Rhyolite. The dashed lines indicate hypothetical Rayleigh fractionation trends by removal of 35% Quartz, 60% Sanidine, 1% Plagioclase, 1% Biotite, and varying amounts of Allanite and Zircon. Black dot marks 10% fractionation. Arrows indicate the direction of fractionation for the residual liquids. Error bar depicts $\pm 1\sigma$.

and lowest concentrations of incompatible elements). Trends 1 and 3 (Figure 25) form the envelope of possible fractionating mineral assemblages for the Bearhead Rhyolite. Trend 1 represents the removal of 35% quartz, 60% sanidine, 1% plagioclase, 1% biotite, 0.015% magnetite, and 0.01% zircon. However, this model does not best represent the Bearhead Rhyolite because the petrography indicates that accessory phases such as allanite and apatite are present in Main Cluster rocks. Alternatively, Trend 3 represents the removal of 35% quartz, 60% sanidine, 1% plagioclase, 1% biotite, 0.03% allanite, 0.01% zircon, 0.01% apatite, and 0.015% magnetite. The mineral assemblage in this model does not differ significantly from the mineral assemblages observed in this study and is also typical of high silica rhyolite. The accessory mineral assemblages estimated by bulk distribution coefficient calculations from this study (35% quartz, 60% sanidine, 1% plagioclase, 1% biotite, 0.01% allanite, 0.01% zircon, 0.01% apatite, and 0.025% magnetite) (Table 7) produce a fractional crystallization trend that lies within the fractional crystallization envelope represented by Trends 1 and 3 in Figure 25.

Trace Element Composition of the Upper Crust Beneath the Jemez Volcanic Field

In order to model the Main Cluster using assimilation/fractional crystallization it is necessary to constrain the composition of the upper crust beneath the Jemez volcanic field (Table 8). To characterize the composition of the upper crust, this study considers Proterozoic granite exposed along the Rio Grande rift (Condie, 1978) and felsic gneiss underlying the Jemez volcanic field (Brookins and Laughlin, 1983). To arrive at more accurate upper crustal compositions, all locations selected for this study lie within a

Table 7. Bulk Distribution Coefficients for the Bearhead Rhyolite and Peralta Tuff

Element	Main Cluster
Sc	0.41
Rb	0.24
Sr	2.66
Y	0.12
Zr	0.71
Nb	0.19
Cs	0.03
Ba	6.07
La	0.97
Ce	0.84
Sm	0.41
Eu	3.20
Tb	0.24
Yb	0.09
Lu	0.10
Hf	0.44
Ta	0.05
Th	0.40
U	0.05

Bulk distribution coefficients were calculated based on the mineral assemblage listed below. The mineral assemblage is based on observed mineral modes of the Bearhead Rhyolite and Peralta Tuff and the observed behavior of each element on the trace element versus Nb plots (Figures 10 and 11) in Chapter 4. The AFC and crystal fractionation models presented in this chapter are based on variations in the amount of zircon, allanite, apatite, and magnetite fractionating while quartz, sanidine, plagioclase, and biotite have little effect on the trace element behavior of rhyolite (see partition coefficients in Appendix M). Typically accessory phases allanite, zircon, apatite, and magnetite drive the compositional changes of high-silica rhyolite (see partition coefficients in Appendix M).

Mineral Assemblage

	Quartz	Sanidine	Plag	Biotite	Zircon	Allanite	Apatite	Mag
Main Cluster	0.35	0.60	0.10	0.10	0.0001	0.0001	0.0001	0.025

Table 8. Possible Upper Crustal Reservoirs Underlying the Jemez Volcanic Field

Sample	1	2	3	4	5	6	7	8	9
SiO_2	72.3	73.4	65.6	76.5	75.0	70.2	73.3	69.2	66.3
TiO_2	0.50	0.51	0.79	0.09	0.17	0.55	0.46	0.76	1.03
Al_2O_3	14.1	12.9	14.3	13.4	14.2	15.3	14.1	13.7	13.9
Fe_2O_3	3.21	3.24	6.42	1.25	1.14	3.21	3.03	4.81	6.85
MnO									
MgO	1.18	0.76	2.50	0.15	0.07	0.48	0.64	1.00	1.33
CaO	1.86	1.72	2.82	0.90	0.89	1.41	1.70	2.75	3.73
Na_2O	3.14	3.38	3.31	3.00	2.71	3.06	2.99	3.29	3.11
K_2O	3.20	3.58	3.78	4.21	5.32	5.27	3.29	3.99	3.25
P_2O_5									
Cs	5.7	7.7	5.9	4.2	7.8	1.6	11.0	8.3	7.6
Rb	137	118	137	149	223	190	150	192	150
Ba	600	750	1570	1060	870	1790	790	840	790
Sr	214	218	510	77	160	386	182	241	228
Th									
U									
La	37	35	32	27	20	95	35	62	49
Ce	86	82	88	67	54	300	81	140	118
Nd									
Sm	8.4	8.4	9.6	7.1	4.9	31.0	7.6	13.0	11.0
Eu	0.9	1.4	1.7	0.5	1.3	3.5	1.5	3.1	2.9
Tb	1.2	1.3	1.0	0.5	0.6	1.8	1.5	2.3	1.9
Yb	4.1	4.2	2.0	1.9	1.7	3.5	4.0	4.9	4.1
Lu	0.75	0.68	0.30	0.34	0.29	0.50	0.61	0.79	0.64
Zr	208	229	302	190	133	453	249	364	365
Nb									
Hf									
Ta									
Sc									
Zn									

Granite from (1) Nacimiento; (2) San Miguel; (3) Penasco; (4) Pecos; (5) Joaquin: (6) Gallinas; (7) Rana; (8) Sandia North; (9) Sandia South in Condie (1978).

Table 8. Possible Upper Crustal Reservoirs Underlying the Jemez Volcanic Field (cont.)

Sample	10	11	12	13	14
SiO_2	63.86	72.08	55.10	65.05	77.43
TiO_2	0.97	0.19	1.44	0.56	0.11
Al_2O_3	14.57	14.20	15.54	16.00	11.98
Fe_2O_3	3.10	0.67	1.87	1.13	0.34
MnO	0.092	0.050	0.140	0.079	0.015
MgO	1.41	0.45	4.67	1.46	0.03
CaO	3.24	1.12	5.14	3.15	0.69
Na_2O	3.30	3.33	2.87	4.50	3.43
K_2O	4.18	4.73	3.31	2.89	4.68
P_2O_5	0.59	0.05	0.51	0.18	< 0.01

Precambrian rocks from drill hole GT-2 JVF (10) av. biotite granodiorite; (11) av. Leucocratic monzogranitic dike; (12) av. Ferrohastingsite-biotite schist; (13) biotite granodioritic gneiss; and (14) leucocratic monzogranitic gneiss in Brookins and Laughlin (1983).

100 km radius of the Jemez volcanic field. The chemistry of the selected Proterozoic granitic plutons suggests that the upper crust is moderately homogeneous and varies from intermediate to felsic compositions (Table 8). The closest granites to the Jemez volcanic field are from Nacimiento, San Miguel, and Joaquin Mountains along the western boundary of the Valles caldera (Figure 26). Chemical data on the average compositions of biotite granodiorite, leuocratic monzogranitic gneiss, and ferro-hastingsite-biotite schist underlying the Valles caldera are also included (Brookins and Laughlin, 1983).

Assimilation and Fractionation

In an assimilation and fractionation model the small chemical variation of typically strongly compatible or incompatible elements (Figure 27) may be modeled by the fractionation of very small amounts of allanite, zircon, and magnetite. In this model, allanite, zircon, and magnetite fractionate so that La, Ce, Zr, Hf, and Th cease to behave incompatibly (as they do in all other, less evolved magma) but do not fractionate in sufficient amounts that La, Ce, Zr, Hf, and Th behave compatibly (Table 7). Assimilation of upper crustal wall rock is limited such that only Sr-isotopes ($^{87}Sr/^{86}Sr$ = 0.7075 to 0.7093) (Ellisor, 1995) are affected due to the low concentration of Sr in the Bearhead Rhyolite (8-47 ppm). The AFC model depicted in Figure 27 shows that the chemical variation observed in the Main Cluster can be predicted by assimilating ~ 0.03% (R = 0.01) upper crustal granite (73.4 wt.% SiO_2) and ~5 to 35% fractionation of a parental melt represented by CAN. Trend 1 represents the removal of 35% quartz, 60% sanidine, 1% plagioclase, 1% biotite, 0.015% magnetite and no other accessory phases and 0.03% assimilation. However, this model does not best represent the Bearhead Rhyolite

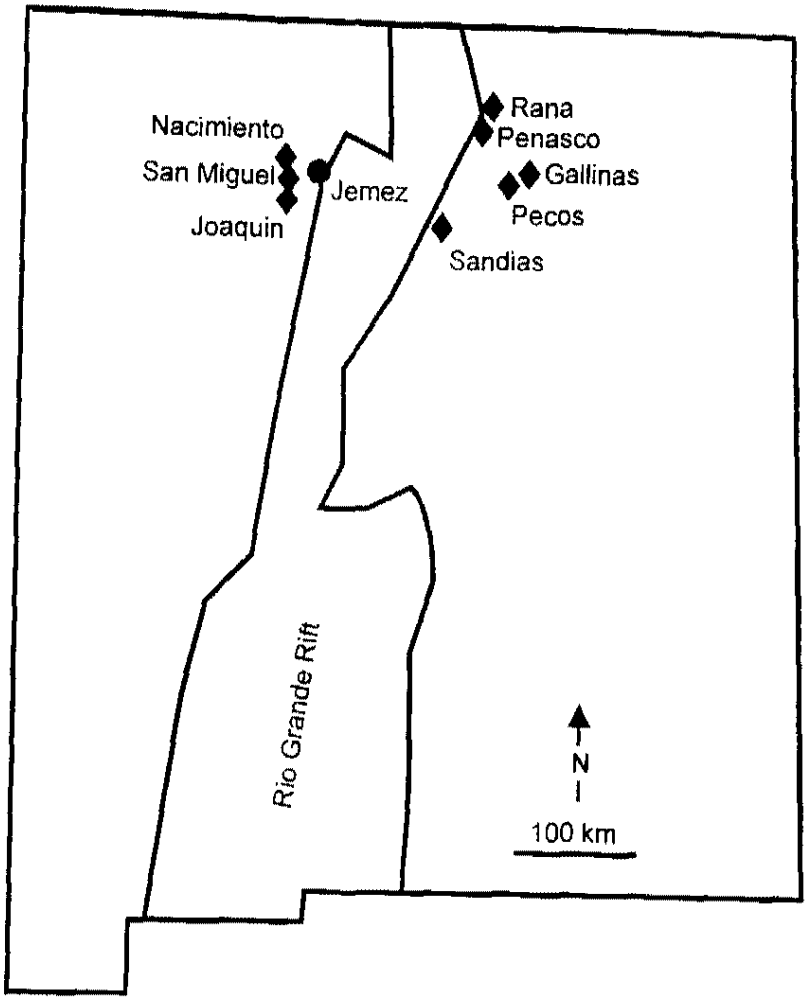

Figure 26. Map showing the sample locations of granite that may represent the chemical composition of the upper crust underlying the Jemez Volcanic Field.

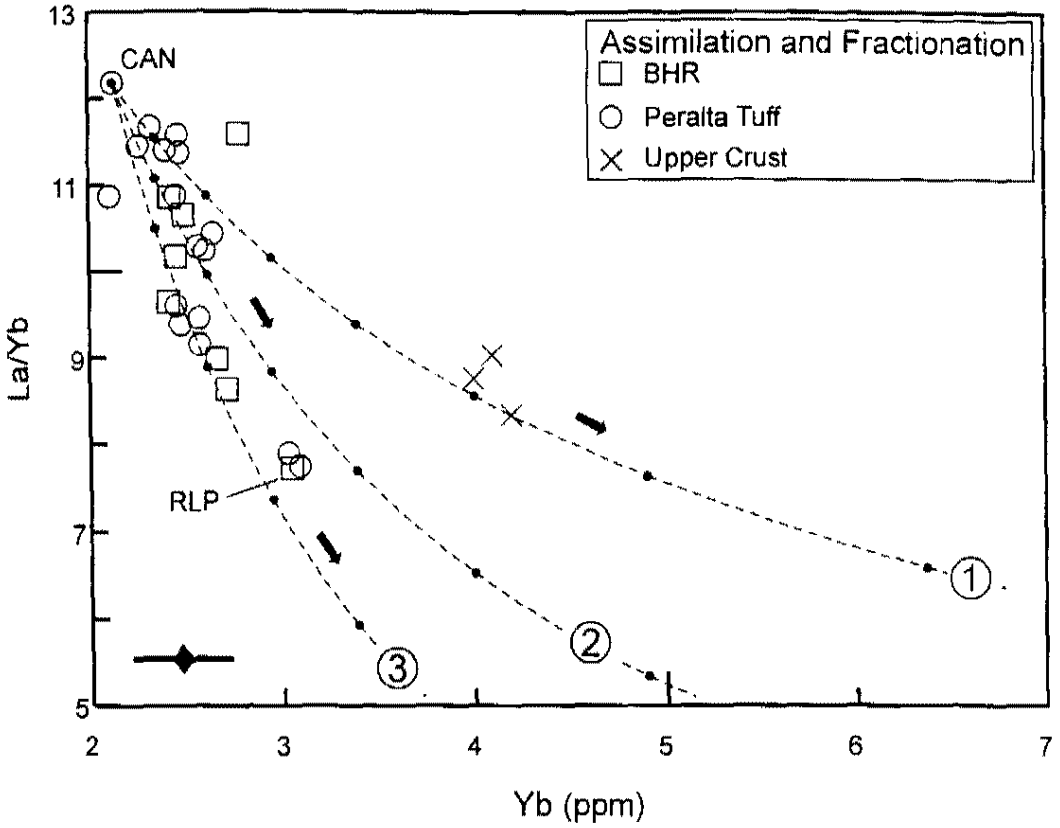

Figure 27. Plot of La/Yb versus Yb showing the relationship between Peralta Tuff and Bearhead Rhyolite within the Main Cluster. BHR = Bearhead Rhyolite. The dashed lines indicate hypothetical assimilation/fractionation trends (with 10% crystal fractionation marked by solid circles) by 0.03% assimilation of upper crustal granite (R = 0.01) and removal of 35% Quartz, 60% Sanidine, 1% Plagioclase, 1% Biotite and: (1) 0.015% Magnetite and no other accessory phases; (2) 0.01% Allanite, 0.01% Zircon, 0.01% Apatite, and 0.025% Magnetite; or (3) 0.06% Allanite, 0.01% Zircon, 0.01% Apatite, and 0.025% Magnetite and 0.03% assimilation of upper crustal granite from Nacimiento, San Miguel, and Rana (data from Condie, 1985) (Samples 1, 2, and 7 from Table 7). Arrows indicate direction of assimilation and fractionation for the residual liquids. Error bar depicts $\pm 1\sigma$.

because the petrography indicates that allanite, apatite, and zircon are present in Main Cluster rocks. Alternatively, Trend 3 represents the removal of 35% quartz, 60% sanidine, 1% plagioclase, 1% biotite, 0.06% allanite, 0.01% zircon, 0.01% apatite, and 0.025% magnetite and ~0.03% assimilation. Trend 2 is based on the mineral assemblage observed in this study.

AFC calculations (DePaolo, 1981) that simultaneously consider all trace elements predict the trace element abundances observed in the Main Cluster's most evolved sample (RLP) using 10 to 15% fractional crystallization (Table 9). The AFC model calculated for the Main Cluster (based on the fractionation of 35% quartz, 60% sanidine, 1% plagioclase, 1% biotite, 0.01% allanite, 0.01% zircon, 0.01% apatite, and 2.5% magnetite and a mass ratio (R) of 0.01) fits well with the observed trend for all trace elements except Rb, Zr, Nb, Cs, Eu, and Th. When analytical errors and variation within eruptive units are taken into account these discrepancies are not significant. The higher concentrations of Rb, Zr, Nb, Cs, and Th predicted by the AFC model may be the result of bulk distribution coefficients that are too low for RLP while the lower concentration of Eu predicted by the AFC model may be the result of a bulk distribution coefficient that is too high for RLP. The AFC model that considers all trace elements (Table 9) requires less fractional crystallization to predict the chemistry of RLP than the La/Yb versus Yb AFC models shown in Figure 27. The La/Yb versus Yb model may be more sensitive to the presence or absence of allanite in an individual sample. For RLP, then, the analyzed sample may contain fewer allanite crystals resulting in a smaller La/Yb ratio that suggests more fractionation. Despite these discrepancies in crystal fractionation percentages,

Table 9. AFC Model for the Main Cluster Considering all Trace Elements

	Observed Parent	Predicted Daughter % Fractionation		Observed Daughter
(ppm)	(CAN)	10%	15%	(RLP)
Sc	2.9	3.1	3.2	3.2
Y	22	24	25	26
Zr	83	86	87	74
Nb	34	37	39	22
La	26	24	23	24
Ce	49	47	46	49
Sm	3.7	3.8	3.9	4.1
Eu	0.4	0.3	0.3	0.5
Tb	0.6	0.6	0.7	0.6
Yb	2.1	2	2	3
Lu	0.3	0.3	0.3	0.4
Hf	3.5	3.7	3.8	3.7
Ta	2.3	2.5	2.7	2.9
Th	12.2	12.8	13.2	11.5
U	4.4	4.9	5.1	4.7

Calculations based on the AFC equation of DePaolo (1981)
R = 0.01, or 0.03% assimilation

both AFC models are in reasonable agreement with each other and both predict the observed composition of RLP using realistic parameters.

AFC or Crystal Fractionation?

Either the fractionation or fractionation-dominated AFC model predicts the trace element trends observed in the Bearhead Rhyolite using mineral assemblages very similar to those observed and reasonable degrees of fractionation and assimilation. However, the pure fractionation model does not account for $^{87}Sr/^{86}Sr$ isotope data (Table 6) (Ellisor, 1995) which suggests felsic upper crust contaminated the magmas. The fact that the crystal fractionation and AFC models both effectively explain the same data set may be attributed to the small amount of assimilation of felsic upper crust.

Was Main Cluster Magma Derived from a Shallow Magma Chamber?

The geochemical data and AFC model imply that the Main Cluster was derived from a single large magma chamber, but was it a shallow (i.e., $\leq$ 10 km below Earth's surface) magma chamber? K/Ar age data on hydrothermal illite reported by WoldeGabriel and Goff (1989) suggests that a hydrothermal event occurred 8.07 $\pm$ 0.22 to 5.60 $\pm$ 0.29 Ma in northern to central portion of the Bearhead Rhyolite dome field (Figure 28). The timing and location of the hydrothermal event coincides with the eruption of the Bearhead Rhyolite implying that the Main Cluster was derived from a shallow magma chamber. Secondly, there are mechanical/thermal problems with moving

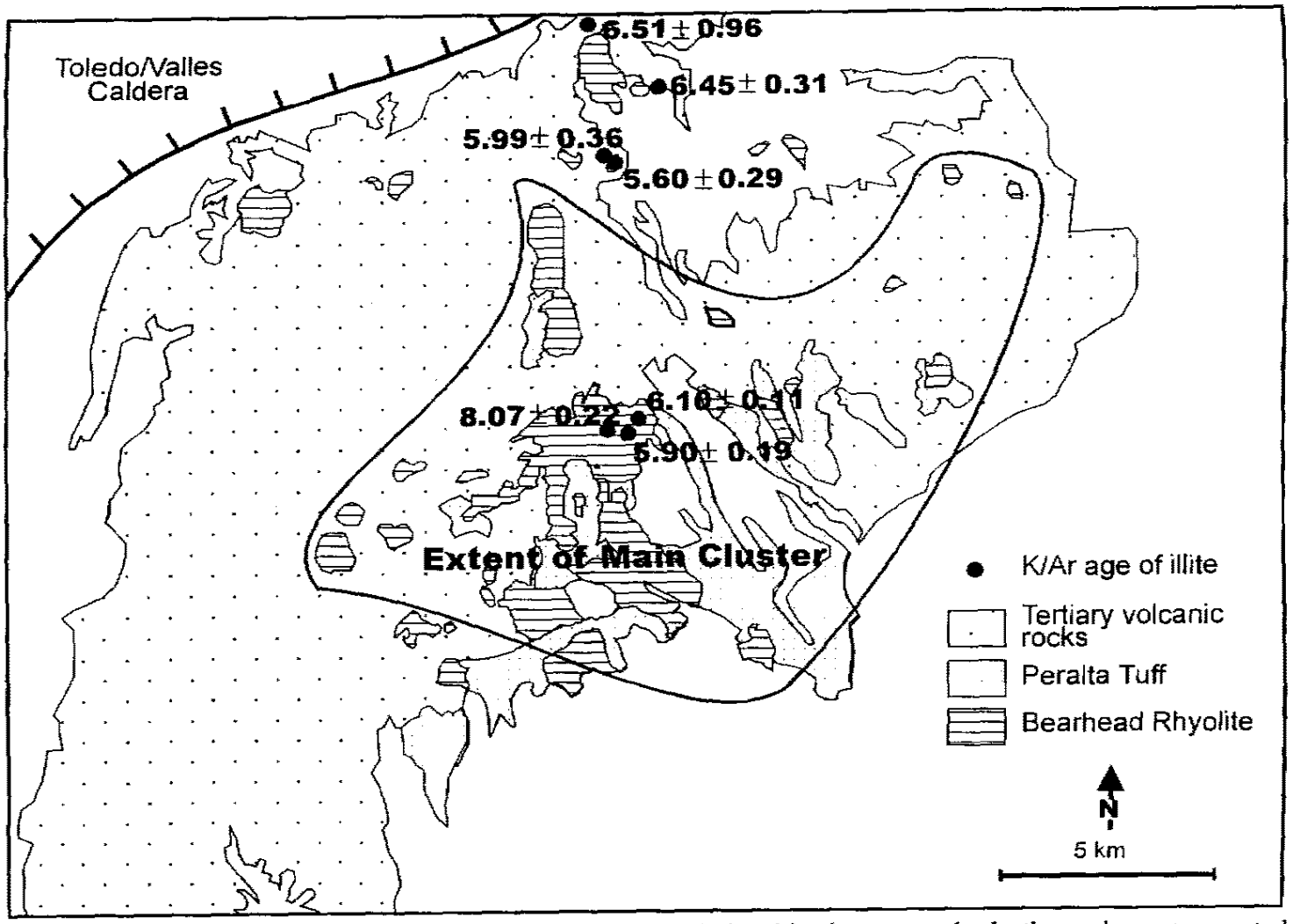

Figure 28. Map of field area depicting the space and time relationships between a hydrothermal event reported by WoldeGabriel and Goff (1989) and the Bearhead Rhyolite. Map after Smith et al. (1970).

small (a few km^3) magma batches from the middle or lower crust that do not exist for magma derived from a shallow magma chamber.

The 680 ka Lifespan of the Bearhead Rhyolite Magma Chamber

Typically, shallow silicic systems reside in the upper crust ≤ ~200 ka before they become too crystalline to erupt. The $^{40}Ar/^{39}Ar$ data obtained by this study, however, implies that the Bearhead Rhyolite resided in the upper crust for a significantly longer, ~680 ka, amount of time. This long residence time seems possible if the magma had an underlying heat source. While there is no textural evidence that the Bearhead Rhyolite magma was heated (e.g., resorbed and/or rimmed phenocrysts) it is possible that the hydrothermal system present in the dome field around the time of Bearhead Rhyolite eruptions could have been a source of heat.

Role of Tectonism in the Eruptive Style of the Bearhead Rhyolite

There are two explanations for effusive eruption of high-silica magma: (1) low volatile content of the magma or (2) tectonic venting of magma by faults before it can explosively erupt (Eichelberger et al., 1986). Ion microprobe data on melt inclusions in quartz from the Peralta Tuff suggests that the volatile content of the Bearhead Rhyolite magma (2 to 5.5 wt.% H_2O) was comparable to the caldera-forming Bandelier Tuff (1 to 6 wt.% H_2O) and, therefore, was likely capable of erupting explosively (Figure 29).

Could tectonism, then, have played a role in the effusive eruption of the Bearhead Rhyolite? The Bearhead Rhyolite dome field is bounded on the west by the Cañada de Cochiti fault zone and bounded on the east by the Pajarito fault zone (Figure 5).

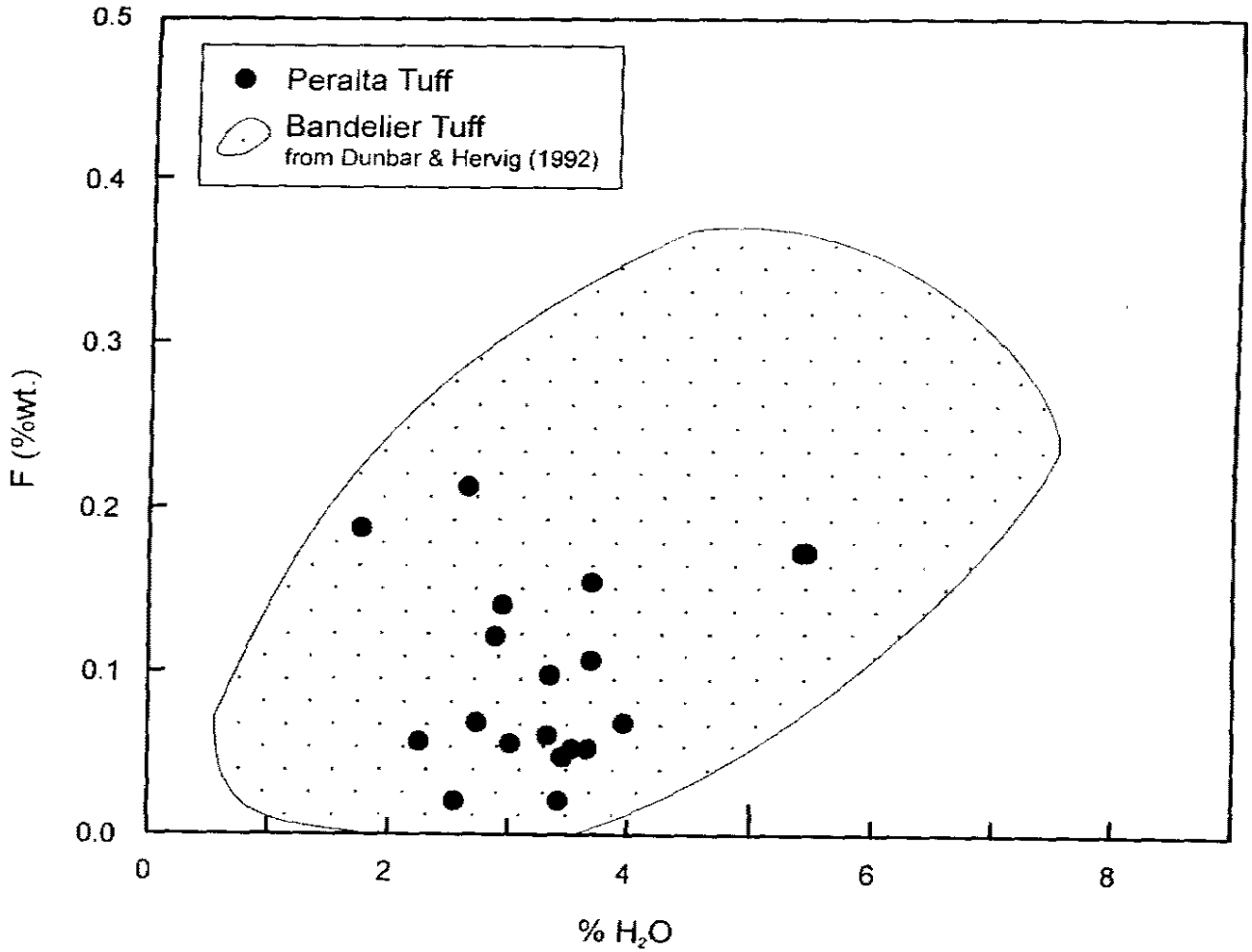

Figure 29. Plot comparing the water content to F content of the Bearhead Rhyolite and the caldera-forming Bandelier Tuff data (n = 134) from Dunbar and Hervig (1992).

Previous workers have suggested that fault activity bounding the western margin of the Española Basin shifted from the north-trending Cañada de Cochiti fault zone to the north- to northeast-trending Pajarito fault zone between 5 to 6 Ma (Manley, 1976, 1979; Golombek, 1981, 1983; Golombek et al., 1983). More recently, G.A. Smith (personal communication, 1998) observed that many Bearhead Rhyolite domes are found at the intersection of faults that form the Bearhead Basin. The close spatial and temporal relationship between extensional faulting and the eruption of the Bearhead Rhyolite implies that tectonism was an important control over the effusive eruption of the Bearhead Rhyolite.

Explaining the Small Degree of Evolution in the Main Cluster's Chemistry

It is not clear what geologic process accounts for the small amount of chemical evolution in the Main Cluster's magma chamber over it's ~680 ka lifetime (Figures 12 and 13). The first possibility is that Main Cluster magma occupied several cupolas in a single magma chamber. With this scenario, Main Cluster magma in each cupola became more or less differentiated than magma in other cupolas so that when each volume erupted there was no chemical progression with time although they all share a common parental melt. This model is appealing because samples of the Main Cluster are found in the highly faulted Bearhead Basin. The Main Cluster's magma chamber may have had an irregular shape caused by upwelling of magma along faults and particularly where faults intersect.

The second possibility is that significant differentiation did occur but this is not evident in many of the trace element plots (e.g., La, Ce, Zr, and Hf) (Figures 12 and 13) because just enough accessory phases such as allanite, apatite, and zircon were fractionating to result in bulk distribution coefficients ~1 (Table 7). This possibility is supported by immobile, very incompatible trace elements such as Y, Yb, and Nb whose concentrations appear to increase ~100% over the 680 ka time interval.

Is the Effusive Eruptive Style of the Bearhead Rhyolite Unusual?

There are only two documented cases of small volumes of silicic magma erupted from large magma chambers that did not produce a caldera-forming eruptions; the rhyolites of Coso volcanic field in the southwest Sierra Nevada Mountains, California and Taylor Creek Rhyolite in the Mogollon-Datil volcanic field, New Mexico. The high-silica rhyolite of Coso consists of 38 rhyolite domes covering ~150 km^2 that were erupted over ~240 ka (K/Ar dates) from a single magma chamber (Bacon et al., 1981). It is estimated that the total volume of the dome and flow units is ~ 1.6 km^3 while only ~0.3 km^3 of pyroclastic material was erupted. Detailed structural studies of the area allowed Bacon et al. (1981) to relate the effusive eruption of the high-silica rhyolite to west-northwest directed Cenozoic extension.

The Taylor Creek Rhyolite consists of 20 high-silca rhyolite domes that were erupted over ~1000 km^2 in ~100 ka ($^{40}Ar/^{39}Ar$ dates) from a single magma chamber. It is conservatively estimated that the total volume of the dome and flow units is ~55 km^3 while ~45 km^3 of pyroclastic material was erupted (Duffield and Dalrymple, 1990). It is less clear why the Taylor Creek Rhyolite did not produce a caldera-forming eruption but

has been attributed to both volatile poor magma (Duffield and du Bray, 1990; Webster and Duffield, 1991) and tectonic leaking of magma (Duffield and Dalrymple, 1990; Duffield and Ruiz, 1992).

The fact that there are only two documented examples of effusive eruptions of silicic magma from sizeable shallow magma chambers implies that the style is unusual. It is possible that this style is not rare, just not recognized when present. This suggests that we may need to expand our conception of sizeable continental silicic systems to include caldera-forming systems as one end-member and effusively erupted dome fields as the other end-member.

Conclusions

In summary, the petrologic, geochemical, and geochronologic data suggest that the majority of the Bearhead Rhyolite (~ 82%) and all of the Peralta Tuff are derived from a single large, shallow magma chamber that erupted over a ~680 ka interval (7.06 ± 0.10 to 6.38 ± 0.09 Ma) at roughly 100 ka intervals. The sufficiently large size of the Bearhead Rhyolite's magma chamber and sufficient (~3 %) volatile content (comparable to the volatile content of the Bandelier Tuff) suggests that the Bearhead Rhyolite was capable of producing a caldera-forming eruption. The Bearhead Rhyolite magma chamber may have failed to produce a caldera-forming eruption because it was vented by any of the numerous faults that intersect the dome field. The apparent lack of significant chemical variation within the Bearhead Rhyolite over ~680 ka may imply that small volumes of magma were physically separated from each other by fault-formed cupolas in the roof of the magma chamber. Alternatively, it is possible that Bearhead Rhyolite

magma did significantly differentiate as indicated by the ~100% increase in immobile and very incompatible trace element such as Y, Yb, and Nb. Limited change in other trace elements (La, Ce, Zr, Hf, and Th) may be due to the fractionation of small amounts of accessory phases such as allanite, apatite, and zircon that resulted in bulk distribution coefficients ~1. The magma chamber's long ~680 ka residence time in the upper crust may have been made possible by an underlying heat source underlying (even though no evidence was seen for underplating this in this study).

The remaining 18% of Bearhead Rhyolite forms three chemically and/or temporally distinct groups that are located along the southwestern and western periphery of the dome field. The chemically distinct dome at Cerrito Yelo (CY, CYF) was erupted from 6.16 ± 0.04 to 6.01 ± 0.05 Ma while trachydacite domes (SHC, NECY) and a low-silica rhyolite dome (GBR) are located just northwest of Cerrito Yelo. A rhyolite dome erupted at 1.47 ± 0.04 Ma located in the northern periphery of the dome field (Paseo del Norte) is related to the Toledo caldera but is chemically distinct from a nearby Toledo caldera-aged rhyolite dome from Rabbit Hill. The lack of geochronologic control and/or limited number of samples makes it difficult to constrain how these magmas evolved chemically.

Further Study

Because this study is the first detailed examination of the Bearhead Rhyolite, much more work is needed to understand the role the Bearhead Rhyolite played in the evolution of the Jemez volcanic field. Some questions that remain include the following:

- How did the Bearhead Rhyolite's source form and what happened between the formation of its source and the Bearhead Rhyolite's residence in the upper crust?

- Are contemporaneously erupted Paliza Canyon Formation dacites and/or andesites related to the Bearhead Rhyolite?

- What is the relationship between the Canovas Canyon Rhyolite and the Bearhead Rhyolite? Is the distinction between the two arbitrary

- What is the relationship between the groups found within the Bearhead Rhyolite?

REFERENCES

Aldrich, M.J., Jr., 1986, Tectonics of the Jemez lineament in the Jemez Mountains and Rio Grande rift: Journal of Geophysical Research, v. 91, no. B2, p. 1779-1798.

Arth, J.G., 1976, Behavior of trace elements during magmatic processes; a summary of theoretical models and their applications: Journal of Research of the U.S. Geological Survey, v. 4, 41-47 p.

Bacon, C.R., Kurasawa, H., Delevaux, M.H., Kistler, R.W., and Doe, B.R., 1984, Lead and strontium isotopic evidence for crustal interaction and compositional zonation in the source regions of Pleistocene basaltic and rhyolitic magmas of the Coso volcanic field, California: Contributions to Mineralogy and Petrology, v. 85, p. 366-375.

Baldridge, W.S., 1979, Petrology and petrogenesis of Plio-Pleistocence basaltic rocks from the central Rio Grande rift, New Mexico, and their relation to rift structure, *in*, Reicker, R.E., ed., Rio Grande rift: tectonics and magmatism: Washington, D.C., American Geophysical Union, p. 323-353.

Baldridge, W.S., Bartov, Y., and Kron, A., 1983, Geologic map of the Rio Grande rift and southeast Colorado Plateau, New Mexico and Arizona, *in*, Tectonics and Magmatism, ed., Riecker, R.E.: American Geophysical Union, Washington, D.C..

Bailey, R.A., Smith, R.L., and Ross, C.S., 1969, Stratigraphic nomenclature of volcanic rocks in the Jemez Mountains, New Mexico: U.S. Geological Survey, Bulletin 1274-P, 19 p.

Bennett, V.C., and DePaolo, D.J., 1987, Proterozoic crustal history of the western United States as determined by neodymium isotopic mapping: Geological Society of America Bulletin, v. 99, p. 674-685.

Brookins, D.G. and, and Laughlin, A.W., 1983, Rb-Sr geochronologic investigations of Precambrian samples from deep geothermal drill holes, Fenton Hill, New Mexico: Journal of Volcanology and Geothermal Research, v. 15, p. 43-58.

Cameron, K.L., and Hanson, G.N., 1982, Rare earth element evidence concerning the origin of voluminous mid-Tertiary rhyolitic ignimbrites and related volcanic volcanic rocks, Sierra Madre Occidental, Chihuahua, Mexico: Geochimica et Cosmochimica Acta, v. 46, p. 1,489-1,503.

Cameron, K.L., 1983, The Bishop Tuff revisited: Isotope dilution REE data consistent with crystal fractionation: EOS, v. 64, p. 883.

Cebula, G.T., Kunk, M.J., Mehnert, H.H., Naeser C.W., Obradovich, J.D., and Sutter, J.F., 1967, The Fish Canyon Tuff, a potential standard for the $^{40}Ar/^{39}Ar$ and fission-track dating methods: Terra Cognita, v. 6, no. 2, p. 139-140.

Christiansen, E.H., Burt, D.M., Sheridan, M.F., and Wilson, R.T., 1983, Petrogenesis of topaz rhyolites from the western United States: Contributions to Mineralogy and Petrology, v. 83, p. 16-30.

Christiansen, E.H., Bikun, J.V., Sheridan, M.F., and Burt, D.M., 1984, Geochemical evolution of topaz rhyolites from the Thomas Range and Spor Mountain, Utah: American Mineralogist, v. 69, p. 223-236.

Christiansen, E.H., Sheridan, M.F., and Burt, D.M., 1986, The geology and geochemistry of Cenozoic topaz rhyolites from the western Unites States: Geological Society of America Special Paper 205, 82 p.

Condie, K.C., 1978, Geochemistry of Proterozoic granitic plutons from New Mexico, USA: Chemical Geology, v. 21, p. 131-149.

DePaolo, D.J., 1981, Neodymiun isotopes in the Colorado Front Range and crust-mantle evolution in the Proterozoic: Nature, v. 291, p. 193-196.

DePaolo, D.J., Perry, F.V., and Baldridge, W.S., 1992, Crustal versus mantle sources of granitic magmas: a two-parameter model based on Nd isotopic studies: Transactions of the Edinburgh Royal Society of Earth Science: v. 83, p. 439-446.

DePaolo, D.J., and Wasserburg, G.J., 1976, Inferences about magma sources and mantle structure from variations of $^{143}Nd/^{144}Nd$: Geophysical Research Letters, v. 3, p. 3,743-3,746.

Doell, R.R., Dalrymple, G.B., Smith, R.L., and Bailey, R.A., 1968, Paleomagnetism, potassium-argon ages, and geology of the rhyolites and associated rocks of the Valles caldera: Memoirs of the Geological Society of America, v. 116, p. 211-248.

Duffied, W.A., and duBray, E.A., 1990, Temperature, size, and depth of the magma reservoir of the Taylor Creek Rhyolite, New Mexico: American Mineralogist, v. 75, p. 1,059-1,070.

Duffield, W.A., and Dalrymple, G.B., 1990, The Taylor Creek Rhyolite of New Mexico: a rapidly emplaced field of lava domes and flows: Bulletin of Volcanology, v. 52, p. 475-487.

Duffield, W.A., and Ruiz, J., 1992. Compositional gradients in large reservoirs of silicic magma as evidenced by ignimbrites versus Taylor Creek Rhyolite lava domes: Contributions to Mineralogy and Petrology, v. 110, p. 192-210.

Dunbar, N.W., and Hervig, R.L., 1992. Volatile and trace element composition of melt inclusions from the lower Bandelier Tuff: implications for magma chamber processes and eruptive style: Journal of Geophysical Research, v. 97, p. 15,151-15,170.

Dungan, M.A., Lindstrom, M.M., McMillan, N.J., Moorbath, S., Hoefs, J., and Haskin, L.A., 1986, Open system magmatic evolution of the Taos Plateau volcanic field, northern New Mexico; 1, The petrology and geochemistry of the Servilleta Basalt: Journal of Geophysical Research, v. 91, p. 5,666-6,028.

Dunker, K.E., Wolff, J.A., Harmon, R.S., Leat, P.T., Dickin, A.P., and Thompson, R.N., 1991, Diverse mantle and crustal components in the lavas of the NW Cerros del Rio volcanic fields, Rio Grande rift, New Mexico: Contributions to Mineralogy and Petrology, v. 108, p. 331-345.

Eichelberger, J.C., Carrigan, C.R., Westrich, H.R., and Price, R.H., 1986, Non-explosive silicic volcanism: Nature, v. 323, p. 598-602.

Ellisor, R., 1995, Petrogenesis of the lavas and tuffs of the Keres Group, Jemez Mountains Volcanic Field, New Mexico [M.S. thesis]: University of Texas, Arlington, 130 p.

Ewart, A., 1971, A review of the mineralogy and chemistry of Tertiary-recent dacitic, latitic, rhyolitic, and related salic volcanic rocks, *in*, Barker, F., ed, Trondhemites, dacites, and related rocks: New York, Elsevier, p. 13-121.

Farmer, G.L., and DePaolo, D.J., 1983, Origin of Mesozoic and Tertiary granite in the western United states and implications for pre-Mesozoic crustal structure, 1, Nd and Sr isotopic studies in the geocline of the northern Great Basin: Journal of Geophysical Research, v. 88, p. 3,379-3,401.

Gardner, J.N., 1985, Tectonic and petrologic evolution of the Keres Group: Implications for the development of the Jemez volcanic field, New Mexico [Ph.D. dissertation]: University of California, Davis, 292 p.

Gardner, J.N., and Goff, F., 1984, Potassium-argon dates from the Jemez volcanic field: Implications for tectonic activity in the north-central Rio Grande rift: New Mexico Geological Society, Guidebook 35, p. 75-81.

Gardner, J.N., Goff, F., Garcia, S., and Hagan, R., 1986, Stratigraphic relations and lithologic variations in the Jemez volcanic field, New Mexico: Journal of Geophysical Research, v. 91, p. 1763-1778.

Gay, K.R., and Smith, G.A., 1993, Eruptive history for two eruptive vents as recorded in the Peralta Tuff: Jemez Mountain, New Mexico: New Mexico Geology, v. 15, p. 75.

Goff, F., and 8 others, 1989, Excursions 17B: volcanic and hydrothermal evolution of the Valles caldera and Jemez volcanic field: New Mexico Bureau of Mines and Mineral Resources Memoir, v. 46, p. 381-434.

Golombek, M.P., 1981, Structural analysis of the Pajarito fault zone in the Española Basin of the Rio Grande rift, New Mexico [Ph.D. dissertation]: University of Massachusetts, Amherst, 129 p.

Golombek, M.P., 1983, Geology, structure, and tectonics of the Pajarito fault zone in the Española Basin of the Rio Grande rift, New Mexico: Geological Society of America Bulletin, v. 94, p. 192-205.

Golombek, M.P., McGill, G.E., and Brown, L., 1983, Tectonic and geologic evolution of the Española Basin, Rio Grande rift; structure, rate of extension, and relation to the state of stress in the Western U.S.: Tectonophysics, v. 94, p. 483-507.

Griggs, R.L., 1964, Geology and groundwater resources of the Los Alamos area, New Mexico: U.S. Geologic Survey Water Supply Paper 1753, 107 p.

Guilbeau, K.P., and Kudo, A.M., 1985, Petrology and geochemistry of the Paliza Canyon Formation and the Bearhead Rhyolite, Keres Group, Jemez Mountains, New Mexico: Geological Society of America Bulletin, v. 96, p. 108-113.

Heikoop, C.E., Dickin, A.P, Wolff, J.A., and Romanak, K.E., in prep., Pb isotope characterization of magma sources for the Cerros del Rio mafic volcanic field, Rio Grande rift, New Mexico.

Higuchi, H., and Nagasawa, H., 1969, Partition of trace elements between rock-forming minerals and their host volcanic rocks: Earth and Planetary Science Letters, v. 7, 281-287 p.

Izett, G.A., and Obradovich, J.D., 1994, $^{40}Ar/^{39}Ar$ age constraints for the Jaramillo Normal Subchron and the Matayuma-Brunhes geomagnetic boundary: Journal of Geophysical Research, v. 99, p. 2925-2934.

Jacobs, J.W., Korotev, R.L., Blanchard, D.P., and Haskins, L.A., 1977, A well tested procedure for instrumental neutron activation analysis of silicate rocks and minerals: Journal of Radioanalytical Chemistry, v. 40, p. 93-114.

Jezek, P.A., and Noble, D.C., 1978, Natural hydration and ion exchange of obsidian: An electron microprobe study: American Mineralogist, v. 63, p. 266-273.

Kempton, P.D., Harmon, R.S., Hawkesworth, C.J., and Moorbath, S., 1990, Petrology, petrography, and geochemistry of the lower crustal granulites from the Geronimo volcanic field, southeastern Arizona: Geochimica et Cosmochimica Acta, v. 54, p. 3,401-3,426.

Kochnar, N, 1977, Post-emplacement alkai modifications in rapidly cooled acid volcanic rocks: American Mineralogist, v. 62, p. 333-335.

Laughlin, A.W., Brookins, D.G., and Damon, P.E., 1976, Late-Cenozoic volcanism along the Jemez Zone of New Mexico and Arizona: Geological Society of America Abstracts with Programs, v. 8, 598 p.

Lavine, A., Smith, G.A., Goff, F., and McIntosh, W.C., 1996, Volcaniclastic rocks of the Keres Group: insights into mid-Miocene volcanism and sedimentation in the southeastern Jemez Mountains: New Mexico Geological Society, Guidebook 47, p. 211-218.

Le Bas, M.J., Le Maitre, R.W, Streckeisen, A., and Zanettin, B.A., 1986, Chemical classification of volcanic rocks based on the total alkali-silica diagram: Journal of Petrology, v. 27, 745-750 p.

Leudke, R.G., and Smith, R.L., 1978, Map showing distribution, composition, and age of late Cenozoic volcanic centers in Arizona and New Mexico: U.S. Geological Survey, Miscellaneous Investigations Map I-1091-A.

Lindstrom, D.J. and Korotev, R.L., 1982, TEABAGS: computer programs for instrumental neutron activation analysis: Journal of Radioanalytical Chemistry, v. 70, p. 439-458.

Lipman, P.W., 1965, Chemical comparison of glassy and crystalline rocks: U.S. Geological Survey Bulletin, 1201-D, p. 1-24.

Loeffler, B.M., Vainman, D.T., Baldridge, W.S., and Shafiquillah, M., 1988, Neogene rhyolites of the northern Jemez volcanic field, New Mexico: Journal of Geophysical Research, v. 93, p. 93,6157-93,6167.

Mahood, G., and Holdreth, W., 1983, Large partition coefficients for trace elements in high-silica rhyolites: Geochimica et Cosmochimica Acta, v. 47, 11-30 p.

Manley, K., 1976, The Late Cenozoic history of the Española Basin, New Mexico [Ph.D. dissertation]: University of Colorado, 171 p.

Manley, K., 1979, Stratigraphy and structure of the Española Basin, Rio Grande rift, New Mexico, *in* Riecker, R.E., ed, Rio Grande Rift: Tectonics and Magmatism: American Geophysical Union Special Publication, p. 71-86.

Mayo, E.B., 1958. Lineament tectonics and some ore districts of the southwest: Mining Engineering, v. 10, 1,169-1,175 p.

McIntosh, W.C., and Quade, J., 1995, $^{40}Ar/^{39}Ar$ geochronology of tephra layers in the Santa Fe Group, Española Basin, New Mexico: New Mexico Geological Society, Guidebook 46, p. 279-287.

Menzies, M.A., and Kyle, P.R., 1990, Continental volcanism: A crust-mantle probe, *in*, Menzies, M.A., ed., Continental Mantle: Oxford University Press, New York, p. 157-177.

Menzies, M.A., Kyle, P.R., Jones, M., and Ingram, G., 1991, Enriched and depleted source components for tholeiitic and alkaline lavas from Zuni-Bandera, New Mexico; inferences about intraplate processes and stratified lithosphere: Journal of Geophysical Research, v. 96, p. 13,645-13,671.

Michael, P.J., 1983, Chemical differentiation of the Bishop Tuff and other high-silica magmas through crystallization processes: Geology, v. 11, 31-34 p.

Nagasawa, H., and Schnetzler, C.C., 1971, Partitioning of rare earth, alkali and alkaline earth elements between phenocrysts and acidic igneous magma: Geochimica et Cosmochimica Acta, v. 35, 953-968 p.

Nakamura, N., 1974, Determination of REE, Ba, Fe, Mg, Na, and K in carbonaceous and ordinary chondrites: Geochimica et Cosmochimica Acts, v. 38, p. 757-775 p.

Nash, W.P., and Crecraft, H.R., 1981, Evolution of silicic magmas in the upper crust: An experimental analog: EOS, v. 62, p. 1,075.

Nash, W.P., and Crecraft, H.R., 1985, Partition coefficients for trace elements in silicic magmas: Geochimica et Cosmochimica Acta, v. 49, 2,309-2,322.

Nelson, B.M., and DePaolo, D.J., 1985, Rapid production of continental crust 1.7 to 1.9 b.y. ago: Nd isotopic evidence from the basement of the North american mid-continent: Geological Society of America Bulletin, v. 96, p. 746-754.

Norrish, K. and Hutton, J.T., 1969, An accurate X-ray spectrographic method for the analysis of a wide range of geological samples: Geochimica et Cosmochimica Acta, v. 33, p. 431-453.

Norrish, K. and Chappell, B.W., 1977, X-ray flourescence spectrometry, *in*, Zussman, J., ed., Physical methods in determinative mineralogy: New York, Academic Press, p. 201-272.

Olsen, K.H., Baldridge, W.S., and Callender, J.F., 1987, Rio Grande Rift; and overview: Tectonophysics, v. 143, 119-139 p.

Perry, F.V., Baldridge, W.S., and DePaolo, D.J., 1987, The role of asthenophere and lithosphere in the genesis of late Cenozoic basaltic rocks from the Rio Grande rift and adjacent regions of the southwestern United States: Journal of Geophysical Research, v. 92, p. 929,193-929,213.

Perry, F.V., Baldridge, W.S., DePaolo, D.J., and Shafiquillah, M., 1990, Evolution of a magmatic system during continental extension: the Mount taylor volcanic field, New Mexico: Journal of Geophysical Research, v. 95, p. 19,327-19,348.

Reneau, S.L., Gardner, J.N., and Forman, S.L., 1996, New evidence for the age of the youngest eruptions in the Valles caldera, New Mexico: Geology, v. 24, p. 7-10.

Schnetzler, C.C., and Philpotts, J.A., 1970, Partition coefficients of rare-earth elements between igneous matrix material and rock-forming mineral phenoocrysts; II: Geochimica et Cosmochimica Acta, v. 34, p. 331-340.

Shand, S.J., 1927, The eruptive rocks: Wiley, New York.

Smith, G.A., Larsen, D., Harlan, S.S., McIntosh, W.C., Erskine, D.W., and Taylor, S., 1991, A tale of two volcaniclastic aprons: Field guide to the sedimentology and physical volcanology of the Oligocene Espinaso Formation and Miocene Peralta Tuff, north-central New Mexico: New Mexico Bureau of Mines and Mineral Resources Bulletin, v. 137, p. 87-103.

Smith, G.A., and Lavine, A., 1996, What is the Cochiti Formation?: New Mexico Geological Society, Guidebook 47, p. 219-224.

Smith, G.A., and Kuhle, A.J., 1998, Pattern of faulting, volcanism and sedimentation at the junction of the Jemez Mountains and Rio Grande rift, New Mexico: Geological Society of America Abstracts with Programs, v. 30, 36 p.

Smith, R.L., Bailey, R.A., and Ross, C.S., 1961, Structural evolution of the Valles caldera, New Mexico, and its bearing on the emplacement of ring dikes: United States Geological Survey Professional Paper, Article 340, p. D145-D149.

Smith, R.L., and Bailey, R.A., 1968, Resurgent cauldrons: Geological Society of America Memoir, 116, p. 613-662.

Smith, R.L., Bailey, R.A., and Ross, C.S., 1970, Geologic map of Jemez Mountains, New Mexico: U.S. Geological Survey, Miscellaneous Investigations Map I-571, scale 1:125,000.

Spell, T.L., Kyle, P.R., Thirwall, M.F., and Campbell, A.R., 1993, Isotopic and geochemical constraints on the origin and evolution of post collapse rhyolites in the Valles caldera, New Mexico: Journal of Geophysical Research, v. 98, p. 19,723-19,739.

Spell, T.L., McDougall, I., and Doulgeris, A.P., 1996, Cerro Toledo Rhyolite, Jemez Volcanic Field, New Mexico: $^{40}Ar/^{39}Ar$ geochronology of eruptions between two caldera-forming events: Geological Society of America Bulletin, v. 108, p. 1549-1566.

Steven, T.A., Mehnert, H.H., and Obradovich, J.D., 1967, Age of volcanic activity in the San Juan Mountains, Colorado: United States Geological Survey Professional Paper, p. D47-D55.

Stix, J.S., Goff, F., Gorton, M.P., Heiken, G., and Garcia, S., 1988, Restoration of compositional zonation in the Bandelier silicic magma chamber between two caldera-forming eruptions; geochemistry and origin of the Cerro Toledo Rhyolite, Jemez Mountains, New Mexico: Journal of Geophysical Research, v. 93, p. 6129-6147.

Stix, J. and Gorton, M.P., 1990, Variations in trace element partition coefficients in sanidine in the Cerro Toledo Rhyolite, Jemez Mountains, New Mexico; effects of composition, temperature, and volatiles: Geochimica et Cosmochimica Acta, v. 54, 2,697-2,708.

Suppe, J., Powell, C., and Berry, R., 1975, Regional topography, seismicity, Quaternary volcanism, and the present-day tectonics of the western United States: American Journal of Science, v. 275, 397-436 p.

Turbeville, B.N., Waresback, D.B., and Self, S., 1989, Lava dome growth and explosive volcanism in the Jemez Mountains, New Mexico: evidence from the Plio-Pleistocene Puye alluvial fan: Journal of Volcanology and Geothermal Research, v. 36, p. 267-291.

Webster, J.D., and Duffield, W.A., 1991, Volatiles and lithophile elements in Taylor Creek Rhyolite: constraints from glass inclusion analysis: American Mineralogist, v. 76, p. 1,628-1,645.

WoldeGabriel, G., and Goff, F., 1989, Temporal relations of volcanism and hydrothermal systems in two areas of the Jemez volcanic field, New Mexico: Geology, v. 17, p. 986-989.

Wolff, J.A., 1985, The effect of explosive eruption processes on geochemical paterns within pyroclastic deposits: Journal of Volcanology and Geothermal Research, v. 26, p. 189-201.

Young, H.D., 1962, Statistical treatment of experimental data: New York, McGraw Hill, 172p.

Zielinski, R.A., Lipman, R.A., and Millard, H.T., Jr., 1977, Minor-element abundances in obsidian, perlite, and felsite of calc-alkaline rhyolites: American Mineralogist, v. 62, p. 426-437.

Appendix A: Bearhead Rhyolite Sample Locations

Sample	Quadrangle	Latitude	Longitude	Sample Location	Sample Description	Analytical Technique
SH 1	Redondo Peak	35°47'23"	106°32'07"	Spring Hill	flow banded rhyolite	XRF; INAA
SH 2	Redondo Peak	35°47'23"	106°32'07"	Spring Hill	flow banded rhyolite	XRF; INAA
9202P 1	Redondo Peak	35°47'00"	106°34'08"	E of Cerro Pelado	flow banded rhyolite	XRF; INAA
9202P 2	Redondo Peak	35°47'00"	106°34'08"	E of Cerro Pelado	flow banded rhyolite	XRF; INAA
9202P 3	Redondo Peak	35°47'00"	106°34'08"	E of Cerro Pelado	flow banded rhyolite	$^{40}Ar/^{39}Ar$
PN 1	Bland	35°49'30"	106°28'50"	Paseo del Norte	rhyolite	XRF; INAA
PN 2	Bland	35°49'30"	106°28'49"	Paseo del Norte	rhyolite	$^{40}Ar/^{39}Ar$
SEAP	Bland	35°45'08"	106°29'40"	SE Aspen Peak	flow banded rhyolite	XRF; INAA; $^{40}Ar/^{39}Ar$
NAP	Bland	35°45'37"	106°29'50"	N Aspen Peak	vitrophyre	XRF; INAA; $^{40}Ar/^{39}Ar$
WR	Bland	35°46'30"	106°30'00"	Woodard Ridge	flow banded rhyolite	XRF; INAA; $^{40}Ar/^{39}Ar$
SM	Bland	35°45'46"	106°23'25"	San Miguel Mountain	rhyolite	XRF; INAA; $^{40}Ar/^{39}Ar$
NCC	Canada	35°44'23"	106°25'05"	N Colle Canyon	flow banded rhyolite	XRF; INAA; $^{40}Ar/^{39}Ar$
NBC	Canada	35°44'04"	106°26'35"	N Bland Canyon	flow banded rhyolite	XRF; INAA; $^{40}Ar/^{39}Ar$
CB	Canada	35°44'05"	106°24'30"	W of Cerro Belitas	flow banded rhyolite	XRF; INAA; $^{40}Ar/^{39}Ar$
CP	Canada	35°44'35"	106°22'40"	Cerro Picacho	flow banded rhyolite	XRF; INAA; $^{40}Ar/^{39}Ar$
EBHP 1	Canada	35°43'35"	106°28'21"	E Bearhead Peak	vitrophyre	XRF; INAA
EBHP 2	Canada	35°43'35"	106°28'21"	E Bearhead Peak	vitrophyre	$^{40}Ar/^{39}Ar$
BHP	Canada	35°43'34"	106°28'52"	Bearhead Peak	vitrophyre	XRF; INAA; $^{40}Ar/^{39}Ar$
DB	Canada	35°43'02"	106°29'22"	SW Bearhead Peak	flow banded rhyolite	XRF; INAA; $^{40}Ar/^{39}Ar$
WBHP	Canada	35°43'12"	106°29'22"	west Bearhead Peak	vitrophyre	XRF; INAA; $^{40}Ar/^{39}Ar$
SCC	Canada	35°43'29"	106°24'48"	S Colle Canyon	rhyolite	XRF; INAA
31A	Canada	35°41'16"	106°29'15"	SW of Peralta Canyon	rhyolite	XRF; INAA; $^{40}Ar/^{39}Ar$

Appendix A: Bearhead Rhyolite Sample Locations (cont.)

Sample	Quadrangle	Latitude	Longitude	Sample Location	Sample Description	Analytical Technique
SHC	Bear Springs Peak	35°42'00"	106°33'17"	S Hondo Canyon	rhyolite	XRF; INAA; $^{40}Ar/^{39}Ar$
CJ	Bear Springs Peak	35°42'28"	106°30'56"	Cerro La Jara	vitrophyre	XRF; INAA; $^{40}Ar/^{39}Ar$
GBR	Bear Springs Peak	35°40'40"	106°32'11"	NW of Cerrito Yelo	flow banded rhyolite	XRF; INAA; $^{40}Ar/^{39}Ar$
NECY	Bear Springs Peak	35°40'58"	106°30'36"	NE Cerrito Yelo	rhyolite	XRF; INAA
CY	Bear Springs Peak	35°40'04"	106°31'17"	Cerrito Yelo	rhyolite	XRF; INAA; $^{40}Ar/^{39}Ar$
SBC	Canada	35°43'03"	106°25'42"	S Bland Canyon	vitrophyre	XRF; INAA; $^{40}Ar/^{39}Ar$
ERP 1	Bear Springs Peak	35°43'10"	106°32'00"	E of Ruiz Peak	pumiceous rhyolite	$^{40}Ar/^{39}Ar$
ERP 2	Bear Springs Peak	35°43'10"	106°32'00"	E of Ruiz Peak	vitrophyre	XRF; INAA
8843P	Bear Springs Peak	35°42'07"	106°33'36"	W Hondo Canyon	pyroclastic flow	XRF; INAA
TC 1	Bear Springs Peak	35°42'10"	106°32'16"	E dome of Tres Cerros	vitrophyre	$^{40}Ar/^{39}Ar$
TC 2	Bear Springs Peak	35°42'10"	106°32'16"	E dome of Tres Cerros	vitrophyre	XRF; INAA
NHC	Bear Springs Peak	35°42'17"	106°33'02"	N Hondo Canyon	flow banded rhyolite	XRF; INAA; $^{40}Ar/^{39}Ar$
CYF	Bear Springs Peak	35°39'56"	106°31'08"	flow south of Cerrito Yelo	rhyolite	XRF; INAA; $^{40}Ar/^{39}Ar$
SAC 1	Frijoles	35°47'06"	106°21'33"	S of Arrow Canyon	vitrophyre	XRF; INAA
SAC 2	Frijoles	35°47'09"	106°21'36"	S of Arrow Canyon	vitrophyre	$^{40}Ar/^{39}Ar$
RH 1	Frijoles	35°47'14"	106°22'27"	Rabitt Hill	rhyolite	$^{40}Ar/^{39}Ar$
RH 2	Frijoles	35°47'14"	106°22'27"	Rabitt Hill	rhyolite	XRF; INAA
RH 3	Frijoles	35°47'12"	106°22'27"	Rabitt Hill	vitrophyre	XRF; INAA
RLP	Canada	35°40'09"	106°25'44"	E of Tent Rocks	rhyolite flow	XRF; INAA
RBJ 2	Canada	35°41'38"	106°28'07"	Bear Jump, Peralta Canyon	basal vitrophyre	XRF; INAA; $^{40}Ar/^{39}Ar$
RBJ 1	Canada	35°41'38"	106°28'07"	Bear Jump, Peralta Canyon	basal vitrophyre	XRF; INAA; $^{40}Ar/^{39}Ar$
RBJ 3	Canada	35°41'39"	106°28'08"	Bear Jump, Peralta Canyon	rhyolite flow	XRF; INAA

Appendix A: Bearhead Rhyolite Sample Locations from Previous Studies (cont.)

Sample	Quadrangle	Latitude	Longitude	Sample Location	Sample Description	Analytical Technique
GF82-117*	Canada	35°44'	106°26.5'	S Bland Canyon	na	K/Ar
RLPA**	Canada	~35°40'09"	~106°25'44"	E of Tent Rocks	na	$^{40}Ar/^{39}Ar$
F82-77*	Frijoles	35°47.2'	106°22.3'	Rabitt Hill	na	K/Ar
GF82-1*	Canada	35°44'	106°24.5'	W side Cerro Boletas	na	K/Ar
SCC/BC#	Canada	na	na	S Colle or Bland Canyon	na	K/Ar
F83-19*	Canada	35°44.6'	106°22.8'	Cerro Picacho	na	K/Ar
JG80-47c*	Redondo Peak	~35°47'00"	~106°34'08"	E of Cerro Pelado	na	K/Ar

* Gardner (1985)

**McIntosh and Quade (1995)

Silberman et al. (written communication, 1976, in Leudke and Smith, 1978)

Appendix A: Peralta Tuff Sample Locations

Sample	Quadrangle	Latitude	Longitude	Sample Location	Sample Description	Analytical Technique
CF	Canada	35°39'39"	106°24'19"	E of Tent Rocks	reworked fallout tephra	XRF; INAA
CAN	Canada	35°40'45"	106°26'17"	NW of Colle/Peralta Canyon	air fall tephra	XRF; INAA
TE	Canada	35°39'50"	106°24'42"	E of Tent Rocks	pyroclastic flow	XRF; INAA
TRD	Canada	35°41'27"	106°26'18"	W of Colle Canyon	pyroclastic flow	XRF; INAA
TRC	Canada	35°41'05"	106°27'11"	Peralta Canyon/Canada Camada	pyroclastic flow	XRF; INAA
TRB	Canada	35°40'45"	106°26'50"	S side of Canada Camada	pyroclastic flow	XRF; INAA
TRA	Canada	35°41'10"	106°26'50"	S side of Canada Camada	pyroclastic flow	XRF; INAA
AF	Canada	35°41'05"	106°27'11"	Peralta Canyon/Canada Camada	air fall tephra	XRF; INAA
TG	Canada	35°41'05"	106°26'36"	SW tip of Oaks Mesa	ash flow	XRF; INAA
CC 3	Canada	35°41'05"	106°26'36"	W of Colle Canyon	air fall tephra	XRF; INAA
CC 1	Canada	35°41'05"	106°26'36"	SW tip of Oaks Mesa	air fall tephra	XRF; INAA
CC 2	Canada	35°41'05"	106°26'36"	SW tip of Oaks Mesa	pyroclastic flow	XRF; INAA
TB	Canada	35°41'05"	106°26'36"	SW tip of Oaks Mesa	pyroclastic flow	XRF; INAA
TA	Canada	35°41'24"	106°25'53"	W arm of West Mesa	pyroclastic flow	XRF; INAA
TBJ	Canada	35°41'10"	106°26'50"	WSW tip of Oaks Mesa	pyroclastic flow	XRF; INAA
TLP 2	Canada	35°39'42"	106°24'21"	W of West Mesa	terminal fall deposit	XRF; INAA
TLP 1	Canada	35°41'57"	106°25'57"	E of Tent Rocks	surge deposit	XRF; INAA
TWM 1	Canada	35°41'58"	106°25'58"	W of West Mesa	ash flow	XRF; INAA
TWM 2	Canada	35°41'57"	106°25'57"	W of West Mesa	ash flow	XRF; INAA
1 PT	Canada	35°42'04"	106°24'40"	S end of Bland Canyon	pyroclastic flow	XRF; INAA
2 PT	Canada	35°41'49"	106°24'25"	S end of Bland Canyon	air fall tephra	XRF; INAA; $^{40}Ar/^{39}Ar$

Appendix A: Peralta Tuff Sample Locations from Previous Studies (cont.)

Sample	Quadrangle	Latitude	Longitude	Sample Location	Sample Description	Analytical Technique
CANA**	Canada			NW of Colle/Peralta Canyon	na	$^{40}Ar/^{39}Ar$
CANB**	Canada			NW of Colle/Peralta Canyon	na	$^{40}Ar/^{39}Ar$
TEA#	Canada			E of Tent Rocks	na	$^{40}Ar/^{39}Ar$
CCA**	Canada			NW Colle/Peralta Canyon	na	$^{40}Ar/^{39}Ar$
TWMA**	Canada			W of West Mesa	na	$^{40}Ar/^{39}Ar$

*Gardner (1985)

** McIntosh and Quade (1995)

McIntosh (unpublished from G.A. Smith, personal communication)

Appendix B: Petrographic Descriptions of Rhyolite

General Petrographic Description for All Rhyolte Samples:
9202P 1&2, 31A, CB, CP, CY, DB, GBR, CYF, NCC, NBC, NHC, NECY, PN, RBJ3, RH2, RLP, SEAP, SH, SHC, SM, WR, ERP2

Sanidine: 0 to 5.6%, mean 2.4%
phenocrysts & phenocryst fragments: 0.025-5.00 mm; clear; equant & elongate; rounding common; unresorbed; unembayed (rarely highly embayed); untwinned & carlsbad twins (common); baveno twins (common); oscillatory zoning along rim (common); continuous & discontinuous zoning throughout crystal (less common); unfractured (fairly commonly fractured).
glomerocrysts: 0.37-5.00 mm; sanidine/plagioclase/quartz/biotite; rounded; resorbed; intercrystalline contacts slightly to highly resorbed. unembayed (commonly highly embayed).

Plagioclase: 0 to 12.4%, mean 2.3%
phenocrysts & phenocryst fragments: 0.01-2.50 mm; clear; lath-shaped; euhedral (fairly commonly rounded); unresorbed; unembayed (fairly uncommonly embayed); polysynthetic and carlsbad twins; discontinuous, continuous & oscillatory zoning (very common); sanidine overgrowths (fairly uncommon); plagioclase overgrowths only seen in CP, CYF); unfractured (uncommonly fractured).

Quartz: 0 to 14.2%, mean 2.3%
phenocrysts & phenocryst fragments: 0.37-3.25 mm; clear; equant; rounded (commonly euhedral); unresorbed; embayed (commonly); fractured (fairly commonly).

Biotite: 0 to 3.0%, mean 0.4%
phenocrysts & phenocryst fragments: 0.13-1.75 mm; lt. to dark red brown; rare green; tabular; unrounded (rarely rounded); rare sanidine overgrowths a few bent around phenocrysts; fairly commonly altered.

Magnetite: 0 to 0.9%, mean 0.2%
minor growths on glomerocrysts and in matrix (fairly common).

Matrix: 73.2 to 99.5%, mean 92.3%
glassy; aphanitic; discontinuous flow banding; devitrification (mean 84.7 %); feldspar (mean 0.6%); lithics (mean 0.1%).

Appendix B: Detailed Petrographic Descriptions of Rhyolite Samples Containing Important Phases or Textures (listed by sample)

Samples: CB, CP, CY, GBR, CYF

Allanite: < 0.25 mm; lt. brown, equant, unrounded, unresorbed, unembayed, associated with sanidine in glomerocrysts and matrix.

Samples: DB, GBR, ERP2, CYF, EBHP, NCC, NBC, NECY, PN, RBJ3, RH2, RLP, SEAP, SH, SHC, SM, WR

Zircon: 0.025-0.37 mm; clear; equant to elongate; rounded (fairly commonly); unresorbed; unembayed; associated with feldspars in glomerocrysts; particularly associated with biotite and opaques in matrix and glomerocrysts.

Samples: NBC

Apatite: 0.13-0.75 mm; acicular; associated with biotite.

Samples: CB, NECY, SHC, RLP

Matrix: 0.02-0.25 mm; non-glassy; feldspar enriched compared to all other samples.

Samples: NECY, WR

Biotite: Visually, abundances appear to be greater than in other samples.

Samples: CJ, CYF, CY, EBHP, PN, SHC

Phenocryst concentrations enriched in these samples, especially plagioclase (except PN).

Samples: 31A, ERP2

Pumiceous: pumice fragments--1.00 mm to 1.00 cm; med. gray; rounded. pumiceous banding--0.05 mm; contains round vescicles.

Samples: DB

Lithics: 0.13-3.25 mm; lt. brown; rounded; spherulitic matrix; phenocryst fragments of plagioclase (polysynthetic and carlsbad twins, zoned); altered biotite; recrystallized quartz and sanidine (carlsbad twins).

Samples: 31A, CB, CP, CY, DB, ERP2, GBR, CYF, EBHP, NBC, RBJ3, RH2

Display some slightly to highly embayed sanidine crystals.

Appendix B: Petrographic Descriptions of Vitrophyre

General Petrographic Description for All Vitrophyre Samples:
BHP, CJ, EBHP, NAP, RBJ1, RH3, SAC, SBC, TC2, WBHP

Sanidine: 0.3 to 3.5%, mean 1.9%

phenocrysts & phenocryst fragments: 0.05-2.50 mm; clear: equant & elongate; rounding common; unresorbed; unembayed (rarely highly embayed); untwinned, baveno and carlsbad twins (v. common); continuous and oscillatory zoning around the rim (common); unfractured (fairly commonly fractured).
glomerocrysts: 0.125-3.25 mm: sanidine/palgioclase/quartz/biotite: rounded; resorbed; intercrystalline contacts resorbed (fairly commonly unresorbed), unembayed (fairly commonly embayed); unfractured (commonly fractured).

Plagioclase: 0.8 to 3.4%, mean 1.5%

phenocrysts & phenocryst fragments: 0.05-3.00 mm; clear; lath-shaped; euhedral (fairly commonly rounded); unresorbed; unembayed; polysynthetic and carlsbad twins (v. common); continuous, discontinuous, oscillatory zoning (v. common), plagioclase and sanidine overgrowths (seen in CJ); unfractured (uncommonly fractured).

Quartz: 0.9 to 4.6%, mean 2.4%

phenocrysts & phenocryst fragments: 0.075-2.50 mm; clear; equant: rounded (commonly euhedral): unresorbed; embayed (commonly); unfractured (commonly fractured).

Biotite: 0 to 1.3%, mean 0.2%

phenocrysts & phenocryst fragments: 0.025-2.50 mm; med. to dk.-red brown and green; tabular & acicular; unrounded (rarely rounded); rare sanidine overgrowths; a few bent around phenocrysts; fairly commonly altered.

Magnetite: trace

0.25 mm; minor growths on glomerocrysts and in matrix (fairly common)

Matrix: 90.4 to 97.9%, mean 93.8%

perlitic and unperlitic, spherulitic glass with minor amounts of fracture-fill quartz; minor flow banding marked by ~0.125 mm feldspar fragments (0.1%); aphanitic; devitrification (mean 20.0%); lithics (mean 0.1%).

Appendix B: Detailed Petrographic Descriptions of Vitrophyre Samples Containing Important Phases or Textures (listed by sample)

Samples: BHP, CJ, EBHP

Allanite: < 0.01 mm; associated with sanidine glomerocrysts; med. brown; equant; unresorbed.

Samples: EBHP, NAP, RBJ1, RH3, SAC, SBC, TC2

Zircon: 0.025-0.05 mm; clear, equant & elongate, rounded (fairly common); unresorbed; unembayed; associated with feldspars, quartz, biotite (v. commonly) and magnetite (v. common) in matrix and glomerocrysts.

Samples: EBHP, NAP

Apatite: 0.5 mm, acicular; associated with biotite.

Samples: SAC, TC2

Lithics: Fragment A: feldspar-rich matrix, recrystallized, spherulitic, abundant polysynthetic twinned plagioclase laths, oscillatory and discontinuous zoning, abundant magnetite.

Fragment B: acicular plagioclase matrix with biotite, acicular apatite, continuously zoned plagioclase, magnetite, fine-grained recrystallized quartz, and highly resorbed carlsbad twinned sanidine.

Fragment C: fine recrystallized quartz matrix with abundant coarser-grained plagioclase laths.

Samples: BHP, CJ, EBHP, NAP, SAC.

Display some slightly to highly embayed sanidine crystals.

Appendix B: Petrographic Descriptions of Tuff

General Petrographic Description for All Tuff Samples:
1 PT, CAN, CC2, CC3, TA, TB, TG, TRB, TRC, TE, TRD, TWM2

Sanidine: 0 to 1.0%, mean 0.4%
phenocrysts & phenocryst fragments: 0.07-3.25 mm; clear; elongate; rounding common; unresorbed; unembayed (rarely embayed); baveno and carlsbad twins (untwinned fairly common); discontinuous near crystal rim and continuous zoning (fairly common); sanidine overgrowths; unfractured fairly commonly fractured).
glomerocrysts: 0.05-3.25 mm; sanidine/plagioclase/quartz/biotite; rounded; resorbed; intercrystalline contacts resorbed; unembayed (rarely embayed)

Plagioclase: 0 to 1.0%, mean 0.4%
phenocrysts & phenocryst fragments: 0.25-2.75 mm; clear; lath-shaped; euhedral (fairly commonly rounded); unresorbed; unembayed (rarely embayed); polysynthetic and carlsbad twins; discontinuous zoning around crystal rim, continuous and oscillatory zoning; sanidine overgrowths; unfractured (uncommonly fractured).

Quartz: 0 to 2.1%, mean 0.5%
phenocrysts & phenocryst fragments: 0.50-3.00 mm; clear; equant; rounded (commonly euhedral); unresorbed; unembayed (v. common); fractured

Biotite: 0 to 0.2%, mean < 0.1%
phenocrysts & phenocryst fragments: 0.125-1.00 mm; lt to med brown; equant and tabular; rounded; biotite & plagioclase overgrowth (only seen in TA); a few bent around phenocrysts; unfractured (rarely fractured).

Magnetite: 0 to 0.2%, mean < 0.1%
0.075 mm; minor growths on biotite, glomerocrysts and in matrix.

Matrix: 97.2 to 99.8%, mean 98.6%
glassy; pumiceous; aphanitic; round to elongate vescicles 0.025-0.37 mm; devitification (mean 16.14%); secondary fibrous quartz fill in vescicles (rare)

Appendix B: Detailed Petrographic Descriptions of Tuff Samples Containing Important Phases or Textures (listed by sample)

Samples: CAN, CC3

Allanite: < 0.01 mm; lt brown; tabular; unrounded; unresorbed; unembayed; associated with matrix, sanidine phenocrysts and sanidine in glomerocrysts.

Samples: 1 PT, TA, TB, TG, TRB, TRC, TE, TRD, TWM2

Zircon: 0.075-0.125 mm; clear; equant & elongate; rounded (fairly commonly); single crystals and clusters; associated with sanidine, plagioclase, biotite, and magnetite in matrix and glomerocrysts.

Samples: 1 PT, TWM2

Apatite: 0.075 mm; acicular; associated with biotite.

Samples: CAN, TRB

Display some embayed sanidine crystals.

Appendix C: Bearhead Rhyolite Whole Rock Major and Trace Element Abundances

wt. %	SH 1	SH 2	9202P	PN	SEAP	NAP	WR	SM	NCC
SiO_2	77.0	77.4	78.1	75.6	76.1	73.7	77.2	77.1	76.4
Al_2O_3	12.7	12.4	13.4	12.5	13.4	13.1	12.1	13.1	13.1
TiO_2	0.1	0.1	0.1	0.1	0.2	0.2	0.1	0.1	0.1
Fe_2O_3[#]	0.7	0.7	0.6	1.3	0.9	0.8	0.8	0.6	0.6
MgO	< 0.1	< 0.1	< 0.1	< 0.1	< 0.1	< 0.1	< 0.1	< 0.1	< 0.1
CaO	0.5	0.5	0.4	< 0.3	0.4	0.8	0.4	0.4	0.4
Na_2O	3.8	3.5	3.8	4.0	2.8	3.5	2.7	3.7	3.9
K_2O	3.9	4.1	4.1	4.4	4.3	3.7	4.1	4.1	4.1
MnO	0.067	0.068	0.051	0.045	0.069	0.074	0.048	0.052	0.067
P_2O_5	< 0.04	< 0.04	< 0.04	< 0.04	0.04	0.04	< 0.04	< 0.04	0.04
% LOI	0.66	0.87	0.51	1.07	2.13	4.85	1.82	0.62	0.45
Total	99.5	99.7	101.0	98.9	100.2	100.6	99.3	99.9	99.2

[#] Total Fe expressed as Fe_2O_3.

ppm	SH 1	SH 2	9202P	PN	SEAP	NAP	WR	SM	NCC
Rb*	103	87	130	118	128	136	120	134	126
Sr*	85	84	38	18	96	124	57	38	32
Y*	17	16	19	28	14	18	17	17	24
Zr*	106	104	84	181	91	89	82	87	94
Nb*	22	20	20	38	19	24	20	20	27
Ba**	1275	1379	747	< 150	875	827	685	662	697
Sc**	2.3	2.2	3.0	1.4	3.2	3.2	3.1	3.1	3.3
Zn**	28	23	24	34	26	27	25	30	24
Cs**	2.2	0.8	3.6	1.9	1.8	4.6	3.0	3.2	3.5
La**	43	41	28	49	23	23	22	27	30
Ce**	75	71	56	98	44	43	43	49	58
Nd**	23	19	< 22	42	5	< 21	12	17	19
Sm**	4.2	4.1	3.9	5.8	3.5	3.5	3.3	3.3	4.4
Eu**	0.8	0.7	0.5	0.1	0.5	0.5	0.4	0.5	0.6
Tb**	0.6	0.6	0.6	0.9	0.6	0.6	0.5	0.6	0.6
Yb**	2.4	2.2	2.1	3.4	2.7	2.4	2.5	2.5	2.9
Lu**	0.3	0.3	0.4	0.4	0.3	0.3	0.3	0.4	0.4
Hf**	3.9	3.8	3.9	7.5	3.6	3.7	3.5	3.7	4.1
Ta**	3.1	2.5	2.6	5.1	3.3	2.9	2.9	2.6	3.0
Th**	11.5	10.9	12.9	15.7	10.4	10.2	10.0	12.9	12.2
U**	3.6	3.6	3.4	5.6	4.0	5.0	4.2	4.6	4.0

*XRF, ** INAA

Appendix C: Bearhead Rhyolite Whole Rock Major and Trace Element Abundances (cont.)

wt.%	NBC	CB	CP	EBHP	BHP	DB	WBHP	SCC	31A
SiO_2	77.5	77.9	77.5	74.9	74.9	78.4	75.4	68.7	77.5
Al_2O_3	12.7	13.0	12.2	12.5	12.6	11.5	12.5	11.5	13.0
TiO_2	0.1	0.1	0.1	0.1	0.1	0.1	0.1	0.1	0.1
Fe_2O_3[#]	0.5	0.6	0.6	0.5	0.5	0.5	0.5	0.5	0.6
MgO	< 0.1	< 0.1	< 0.1	< 0.1	< 0.1	< 0.1	< 0.1	0.5	< 0.1
CaO	0.4	0.4	< 0.3	0.4	0.5	0.4	0.4	< 0.3	0.4
Na_2O	3.7	3.7	3.9	3.3	3.6	3.0	3.4	0.9	3.7
K_2O	4.2	4.1	4.6	4.5	3.8	4.3	4.3	2.2	4.0
MnO	0.068	0.051	0.045	0.069	0.074	0.048	0.052	0.052	0.057
P_2O_5	< 0.04	< 0.04	< 0.04	< 0.04	< 0.04	< 0.04	< 0.04	< 0.04	< 0.04
% LOI	0.43	0.57	0.28	4.04	4.36	0.67	3.58	13.91	0.41
Total	99.6	100.5	99.3	100.3	100.6	98.9	100.2	98.3	99.8

[#] Total Fe expressed as Fe_2O_3.

ppm	NBC	CB	CP	EBHP	BHP	DB	WBHP	SCC	31A
Rb*	136	139	140	163	132	138	148	117	130
Sr*	31	34	38	30	50	26	37	368	26
Y*	19	23	20	28	24	10	19	21	16
Zr*	78	83	81	81	78	75	78	98	97
Nb*	19	22	19	24	21	15	24	16	14
Ba**	557	543	615	392	677	410	617	548	447
Sc**	2.9	3.1	3.0	3.2	3.0	2.8	3.0	2.7	3.0
Zn**	37	33	26	28	27	12	22	22	20
Cs**	3.3	4.0	4.0	4.7	7.6	0.2	0.2	0.2	0.2
La**	25	26	28	25	25	22	26	26	32
Ce**	48	49	53	49	50	45	50	48	59
Nd**	11	< 20	20	18	13	20	16	11	12
Sm**	3.4	3.3	3.7	4.4	3.8	3.5	4.1	4.0	4.7
Eu**	0.4	0.4	0.4	0.5	0.5	0.4	0.5	0.5	0.6
Tb**	0.6	0.6	0.7	0.8	0.6	0.6	0.7	0.7	0.7
Yb**	2.5	2.2	2.7	3.2	2.6	2.2	2.4	2.8	2.8
Lu**	0.3	0.3	0.3	0.4	0.3	0.3	0.3	0.3	0.3
Hf**	3.7	3.9	3.8	3.9	3.6	3.3	3.5	3.3	4.2
Ta**	3.4	3.4	3.2	3.1	2.7	2.5	2.3	1.6	2.6
Th**	13.0	13.4	13.2	11.5	11.6	10.5	11.8	10.3	12.8
U**	5.8	4.1	5.2	4.7	4.4	3.9	5.3	3.5	4.8

*XRF, ** INAA

Appendix C: Bearhead Rhyolite Whole Rock Major and Trace Element Abundances (cont.)

wt.%	8843P	SHC	CJ	GBR	NECY	RH 3	CY	SBC	ERP 2
SiO_2	74.0	68.1	75.0	73.1	66.9	75.6	77.3	75.5	75.3
Al_2O_3	12.9	17.0	12.6	14.8	17.9	13.0	12.6	12.7	12.8
TiO_2	0.1	0.6	0.1	0.2	0.5	0.1	0.1	0.1	0.1
Fe_2O_3[#]	0.6	2.9	0.5	1.1	2.6	0.7	0.6	0.5	0.5
MgO	< 0.1	0.3	< 0.1	0.2	0.3	< 0.1	< 0.1	< 0.1	< 0.1
CaO	0.4	< 0.3	0.4	0.9	1.2	0.4	0.5	0.4	0.4
Na_2O	3.1	5.5	3.7	3.6	4.4	3.5	3.5	3.7	3.7
K_2O	4.4	3.9	4.1	3.6	4.8	4.1	4.1	4.3	4.0
MnO	0.064	0.094	0.065	0.046	0.036	0.064	0.055	0.066	0.066
P_2O_5	< 0.04	0.19	< 0.04	0.07	0.14	< 0.04	< 0.04	< 0.04	< 0.04
% LOI	4.70	0.43	3.61	2.72	1.84	2.55	0.70	3.02	3.21
Total	100.3	99.0	100.1	100.4	100.6	100.1	99.4	100.3	100.2

[#] Total Fe expressed as Fe_2O_3.

ppm	8843P	SHC	CJ	GBR	NECY	RH 3	CY	SBC	ERP 2
Rb*	137	87	139	103	124	128	163	125	143
Sr*	32	356	36	264	387	55	40	31	27
Y*	17	48	24	16	33	25	0	24	15
Zr*	80	459	78	170	417	86	77	76	75
Nb*	16	58	21	28	30	23	16	21	15
Ba**	526	1408	688	1081	1723	557	241	518	518
Sc**	3.2	5.5	2.8	1.7	4.7	3.0	1.7	3.2	3.0
Zn**	38	61	29	26	42	22	7.8	18.3	25.1
Cs**	0.2	0.2	0.2	0.1	0.1	0.2	0.2	0.2	0.2
La**	27	83	27	54	77	30	36	24	25
Ce**	50	128	54	75	122	55	61	48	49
Nd**	28	35	12	24	42	10	< 16	24	21
Sm**	3.9	8.0	3.9	4.1	7.3	3.8	1.9	4.0	3.7
Eu**	0.5	1.9	0.5	0.8	1.5	0.5	0.3	0.4	0.4
Tb**	0.7	1.1	0.6	0.5	0.8	0.6	0.3	0.7	0.6
Yb**	2.5	3.5	2.3	2.2	3.2	2.6	1.7	2.6	2.7
Lu**	0.3	0.5	0.3	0.3	0.4	0.4	0.2	0.4	0.4
Hf**	3.3	10.4	3.5	4.7	9.7	3.5	3.3	3.6	3.5
Ta**	2.6	3.8	2.5	2.9	2.8	2.3	3.0	2.2	2.2
Th**	11.7	17.2	11.9	16.4	17.1	12.5	20.0	11.6	12.4
U**	4.5	6.0	5.0	5.2	7.9	4.7	6.2	4.9	5.7

*XRF, ** INAA

Appendix C: Bearhead Rhyolite Whole Rock Major and Trace Element Abundances (cont.)

wt.%	TC 2	NHC	CYF	SAC	RH 2	RBJ 3	RLP 1
SiO_2	75.5	76.7	76.8	75.8	77.8	75.1	78.1
Al_2O_3	12.7	11.8	13.0	12.7	12.1	12.2	11.4
TiO_2	0.1	0.1	0.1	0.1	0.1	0.1	0.1
Fe_2O_3[#]	0.5	0.6	0.6	0.6	0.6	0.5	0.5
MgO	< 0.1	< 0.1	< 0.1	< 0.1	< 0.1	< 0.1	< 0.1
CaO	0.4	0.3	0.5	0.4	0.3	< 0.3	< 0.3
Na_2O	3.5	3.8	3.7	3.7	3.8	3.0	3.8
K_2O	4.2	4.6	4.1	4.1	4.5	5.3	4.2
MnO	0.065	0.062	0.045	0.063	0.056	0.069	0.061
P_2O_5	< 0.04	< 0.04	< 0.04	< 0.04	0.04	< 0.04	0.05
% LOI	3.18	0.61	0.85	2.66	0.33	3.43	0.74
Total	100.2	98.5	99.7	100.3	99.7	99.8	99.0

[#] Total Fe expressed as Fe_2O_3.

ppm	TC 2	NHC	CYF	SAC	RH 2	RBJ 3	RLP 1
Rb*	169	143	165	134	135	127	118
Sr*	38	31	37	42	35	8	26
Y*	24	15	2	21	21	30	26
Zr*	76	133	71	82	85	84	74
Nb*	25	17	24	24	21	40	22
Ba**	427	567	156	573	625	385	502
Sc**	3.0	2.9	1.8	3.1	2.9	3.3	3.2
Zn**	24.4	23.8	19.1	22.3	29.3	35	17
Cs**	0.4	0.2	0.2	0.3	0.2	5.2	3.9
La**	24	27	39	26	31	24	24
Ce**	49	51	52	53	53	49	49
Nd**	28	22	17	19	16	< 22	28
Sm**	3.6	3.7	1.7	3.6	3.9	4.3	4.1
Eu**	0.4	0.4	0.2	0.5	0.5	0.5	0.5
Tb**	0.7	0.6	0.3	0.6	0.6	0.7	0.6
Yb**	2.9	2.7	1.8	2.9	2.9	2.7	3.0
Lu**	0.3	0.3	0.3	0.3	0.3	0.4	0.4
Hf**	3.5	3.6	3.1	3.7	3.7	3.9	3.7
Ta**	2.4	2.6	3.6	2.3	2.9	3.3	2.9
Th**	12.2	12.6	20.2	12.5	12.5	11.8	11.5
U**	5.0	4.9	6.4	4.9	5.0	5.2	4.7

*XRF, ** INAA

Appendix C: Peralta Tuff Whole Rock Major and Trace Element Abundances

wt. %	CF	CAN	TE	TRD	TRC	TRB	TRA	AF
SiO_2	73.9	75.2	74.4	69.3	75.6	76.9	73.3	76.9
Al_2O_3	12.6	11.8	11.5	11.5	12.5	12.7	12.5	11.3
TiO_2	0.1	0.1	0.1	0.1	0.1	0.1	0.1	0.1
Fe_2O_3[#]	0.6	0.5	0.5	0.5	0.6	0.5	0.5	0.5
MgO	< 0.1	< 0.1	< 0.1	< 0.1	0.1	0.1	< 0.1	0.1
CaO	0.4	< 0.3	0.4	< 0.3	< 0.3	< 0.3	< 0.3	< 0.3
Na_2O	2.6	3.0	2.9	3.3	3.5	3.1	2.8	1.9
K_2O	5.5	5.1	4.6	4.5	4.9	4.9	5.2	5.3
MnO	0.049	0.061	0.038	0.066	0.065	0.063	0.019	0.064
P_2O_5	< 0.04	< 0.04	0.06	< 0.04	< 0.04	< 0.04	0.06	< 0.04
% LOI	4.83	4.03	3.63	4.71	3.33	5.05	5.19	5.50
Total	100.6	99.9	98.1	94.0	100.6	103.4	99.6	101.8

[#] Total Fe expressed as Fe_2O_3.

ppm	CF	CAN	TE	TRD	TRC	TRB	TRA	AF
Rb*	150	132	129	119	119	124	134	136
Sr*	46	17	28	30	33	33	37	31
Y*	6	22	15	19	24	22	18	14
Zr*	70	83	70	76	74	75	80	67
Nb*	23	34	14	22	20	20	22	17
Ba**	88	666	526	682	675	646	775	623
Sc**	1.9	2.9	2.7	2.9	2.9	2.9	2.9	2.8
Zn**	15	18	16	13	19	21	25	23
Cs**	6.5	4.9	4.5	4.2	4.4	4.2	4.4	4.6
La**	29	26	24	27	< 0.75	26	27	23
Ce**	46	49	48	51	52	51	51	48
Nd**	< 26	< 26	< 26	7	< 26	21	< 23	< 21
Sm**	1.5	3.7	3.5	4.1	4.0	3.9	3.9	3.6
Eu**	0.2	0.4	0.4	0.4	0.5	0.5	0.5	0.5
Tb**	0.2	0.6	0.5	0.5	0.5	0.6	0.6	0.5
Yb**	1.4	2.1	2.6	2.4	2.4	2.3	2.6	2.1
Lu**	0.3	0.3	0.2	0.3	0.3	0.4	0.3	0.4
Hf**	3.4	3.5	3.4	3.5	3.7	3.4	3.7	3.3
Ta**	2.7	2.3	3.3	2.7	2.8	2.0	2.5	2.5
Th**	20.9	12.2	11.9	13.3	11.9	11.6	11.8	10.7
U**	8.5	4.4	5.0	4.0	4.5	4.4	4.8	4.7

*XRF, ** INAA

Appendix C: Peralta Tuff Whole Rock Major and Trace Element Abundances (cont.)

wt. %	CC 3	CC 1	CC 2	TB	1 PT	2 PT	TA	TBJ 1
SiO_2	74.4	74.7	71.9	74.5	75.5	69.5	74.3	73.6
Al_2O_3	12.1	12.5	12.0	11.8	13.4	12.6	12.5	12.6
TiO_2	0.1	0.1	0.1	0.1	0.1	0.1	0.1	0.1
Fe_2O_3[#]	0.6	0.5	0.5	0.5	0.6	0.5	0.5	0.6
MgO	< 0.1	0.1	< 0.1	0.4	0.2	0.4	1.5	0.1
CaO	< 0.3	< 0.3	0.4	< 0.3	0.4	< 0.3	< 0.3	< 0.3
Na_2O	3.4	2.9	3.4	2.8	2.9	2.3	3.1	2.5
K_2O	4.5	5.1	4.0	5.0	5.1	5.0	5.2	5.5
MnO	0.061	0.038	0.066	0.065	0.063	0.019	0.017	0.078
P_2O_5	< 0.04	< 0.04	0.06	0.07	0.04	< 0.04	0.07	< 0.04
% LOI	5.17	5.43	4.90	4.74	4.26	8.16	4.39	5.22
Total	100.4	101.6	97.4	100.0	102.5	98.7	101.7	100.4

[#] Total Fe expressed as Fe_2O_3.

ppm	CC 3	CC 1	CC 2	TB	1 PT	2 PT	TA	TBJ 1
Rb*	118	122	120	139	108	150	120	175
Sr*	21	30	17	25	59	34	24	25
Y*	30	18	30	14	24	23	23	24
Zr*	92	77	89	82	81	74	82	74
Nb*	37	18	37	20	23	25	25	20
Ba**	637	577	564	358	669	172	472	588
Sc**	3.1	3.2	3.2	3.2	3.1	3.8	3.2	3.1
Zn**	28	26	24	20	25	33	23	11
Cs**	3.9	4.4	4.5	5.5	3.9	3.3	4.2	6.1
La**	28	27	28	< 0.77	23	16	26	27
Ce**	56	56	57	49	46	37	54	55
Nd**	< 22	27	< 20	16	12	7	16	23
Sm**	4.3	4.1	4.2	4.1	3.9	3.6	4.2	4.3
Eu**	0.5	0.5	0.6	2.6	0.5	0.4	0.5	0.5
Tb**	0.7	0.6	0.6	0.7	0.7	0.6	0.6	0.6
Yb**	2.5	2.3	2.5	2.6	2.5	3.0	2.6	2.4
Lu**	0.4	0.3	0.4	0.4	0.3	0.3	0.4	0.4
Hf**	3.9	3.9	4.0	3.6	3.8	4.0	3.9	3.7
Ta**	2.1	2.3	2.2	2.6	3.0	3.0	2.9	2.5
Th**	11.9	11.6	11.9	11.3	10.8	11.5	11.8	11.7
U**	4.6	4.4	3.4	4.5	3.8	4.1	3.7	5.7

*XRF, ** INAA

Appendix C: Peralta Tuff Whole Rock Major and Trace Element Abundances (cont.)

wt. %	TLP 2	TWM 2	TWM 1	TG
SiO_2	74.4	74.2	73.4	74.4
Al_2O_3	11.7	12.3	12.4	12.3
TiO_2	0.1	0.1	0.1	0.1
Fe_2O_3[#]	0.5	0.6	0.5	0.6
MgO	< 0.1	< 0.1	0.1	0.1
CaO	< 0.3	< 0.3	< 0.3	< 0.3
Na_2O	2.3	3.3	2.7	3.1
K_2O	5.9	5.0	5.4	4.9
MnO	0.068	0.075	0.010	0.049
P_2O_5	< 0.04	< 0.04	0.07	< 0.04
% LOI	5.08	5.12	4.51	4.65
Total	100.4	100.7	99.2	94.0

[#] Total Fe expressed as Fe_2O_3

ppm	TLP 2	TWM 2	TWM 1	TG
Rb*	123	132	134	116
Sr*	22	24	22	27
Y*	18	23	23	21
Zr*	67	78	82	78
Nb*	14	18	23	21
Ba**	390	567	314	673
Sc**	3.3	3.2	3.4	3.2
Zn**	38	40	26	26
Cs**	4.3	4.2	4.5	4.2
La**	24	24	24	28
Ce**	51	48	49	54
Nd**	12	38	16	26
Sm**	4.1	4.1	4.3	4.1
Eu**	0.5	0.5	0.5	0.5
Tb**	0.7	0.6	0.7	0.6
Yb**	3.1	2.6	2.5	2.6
Lu**	0.4	0.3	0.4	0.3
Hf**	3.9	3.7	4.0	3.8
Ta**	2.9	2.1	2.8	2.1
Th**	11.7	11.3	11.7	11.7
U**	4.5	5.0	4.7	4.0

*XRF, ** INAA

APPENDIX D

Sample Collection

Bearhead Rhyolite

Several kilograms of each sample were collected from 28 domes and 4 flows (see Appendix A for locations). Samples chosen for chemical analysis displayed discontinuous to no flow banding, no visible alteration, and as little devitrification as possible. Samples chosen for $^{40}Ar/^{39}Ar$ dating contained clear, unaltered sanidine phenocrysts. Most samples were extracted from outcrop and edges were trimmed of weathering rinds and visible alteration in the field. One sample (31A) was collected from a boulder-sized piece of float in an area with no outcrop.

Peralta Tuff

Approximately 2,000 cm^3 of each of 19 pumice samples (air fall tephra, pyroclastic flow, distal fall deposit, and surge deposit) were collected from Peralta, Colle, and Bland Canyons with guidance from Dr. G. A. Smith (University of New Mexico, Albuquerque). Pumice samples chosen for chemical analysis were typically > 2 cm diameter to minimize the effects of magma fragmentation and phenocryst control of bulk pumice chemistry due to high phenocryst/glass ratios (Wolff, 1985). Five samples contained pumice < 1 cm diameter (CF, TBJ, TLP, TLP, 2 PT). Samples 1 PT and 2 PT

lie stratigraphically lower than all of the other samples and are not included in G. A. Smith's stratigraphy of the Peralta Tuff. Additionally, sample CF lies stratigraphically above G.A. Smith's stratigraphy in the Cochiti Formation.

Rock Powder Preparation

Bearhead Rhyolite

Samples of the Bearhead Rhyolite were powdered for XRF and INA analysis. Each sample was prepared by first breaking the rock into ~6 cm diameter pieces using a hammer and steel plate. A hand sample and thin section specimen were set aside at this point. After visual inspection and handpicking, ~1 kg of the sample was crushed to < 1 cm diameter using a Bico™ chipmunk crusher equipped with tungsten carbide jaws. The jaw crusher was cleaned between each sample by scrubbing the plates with a steel brush and applying compressed air to all surfaces. Half of the crushed sample was reserved for $^{40}Ar/^{39}Ar$ dating using the cone and quarter method. Around 5 g of the remaining crushed fraction was then powdered to < 0.075 mm in a tungsten-carbide-lined Bico™ shatterbox for 2 minutes.

Peralta Tuff

Pumice samples were prepared for XRF and INA analysis by first removing the outer ~2-3 mm of each pumice with a steel brush. Hand samples and thin section specimens, when possible, were set aside at this point. Around 10 g of brushed sample

nd pumice samples < 1 cm diameter (cleaned with a nylon brush) were ultrasonically cleaned in reverse-osmosis water for 30 minutes and dried at 100 °C for 6 hours. After selecting unaltered pumice, the sample was then crushed and powdered like the rhyolite samples previously described.

Precision of Loss On Ignition Calculations

The amount of water retained in the samples (expressed as percent loss on ignition) was determined using the following method (method A). A ceramic crucible was wiped with low-lint laboratory tissue until visibly free of rock powder residue. The crucible was then labeled and weighed to ± 0.0005 g. Two to four grams of powdered sample was placed in the crucible and the crucible was reweighed to ± 0.0005 g. The crucible was then placed in a 110 °C oven for 2 hours. The crucible was then removed from the oven and allowed to cool to room temperature in a desiccator. Once cooled, the crucible was reweighed to ± 0.0005 g. Next, the crucible was placed in a 1000 °C oven for 2 hours. The crucible was then removed from the oven and cooled on a heat resistant surface until it could be placed in a desiccator. Once at room temperature, the crucible was reweighed to ± 0.0005 g. The weight loss after 110 °C is H_2O^- and the weight loss after 1000 °C is H_2O^+. The two combined give the total loss on ignition, expressed as total percentage loss on ignition (%LOI).

To determine the reproducibility of method A, duplicate and triplicate %LOI determinations were made on 13 samples (4 rhyolites and 9 tuffs) from this study. The percent differences of the calculated %LOIs range widely from 0.4 to 26.2 with 7.1 ± 7.7

% difference between samples. The variation in range for each analysis occurs equally in H_2O^- and H_2O^+ calculations.

In an alternative method (method B), %LOI was determined the following way. A ceramic crucible was washed in distilled water and placed in a 600 °C furnace until dry (~1-2 min.). The crucible was then cooled in a desiccator for ~15 min. After the sample number was marked on the crucible and weighed to ± 0.0005 g, 2 to 4 grams of sample are added and the crucible was reweighed. Next, the crucible was heated at 110 °C, cooled, and reweighed as in method A. For the high temperature step, the crucible was placed in a 900 °C oven for 2 hours. Afterwards, the crucibles were left to cool in the furnace until the furnace reached 300 °C (4-5 hours). The crucible was then placed in a desiccator until it reached room temperature. The crucible was finally weighed %LOI is calculated as described in method A.

To constrain whether method A or B is more precise, LOIs were determined at the same time on a series of five samples by each method. The results are listed in the table below.

Comparison of Two Methods for Determining %LOI

Sample	%LOI for Method A	% LOI for Method B	% Difference
1	0.9034	0.8219	9.0
2	0.5865	0.5708	2.7
3	0.7036	0.6685	5.0
4	0.6637	0.6941	4.4
5	1.1533	0.9417	18.3

These results indicate that method B lies within the precision of method A for all samples except 5. It appears, then, that both methods for calculating %LOI are valid. It is not

clear whether method B's precision is better than method A's because duplicate analyses were not performed in this experiment.

X-Ray Fluorescence Spectrometry

Bearhead Rhyolite and Peralta tuff samples were analyzed for major and selected trace elements (Rb, Sr, Nb, Y, Zr) using procedures outlined by Norrish and Hutton (1969) and Norrish and Chappell (1977). Just prior to making fused disks for XRF analysis, it is important to heat all of the powdered samples at ~100 °C for at least 30 minutes. The heating allows for more complete mixing of the sample and flux. Failure to heat powders (especially pumice) often leads to low major element totals (< 98%) for the XRF analysis.

Fused glass disks for major and trace element analysis were prepared at a 5:1 flux/sample ratio by mixing 8.50 g lithium tetraborate, 0.2740 g ammonium nitrate and 1.70 g powdered sample (all measurements to ± 0.0005 g) in a Au-Pt crucible. The mixture was fused at 1100 °C for 30 minutes, quenched in an Au-Pt mold at 450 °C for 10 minutes or an aluminum press at 350 °C for 15 minutes following the process of Norrish and Hutton (1969), and cooled to room temperature in a desiccator.

Major and trace element analyses were performed using a Rigaku 3030 XRF spectrometer at the University of Nevada, Las Vegas. For major elements, kV/ma was set at 50/30 while trace elements were run at 50/50 kV/ma. Slit, filter, and crystals varied according to the elements being analyzed. Data reduction was performed by an on-line computer. A large number of well-characterized standards were used to calibrate XRF

runs (see Appendix E). Analytical errors were calculated by multiple runs of in-laboratory standards (GA for major elements and MAG-1 for trace elements).

Instrumental Neutron Activation Analysis

Trace elements Cs, Co, Mo, Sm, Sc, Tb, U, La, Ce, Eu, Yb, Lu, Ta, Nd, Zn, Sb, W, Ba, Th, and Hf, were analyzed using INA methods described by Jacobs et al. (1977) and Lindstrom and Korotev (1982). Powdered samples were placed in capsules made from T21 Grade Suprasil™ (4 mm ID, 6 mm OD) tubing. The Suprasil™ vials were made by scoring and breaking the tubing into 16 cm lengths and then dividing each segment in half (8 to 9 cm lengths) using an oxygen-natural gas torch. The half-sealed vials were then soaked in aqua-regia solution for 30 minutes, rinsed five times with distilled water, covered, and dried at 100 °C for 12 hours. Approximately 200 to 250 mg of each sample was measured to ± 0.0001 g, their masses recorded, and placed in the vials. One blank, one blind standard, and 2 duplicates were also included. The vials were then sealed by melting the open end of the vial in on itself. Samples were irradiated at the Phoenix Memorial Laboratory Ford Nuclear Reactor at the University of Michigan for 20 hours at a fluence of ~ 1.5 X 10^{12} neutrons·s/cm^2. Counts were taken on each sample 1 and 5 weeks after irradiation at Phoenix Memorial Laboratory Ford Nuclear Reactor at the University of Michigan. The laboratory reports a systematic error of 3% resulting from position variations of the samples in the sample changer. The analysis was completed using the direct comparison INA technique with NIST SRM 1633a, Coal Fly Ash as the comparison standard. The certified elemental concentrations for the standard

were used where possible. For the non-certified elements, the consensus mean values from NBS Special Publication 260-111 were used. The accuracy and precision of INAA is listed in Appendix F.

Appendix E: Precision and Accuracy of XRF Analysis

Primary calibration standards

Major Elements: DNC-1; BHVO-1; PCC-1; AGV-1; GS-N; GA; W-2; BR; SCo-1; STM-1; GSP-1; RGM-1; QLO-1; AL-1

Trace Elements: G-2; W-2; BIR-1; BHVO-1; DNC-1; RGM-1; QLO-1; PCC-1; SCo-1; AGV-1 GSP-1; AN-G; DR-N; GS-N; MAG-1; Mica Mg; NBS-688

Element	Published concentration	Mean	1σ	% Accuracy	% Precision	Quantitation Limit
SiO_2	48.35	48.27	0.73	0.17	1.51	
Al_2O_3	17.35	17.53	0.37	1.04	2.11	
TiO_2	1.168	1.16	0.02	0.68	1.72	
Fe_2O_3	10.34	9.96	0.18	3.68	1.81	
MgO	8.46	8.57	0.26	1.30	3.03	0.12
CaO	12.17	12.05	0.17	0.99	1.41	0.028
Na_2O	2.16	2.15	0.03	0.46	1.40	
K_2O	0.19	0.19	0.01	0.00	5.26	
MnO	0.167	0.16	0.03	4.19	15.63	0.003
P_2O_5	0.133	0.15	0.01	12.78	3.33	0.043
Rb	149	157.1	2.34	5.44	1.49	
Sr	146	146.9	1.60	0.62	1.09	
Zr	126	119.4	2.51	5.24	2.10	
Y	28	26.0	1.85	7.14	7.10	
Nb	12	16.7	1.76	39.17	10.56	

NOTE: 9 replicate analyses of NIST 688 were used to determine the accuracy and precision of the XRF major element analyses. 7 replicate analyses of MAG-1 were used to determine the accuracy and precision of the XRF trace element analyses. Published concentrations were taken from the Special Issue of Geostandards Newsletter (July 1994).

Appendix F: Precision and Accuracy of INA Analysis

Standard NIST 278

Element	Published concentration	Mean	1σ	% Accuracy	% Precision
Ba	1140	1013.39	117.6999	11	11.6
Sc	5.1	5.01	0.0690	1.7	1.4
Zn	55	48.60	14.1426	11.6	29.1
Cs	5.5	5.13	0.0561	6.7	1.1
La	32	40.60	3.1929	7.08	7.9
Ce	62.2	83.15	1.9029	10.9	2.3
Nd	30	31.90	8.4141	6.3	26.4
Sm	5.7	5.66	0.1676	0.7	3.0
Eu	0.84	0.79	0.0648	5.8	8.2
Tb	1	1.11	0.0694	10.9	6.3
Yb	4.5	4.49	0.2397	0.3	5.3
Lu	0.73	0.63	0.0151	13.7	2.4
Hf	8.4	8.39	0.0361	0.1	0.4
Ta	1.2	1.50	0.1045	24.9	7.0
Th	12.4	12.04	0.1120	0.8	0.9
U	4.58	4.55	0.2596	0.6	5.7

NOTE: 3 replicate analyses of standard NIST 278 were used to determine the accuracy and precision of INA. Published concentrations were taken from the Special Issue of Geostandards News Letter (July 1994).

Appendix G: Chemical Abundances of Melt Inclusions in Quartz from the Peralta Tuff

	TWM1						
wt.%**	1/1	1/3	2/1	2/2	2/3	2/4	3/1
SiO_2	73.89	73.98	72.98	70.86	72.89	72.40	73.59
TiO_2	0.06	0.10	0.12	0.12	0.06	0.06	0.08
Al_2O_3	11.75	11.84	11.69	11.63	11.63	11.41	11.62
MgO	0.03	0.04	0.04	0.05	0.03	0.03	0.02
CaO	0.38	0.34	0.31	0.32	0.33	0.32	0.31
MnO	0.08	0.02	0.10	0.03	0.02	0.08	0.09
FeO*	0.62	0.51	0.53	0.53	0.56	0.61	0.61
Na_2O	2.62	2.61	3.56	3.62	3.60	3.33	2.97
K_2O	5.61	5.56	4.92	4.35	4.53	4.63	5.66
P_2O_5	0.027	0	0	0.035	0	0.039	0.008
SO_2	0	0.006	0.010	0	0	0	0
F	0	0.045	0.053	0.048	0.351	0.141	0
Cl	0.140	0.098	0.110	0.139	0.128	0.119	0.106
Total	95.19	95.15	94.43	91.71	94.12	93.17	95.06

*Total Fe, ** Electron Microprobe Analysis

	TWM1						
ppm#	1/1	2/1	2/1	2/2	2/3	2/4	3/1
H_2O (wt.%)		3.53	3.66	3.45			
Li		18	19	90			
B		12	12	10			
Rb		116	112	107			
Sr		4.0	4.9	6.2			
Y		21	22	22			
Zr		60	63	65			
Nb		24	24	21			
Ba		105	115	133			
La		14	14	11			
Ce		33	29	32			
Nd		13	13	11			
Th		12	8	10			
U		4	3	5			

Ion Microprobe Analysis

Appendix G: Chemical Abundances of Melt Inclusions in Quartz from the Peralta Tuff (cont.)

	TWM1						
wt.%**	3/2	3/3	3/4	3/5	4/1	4/2	4/3
SiO_2	72.88	72.16	72.36	70.21	73.04	72.68	73.75
TiO_2	0.09	0.11	0.09	0.04	0.08	0.09	0.12
Al_2O_3	11.86	11.59	11.57	11.43	11.77	11.76	11.64
MgO	0.02	0.04	0.03	0.04	0.04	0.04	0.01
CaO	0.32	0.32	0.35	0.32	0.34	0.32	0.32
MnO	0.05	0.10	0.03	0.07	0.09	0.06	0.07
FeO*	0.56	0.53	0.57	0.52	0.63	0.55	0.57
Na_2O	2.87	2.80	3.21	3.41	3.01	3.05	4.05
K_2O	5.71	5.58	5.28	4.61	5.47	5.44	5.68
P_2O_5	0	0.012	0.047	0.012	0	0	0
SO_2	0	0	0	0.021	0.006	0.022	0.001
F	0.016	0	0	0.053	0	0	0.188
Cl	0.118	0.133	0.123	0.114	0.112	0.113	0.089
Total	94.50	93.38	93.66	90.85	94.58	94.11	96.48

*Total Fe, ** Electron Microprobe Analysis

	TWM1						
ppm#	3/2	3/3	3/4	3/5	4/1	4/2	4/3
H_2O (wt.%)					2.20		1.75
Li					14		9
B					11		11
Rb					114		121
Sr					5.3		4.5
Y					22		22
Zr					63		60
Nb					23		24
Ba					112		123
La					13		12
Ce					21		30
Nd					8		13
Th					8		10
U					6		3

Ion Microprobe Analysis

Appendix G: Chemical Abundances of Melt Inclusions in Quartz from the Peralta Tuff (cont.)

	TWM1				CC3		
wt.%**	4/4	4/5	4/6	4/7	1/1	1/2	1/3
SiO_2	73.64	72.76	72.53	71.99	72.81	75.75	76.05
TiO_2	0.15	0.07	0.11	0.07	0.13	0.13	0.10
Al_2O_3	11.53	11.53	11.64	11.46	11.73	12.26	12.35
MgO	0.02	0.02	0.00	0.04	0.05	0.06	0.05
CaO	0.34	0.31	0.35	0.32	0.37	0.41	0.39
MnO	0.06	0.04	0.09	0.11	0.07	0.06	0.08
FeO*	0.54	0.52	0.56	0.49	0.59	0.53	0.65
Na_2O	2.65	2.79	3.22	2.78	3.48	3.11	3.74
K_2O	5.51	5.82	5.49	5.79	4.43	4.36	4.58
P_2O_5	0	0.074	0.004	0.027	0.035	0	0.031
SO_2	0.001	0	0	0.009	0	0.003	0.021
F	0.107	0.069	0.069	0	0.056	0.064	0.082
Cl	0.122	0.103	0.108	0.077	0.133	0.124	0.112
Total	94.67	94.12	94.17	93.17	93.88	96.85	98.23

*Total Fe, ** Electron Microprobe Analysis

	TWM1				CC3		
ppm#	4/4	4/5	4/6	4/7	1/1	1/2	1/3
H_2O (wt.%)			2.73	2.31	3.01		
Li			13	9	15		
B			12	10	11		
Rb			113	117	123		
Sr			4.5	4.9	9.8		
Y			21	20	18		
Zr			58	61	64		
Nb			23	26	28		
Ba			105	105	291		
La			14	11	19		
Ce			32	27	38		
Nd			11	13	12		
Th			9	13	13		
U			2	3	4		

Ion Microprobe Analysis

Appendix G: Chemical Abundances of Melt Inclusions in Quartz from the Peralta Tuff (cont.)

				CC3			
wt.%**	2/1	2/2	2/3	3/1	3/2	4/1	4/2
SiO_2	73.56	72.34	97.24	73.04	72.17	72.94	70.06
TiO_2	0.15	0.11	0.02	0.08	0.08	0.08	0.08
Al_2O_3	11.72	11.62	0.00	10.86	11.73	11.71	13.82
MgO	0.06	0.04	0.03	0.05	0.03	0.04	0.04
CaO	0.36	0.38	0.03	0.34	0.32	0.34	0.29
MnO	0.08	0.09	0.02	0.07	0.04	0.07	0.04
FeO*	0.54	0.59	0.01	0.49	0.61	0.57	0.36
Na_2O	3.30	3.55	0.00	3.61	3.59	3.27	3.78
K_2O	4.28	4.45	0.01	4.07	4.50	4.29	5.98
P_2O_5	0	0	0	0.035	0.004	0.008	0.043
SO_2	0.009	0.016	0.006	0.009	0.045	0.009	0.059
F	0.122	0.021	0.006	0	0.061	0.209	0.246
Cl	0.109	0.088	0.008	0.107	0.102	0.104	0.076
Total	94.29	93.29	97.37	92.76	93.27	93.64	94.86

*Total Fe, ** Electron Microprobe Analysis

				CC3			
ppm#	2/1	2/2	2/2	3/1	3/2	4/1	4/2
H_2O (wt.%)	2.88	2.55	3.42	2.85	3.32		
Li	17	28	4	67	29		
B	11	11	12	11	11		
Rb	109	111	119	104	111		
Sr	10.6	12.0	12.3	10.1	13.8		
Y	20	18	17	19	21		
Zr	63	64	58	64	62		
Nb	21	27	22	23	23		
Ba	377	392	386	308	377		
La	16	19	18	17	17		
Ce	40	41	33	37	32		
Nd	9	13	11	13	11		
Th	10	13	10	10	8		
U	5	5	4	6	0		

Ion Microprobe Analysis

Appendix G: Chemical Abundances of Melt Inclusions in Quartz from the Peralta Tuff (cont.)

				TA			
wt.%**	1/1	1/2	1/3	1/4	1/5	2/1	2/2
SiO_2	70.96	73.93	73.71	72.99	73.17	61.01	75.77
TiO_2	0.11	0.07	0.07	0.13	0.13	0.00	0.06
Al_2O_3	11.89	11.90	11.96	11.71	11.29	20.07	11.80
MgO	0.05	0.03	0.04	0.03	0.03	0.00	0.03
CaO	0.38	0.34	0.34	0.38	0.29	2.48	0.30
MnO	0.08	0.08	0.06	0.08	0.07	0.00	0.03
FeO*	0.58	0.51	0.52	0.55	0.54	0.17	0.46
Na_2O	4.67	3.53	3.72	3.29	2.74	7.29	4.68
K_2O	4.54	4.53	4.38	5.02	5.67	1.38	2.85
P_2O_5	0	0.008	0.016	0.039	0	0.020	0
SO_2	0.004	0.007	0.003	0	0.006	0.036	0.018
F	0.053	0	0.299	0.000	0.011	0.194	0.106
Cl	0.099	0.103	0.113	0.085	0.109	0	0.032
Total	93.41	95.04	95.23	94.32	94.05	92.64	96.14

*Total Fe, ** Electron Microprobe Analysis

				TA			
ppm#	1/1	1/2	1/2	1/4	1/5	2/1	2/2
H_2O (wt.%)		3.21	3.14				
Li		33	36				
B		10	10				
Rb		112	121				
Sr		6.7	6.5				
Y		20	20				
Zr		60	59				
Nb		25	23				
Ba		234	234				
La		15	18				
Ce		33	31				
Nd		9	10				
Th		8	10				
U		2	2				

Ion Microprobe Analysis

Appendix G: Chemical Abundances of Melt Inclusions in Quartz from the Peralta Tuff (cont.)

	TA	CAN				
wt.%**	2/3	1/1	1/2	1/4	1/5	1/6
SiO_2	61.50	72.58	73.443	73.542	74.174	74.913
TiO_2	0.01	0.109	0.094	0.114	0.107	0.119
Al_2O_3	20.88	11.668	11.533	11.59	11.932	11.988
MgO	0.00	0.042	0.032	0.056	0.042	0.056
CaO	2.47	0.33	0.366	0.32	0.367	0.305
MnO	0.00	0.086	0.063	0.08	0.022	0.068
FeO*	0.18	0.491	0.485	0.632	0.562	0.538
Na_2O	9.06	3.51	3.287	3.832	3.966	2.948
K_2O	1.38	4.411	4.4	4.169	4.158	4.836
P_2O_5	0.039	0	0.055	0.043	0	0.004
SO_2	0.006	0.021	0.009	0.003	0.007	0
F	0.013	0.273	0.069	0.011	0.000	0
Cl	0.005	0.100	0.124	0.087	0.096	0.100
Total	95.53	93.621	93.96	94.479	95.433	95.875

*Total Fe, ** Electron Microprobe Analysis

	TA	CAN				
ppm#	2/3	1/1	1/2	1/4	1/5	1/6
H_2O (wt.%)						
Li						
B						
Rb						
Sr						
Y						
Zr						
Nb						
Ba						
La						
Ce						
Nd						
Th						
U						

Ion Microprobe Analysis

Appendix G: Chemical Abundances of Melt Inclusions in Quartz from the Peralta Tuff (cont.)

	CAN					
wt.%**	2/1	2/2	2/3	2/4	2/5	3/1
SiO_2	71.26	73.60	72.44	76.71	80.55	72.10
TiO_2	0.10	0.11	0.06	0.12	0.10	0.17
Al_2O_3	11.61	11.55	11.60	9.64	8.91	11.21
MgO	0.04	0.06	0.06	0.04	0.01	0.04
CaO	0.33	0.31	0.38	0.31	0.27	0.35
MnO	0.09	0.06	0.05	0.06	0.09	0.07
FeO*	0.50	0.56	0.66	0.38	0.39	0.52
Na_2O	4.65	3.41	3.39	2.68	2.30	2.80
K_2O	5.17	4.75	4.69	3.69	3.98	5.05
P_2O_5	0.015	0	0	0.004	0.016	0.027
SO_2	0	0.015	0	0	0	0.030
F	0	0	0	0	0.057	0.056
Cl	0.101	0.112	0.115	0.094	0.108	0.127
Total	93.86	94.54	93.44	93.73	96.76	92.53

*Total Fe, ** Electron Microprobe Analysis

	CAN					
ppm#	2/1	2/2	2/3	2/4	2/5	3/1
H_2O (wt.%)	4.33		4.11		2.25	
Li	15		17		11	
B	12		15		10	
Rb	109		114		96	
Sr	12.1		10.6		12.2	
Y	17		16		15	
Zr	56		60		47	
Nb	20		19		14	
Ba	248		260		303	
La	13		13		13	
Ce	35		32		27	
Nd	9		9		9	
Th	11		10		9	
U	1		6		5	

Ion Microprobe Analysis

Appendix G: Chemical Abundances of Melt Inclusions in Quartz from the Peralta Tuff (cont.)

	CAN						
wt.%**	3/2	3/3	3/4	3/5	3/6	3/7	4/1
SiO_2	74.44	72.78	83.93	84.40	72.63	73.35	72.17
TiO_2	0.12	0.09	0.07	0.14	0.10	0.12	0.12
Al_2O_3	11.55	11.57	7.00	6.90	11.69	11.63	11.16
MgO	0.05	0.02	0.02	0.02	0.04	0.06	0.04
CaO	0.35	0.36	0.24	0.25	0.37	0.34	0.30
MnO	0.08	0.06	0.02	0.04	0.07	0.05	0.09
FeO*	0.54	0.53	0.35	0.32	0.50	0.58	0.57
Na_2O	3.85	3.55	1.96	2.27	3.17	3.55	3.39
K_2O	4.09	4.37	2.69	2.53	4.80	4.67	4.31
P_2O_5	0	0.020	0.039	0.079	0.023	0.004	0.012
SO_2	0	0	0	0.033	0	0	0.031
F	0.384	0.069	0	0.059	0.155	0.051	0.213
Cl	0.119	0.122	0.096	0.052	0.114	0.137	0.098
Total	95.56	93.54	96.42	97.08	93.66	94.54	92.50

*Total Fe, ** Electron Microprobe Analysis

	CAN						
ppm#	3/2	3/3	3/4	3/5	3/6	3/7	4/1
H_2O (wt.%)		3.96			3.68		2.63
Li		73			13		66
B		12			13		12
Rb		114			124		120
Sr		9.4			12.8		12.6
Y		18			19		19
Zr		63			61		62
Nb		22			22		20
Ba		221			286		272
La		15			15		17
Ce		33			31		30
Nd		8			12		10
Th		10			10		10
U		5			5		0

Ion Microprobe Analysis

Appendix G: Chemical Abundances of Melt Inclusions in Quartz from the Peralta Tuff (cont.)

	CAN			1 PT		TWM2
wt.%**	4/2	4/3	4/4	1/1	2/1	1/1
SiO_2	74.94	74.53	76.51	70.65	67.58	70.74
TiO_2	0.14	0.12	0.08	0.11	0.08	0.12
Al_2O_3	11.78	11.54	12.21	12.00	14.00	11.13
MgO	0.05	0.05	0.04	0.00	0.00	0.02
CaO	0.34	0.36	0.36	0.28	0.36	0.33
MnO	0.08	0.07	0.04	0.05	0.02	0.05
FeO*	0.56	0.52	0.60	0.28	0.37	0.56
Na_2O	3.64	3.76	3.92	3.76	3.71	0.13
K_2O	4.11	4.38	3.99	3.89	5.47	4.53
P_2O_5	0	0.004	0.012	0.027	0.039	0
SO_2	0	0.039	0.036	0	0	0.025
F	0.000	0.008	0.270	0.173	0.217	0.141
Cl	0.106	0.102	0.125	0.017	0.041	0.103
Total	95.74	95.47	98.18	91.25	91.89	87.88

*Total Fe, ** Electron Microprobe Analysis

	CAN			1PT		TWM2
ppm#	4/2	4/3	4/4	1/1	2/1	1/1
H_2O (wt.%)	2.87			5.4		2.93
Li	22			127		12
B	10			10		10
Rb	106			101		146
Sr	10.9			20.9		7.1
Y	17			15		26
Zr	59			50		85
Nb	20			24		31
Ba	276			45		212
La	16			8		18
Ce	32			17		9
Nd	12			6		14
Th	10			6		11
U	5			2		6

Ion Microprobe Analysis

Appendix G: Chemical Abundances of Melt Inclusions in Quartz from the Peralta Tuff (cont.)

	TWM 2					
wt.%**	2/1	2/2	2/3	3/1	3/2	4/1
SiO_2	72.75	72.34	70.56	69.76	74.32	70.03
TiO_2	0.06	0.10	0.08	0.09	0.07	0.10
Al_2O_3	11.26	11.38	11.16	11.47	12.33	13.07
MgO	0.08	0.01	0.02	0.05	0.05	0.04
CaO	0.38	0.32	0.33	0.33	0.33	0.32
MnO	0.10	0.13	0.06	0.05	0.07	0.09
FeO*	0.50	0.47	0.47	0.51	0.47	0.48
Na_2O	3.09	3.56	3.53	6.15	3.40	3.43
K_2O	4.24	4.22	4.10	4.20	4.89	5.37
P_2O_5	0.008	0	0	0	0.051	0.019
SO_2	0.024	0.009	0.013	0	0.039	0.048
F	0.107	0	0.067	0	0.005	0
Cl	0.120	0.100	0.108	0.098	0.114	0.100
Total	92.72	92.63	90.49	92.71	96.13	93.09

*Total Fe, ** Electron Microprobe Analysis

	TWM 2					
ppm#	2/1	2/2	2/3	3/1	3/2	4/1
H_2O (wt.%)	3.68	2.92		3.34		
Li	66	44		69		
B	10	9		10		
Rb	115	97		110		
Sr	5.9	4.6		6.2		
Y	22	19		20		
Zr	63	58		73		
Nb	25	22		27		
Ba	143	110		171		
La	14	11		15		
Ce	30	25		33		
Nd	11	9		10		
Th	11	9		13		
U	5	3		6		

Ion Microprobe Analysis

Appendix G: Chemical Abundances of Melt Inclusions in Quartz from the Peralta Tuff (cont.)

	TWM 2			TRB	
wt.%**	4/2	4/3	4/4	1/3	1/4
SiO_2	73.14	67.96	71.47	86.70	73.01
TiO_2	0.12	0.11	0.07	0.09	0.09
Al_2O_3	10.39	13.88	12.23	4.90	11.61
MgO	0.05	0.02	0.02	0.01	0.06
CaO	0.28	0.33	0.45	0.17	0.35
MnO	0.11	0.02	0.07	0.01	0.02
FeO*	0.61	0.41	0.53	0.22	0.53
Na_2O	2.82	3.57	2.36	1.56	3.29
K_2O	4.46	6.05	4.67	1.91	4.79
P_2O_5	0.039	0.047	0.027	0.032	0
SO_2	0	0	0.021	0	0
F	0.155	0.096	0.086	0.095	0.000
Cl	0.136	0.053	0.116	0.049	0.129
Total	92.30	92.53	92.11	95.74	93.87

*Total Fe, ** Electron Microprobe Analysis

Appendix G: Chemical Profiles of Sanidine Phenocrysts from the Peralta Tuff

	TA			TWM2			TWM1
wt.%	2/4	2/5	2/6	4/5	4/6	4/7	1/2
SiO_2	62.93	64.31	64.31	63.57	64.57	64.79	64.46
Al_2O_3	19.00	19.26	19.26	19.37	19.25	19.55	19.28
CaO	0.22	0.21	0.23	0.22	0.22	0.20	0.23
FeO*	0.12	0.14	0.16	0.13	0.12	0.13	0.12
Na_2O	4.34	4.45	3.03	4.53	4.30	4.69	4.41
K_2O	9.58	9.50	9.50	9.77	9.83	9.98	9.85
SrO	0.02	0.05	0.01	0.06	0.01	0.01	0.03
BaO	1.21	1.23	1.19	1.31	1.29	1.08	0.82
Total	97.41	99.15	97.69	98.96	99.59	100.42	99.19

*Total Fe

	TWM1		CC3			
wt.%	1/5	1/6	4/4	4/5	4/6	4/7
SiO_2	65.35	65.57	63.73	64.59	63.96	64.35
Al_2O_3	19.41	19.56	19.44	19.45	19.58	19.57
CaO	0.22	0.19	0.23	0.21	0.25	0.24
FeO	0.11	0.13	0.11	0.10	0.09	0.12
Na_2O	4.50	4.60	2.90	4.54	4.64	4.59
K_2O	9.79	9.90	9.54	9.64	9.25	9.35
SrO	0.00	0.00	0.04	0.00	0.04	0.03
BaO	0.78	0.65	2.18	1.04	1.99	1.57
Total	100.16	100.59	98.16	99.58	99.79	99.82

APPENDIX H

Electron Microprobe Analysis

Major and minor element analyses were completed on melt inclusions in quartz and feldspar from 6 Peralta Tuff samples (1PT, TWM1 and 2, TRB, TA, CC3 and CAN). Five quartz and feldspar grains were handpicked from each of the six units and cleaned with acetone. Under the guidance of Dr. Nelia Dunbar (New Mexico Bureau of Mines and Mineral Resources), quartz, feldspar, and NIST 610 grains were sealed in epoxy mounts and left to cure for 12 hours at 65 °C. After cooling for several hours, the epoxy mount was ground until melt inclusions in the interior of the grains were exposed on the surface (3 to 5 minutes using 68 and 30 μm diamond impregnated disks). To determine whether melt inclusions were exposed, the mount was periodically examined under transmitted and reflected light. The ground side of the mount was further polished for 3 to 5 minutes with 15, 6, and < 2 μm lose diamond grit. The mount was then reexamined under transmitted and reflected light to confirm that melt inclusions were exposed on the surface. The grinding and polishing process was repeated until inclusions were exposed. Once the melt inclusions were exposed, each grain was sketched and labeled. Oil and dirt was removed from the mount's surface using petroleum ether, and the polished surface of the mount was sputter coated with 20 μm of carbon for electron microprobe analysis. During the analysis NIST 610 and inter-laboratory standards VG 586 (rhyolite),

KE 12 (glass), orthoclase, and albite were repeatedly run as standards. Accuracy and precision of analyses are listed in Appendix I.

Ion Microprobe Analysis

Following the ion microprobe laboratory procedure described in Hervig and Dunbar (1992), ion microprobe analyses were made on a Cameca IMS 3f instrument at Arizona State University by Dr. N.W. Dunbar. A 1-2 nA mass-analyzed primary beam of $^{16}O^-$ ions was focussed to a 20-25 μm in diameter spot. Secondary ions were accelerated to +4.5 keV and the transfer optics and field aperature were set to accept secondary ions into the mass spectrometer from a circular area 20 μm in diameter on the sample. The energy bandpass was set at 40 eV. After the secondary ion signal stabilized the samples voltage was ramped ±100 V from 4500 V while the intensity of $^{30}Si^+$ ions was monitored. The sample voltage was returned to the centroid of the intensity vs. sample potential curve to correct for the small amount of charging which occurred. Molecular ion interferences were removed by collecting secondary ion intensities at high energies, which were achieved by offsetting the sample voltage –75 V from the centroid position for H, ^{7}Li, ^{11}B, ^{19}F, ^{31}P, ^{47}Ti, ^{54}Fe, ^{85}Rb, ^{88}Sr, ^{89}Y, ^{90}Zr, ^{93}Nb, ^{138}Ba, ^{140}Ce, and ^{232}Th. Trace elements were calibrated against NBS 610, a sodium- and silica-rich glass doped with 61 trace elements at the 500 ppm level. Comparison of NBS 610 with bulk analyzed rhyolite glasses indicated that the trace elements studies were within 10% of their assayed or nominal concentration. Accuracy and precision of analyses listed in Appendix J.

Appendix I: Precision and Accuracy for Electron Microprobe Analysis of Melt Inclusions from the Peralta Tuff

Element	VG 586	KN 18	Mean VG 568	Mean KN 18	1σ	% Acc.	% Prec.
SiO_2	76.71		76.50		0.2969	0.3	0.7
Al_2O_3	12.06		12.15		0.1419	0.7	3.3
TiO_2	0.12		0.08		0.0305	34.3	67.4
FeO	0.48		1.14		0.0372	43.0	6.1
MgO		0.01		0.0003	0.0007	97.5	700.0
CaO	0.50		0.43		0.0296	13.5	11.0
Na_2O	3.75		3.96		0.3691	5.7	30.0
K_2O	4.89		4.97		0.0549	1.7	2.5
MnO	0.03		0.03		0.0199	11.5	91.4
P_2O_5							
Cl		0.37		0.32	0.0219	39.3	93.0
F		0.64		0.39	0.2375	14.7	13.4

NOTE: 16 replicate analyses of VG 586 and 8 replicate analyses of KN 18 used to determine precision of the major element abundances in glass. Concentrations for VG 586 and KN 18 from Dr. N.W. Dunbar.

Precision and Accuracy for Electron Microprobe Analysis of Sanidine from the Peralta Tuff

Orthoclase Element	Conc. wt. %	Mean	1σ	% Accuracy	% Precision
SiO_2	64.79	64.85	0.0866	0.1	0.2
Al_2O_3	16.72	16.69	0.0366	0.2	0.3
FeO	1.88	1.77	0.0301	5.6	2.2
CaO		0.01	0.0063		70.7
Na_2O	0.91	1.00	0.4708	10.4	108.3
K_2O	15.49	15.52	0.0665	0.2	0.5
SrO		0.01	0.0133		64.4
BaO	0.05	0.06	0.0201		54.4
Albite Element	**Conc. wt. %**	**Mean**	**1σ**	**% Accuracy**	**% Precision**
SiO_2	68.24	68.35	0.2778	0.2	0.6
Al_2O_3	19.90	20.16	0.1202	1.3	0.8
FeO					
CaO	0.03	0.02	0.0116	22.5	69.9
Na_2O	11.94	11.75	0.3508	1.6	4.4
K_2O	0.04	0.01	0.0024	70.0	25.0

NOTE: 8 replicate analyses of orthoclase standard and 4 replicate analyses of albite standard used to determine precision and accuracy of major and trace element abundanses in feldspar. Concentrations for orthoclase and albite taken from Dr. N.W. Dunbar.

Appendix J: Precision and Accuracy for Ion Microprobe Analysis of Melt Inclusions from the Peralta Tuff

Element	Conc. (ppm) Mean NBS-610		1σ	% Accuracy	% Precision
Li	482	598	11	24.1	0.50
B	358	344	8	3.9	0.58
Rb	430	415	13	3.5	2.17
Sr	505	549	11	8.7	0.18
Y	453	480	14	6.0	1.46
Zr	400	517	18	29.3	0.39
Nb	382	520	10	36.1	1.92
Ba	416	553	16	32.9	0.72
La	437	504	19	15.3	0.99
Ce	443	534	20	20.5	3.37
Nd	430	507	7	17.9	2.56
Th	463	626	33	35.2	1.92
U	463	522	37	12.7	4.02

NOTE: 7 replicate analyses of NBS-610 used to determine precision of the trace and water abundances in glass. Concentrations for NBS-610 from the Special Issue of Geostandards News Letter (July 1994).

Appendix K: Geochronology of the Bearhead Rhyolite

$^{40}Ar/^{39}Ar$	$^{37}Ar/^{39}Ar$	$^{36}Ar/^{39}Ar$ (X 10^{-3})	$^{39}Ar_K$ (X 10^{-15} mol)	K/Ca	$\%^{40}Ar^*$	Age (Ma)	1σ (Ma)	Laboratory
8843P, J = 1.584 X 10^{-3}, single sanidine crystals								
2.513	0.0074	0.1850	20.0	69.1	95.1	6.82	0.05	NMT
2.512	0.0000	0.1740	12.0	-	95.2	6.82	0.06	NMT
2.539	0.0065	0.2060	11.2	78.6	94.9	6.87	0.05	NMT
2.531	0.0000	0.1600	29.2	-	95.4	6.89	0.05	NMT
2.565	0.0111	0.2290	14.9	46.0	94.7	6.93	0.05	NMT
2.706	0.0160	0.7000	14.5	31.9	89.9	6.94	0.05	NMT
					Mean:	**6.88**	**+/-**	**0.05**
- denotes an infinite K/Ca value								
RH1, J = 1.618 X 10^{-3}, single sanidine crystals								
2.357	0.0095	0.0797	18.8	53.6	96.1	6.60	0.05	NMT
2.349	0.0031	0.0476	10.7	165.1	96.5	6.60	0.05	NMT
5.502	0.0310	10.70	7.7	16.5	41.2	6.61	0.08	NMT
2.374	0.0132	0.1180	18.4	38.7	95.7	6.62	0.05	NMT
2.378	0.0166	0.1190	10.4	30.7	95.7	6.63	0.05	NMT
2.371	0.0000	0.0713	13.8	-	96.2	6.65	0.05	NMT
2.379	0.0000	0.0960	11.7	-	95.9	6.65	0.05	NMT
2.393	0.0086	0.1470	15.5	59.7	95.3	6.65	0.05	NMT
2.382	0.0071	0.1080	14.0	71.9	95.8	6.65	0.05	NMT
2.362	0.0252	0.0450	5.80	20.3	96.6	6.65	0.06	NMT
2.381	0.0129	0.1020	15.9	39.7	95.9	6.65	0.05	NMT
2.386	0.0188	0.1160	8.30	27.1	95.7	6.66	0.06	NMT
2.380	0.0000	0.0726	7.44	-	96.2	6.67	0.05	NMT
2.411	0.0190	0.1520	5.64	26.9	95.3	6.70	0.06	NMT
2.405	0.0000	0.0810	11.7	-	96.1	6.74	0.05	NMT
2.425	*0.0000*	*0.1190*	*2.47*	-	*95.7*	*6.76*	*0.07*	*NMT*
					Mean:	**6.65**	**+/-**	**0.05**
Italics denote an analysis whose age lies outside of 2σ of the mean age; - denote infinite K/Ca value								
DB, J = 1.580 X 10^{-3}, single sanidine crystals								
2.484	0.0159	0.0691	15.5	32.1	96.4	6.82	0.05	NMT
2.506	0.0000	0.0524	5.35	-	96.6	6.89	0.06	NMT
2.527	0.0134	0.0652	7.28	38.1	96.5	6.94	0.06	NMT
2.582	0.0934	0.1200	2.58	5.5	96.2	7.07	0.07	NMT
					Mean:	**6.93**	**+/-**	**0.11**
- denotes an infinite K/Ca value								
TC, J = 1.544 X 10^{-3}, single sanidine crystals and # = ~40 sanidine crystals								
2.530	0.2536	0.4200	3.69	2.0	93.1	6.56	0.06	NMT
2.830	0.2150	1.1510	15.0	2.4	86.1	6.78#	0.06	NMT
2.544	0.0554	0.1140	5.82	9.2	96.1	6.80	0.06	NMT
2.517	0.2380	0.0702	3.12	2.1	97.1	6.81	0.07	NMT
2.693	0.1911	0.5979	5.62	2.7	91.4	6.85#	0.07	NMT
2.835	0.1572	0.8169	13.1	3.2	89.4	7.06#	0.06	NMT
					Mean:	**6.81**	**+/-**	**0.16**

Appendix K: Geochronology of the Bearhead Rhyolite (cont.)

$^{40}Ar/^{39}Ar$	$^{37}Ar/^{39}Ar$	$^{36}Ar/^{39}Ar$ (X 10^{-3})	$^{39}Ar_K$ (X 10^{-15} mol)	K/Ca	$\%^{40}Ar^*$	Age (Ma)	1σ (Ma)	Laboratory
ERP1, J = 1.614 X 10^{-3}, single sanidine crystals								
2.430	*0.0879*	*0.4240*	*3.15*	*5.8*	*92.3*	*6.52*	*0.06*	*NMT*
2.543	0.0106	0.7230	24.1	48.1	88.9	6.57	0.05	NMT
2.452	0.0058	0.3780	34.2	88.4	92.7	6.61	0.05	NMT
2.369	0.0047	0.0706	17.6	108.6	96.2	6.62	0.05	NMT
2.459	0.0100	0.3580	19.9	51.0	92.9	6.64	0.05	NMT
2.416	0.1861	0.2540	5.00	2.7	94.6	6.65	0.06	NMT
2.396	0.0054	0.1240	11.8	95.2	95.6	6.66	0.05	NMT
2.439	0.0088	0.2510	12.3	58.0	94.2	6.68	0.05	NMT
2.450	0.0059	0.2840	4.37	86.5	93.8	6.68	0.06	NMT
2.408	0.0021	0.1310	20.2	241.8	95.5	6.69	0.05	NMT
2.406	0.0001	0.1160	13.4	4515.1	95.7	6.69	0.05	NMT
2.407	0.0642	0.1320	16.1	7.9	95.7	6.70	0.05	NMT
2.404	0.0002	0.0688	10.4	2538.3	96.3	6.73	0.05	NMT
2.414	0.1097	0.1310	6.87	4.7	95.9	6.73	0.06	NMT
2.447	0.0875	0.1900	7.51	5.8	95.1	6.77	0.06	NMT
					Mean:	**6.66**	**+/-**	**0.06**

Italics denote an analysis whose age lies outside of 2σ of the mean age.

CJ1, J = 1.598 X 10^{-3}, single sanidine crystals and # = ~60 sanidine crystals								
2.520	0.0000	0.4790	9.95	-	91.7	6.65	0.05	NMT
2.571	0.0193	0.5790	9.95	26.4	90.7	6.71	0.05	NMT
2.588	0.0214	[illegible]	4.02	23.8	91.2	6.79	0.06	NMT
3.082	0.1227	[illegible]	4.05	4.2	76.9	6.82	0.06	NMT
2.857	0.0547	[illegible]		9.3	83.1	6.83	0.07	NMT
2.603	0.0870	[illegible]			91.5	6.85#	0.06	NMT
2.640	0.1860	0.6447	[illegible]		90.7	6.90#	0.06	NMT
2.682	0.1818	0.5961	9.12	[illegible]	[illegible]	7.06#	0.06	NMT
2.652	0.0551	0.4539	6.33	9.3	[illegible]	[illegible]06#	0.06	NMT
2.695	0.1300	0.5560	7.68	3.9	91.7	[illegible]12#	0.06	NMT
2.719	0.1820	0.6245	10.6	2.8	91.1	7.14#	0.06	NMT
2.788	0.1865	0.8571	16.8	2.7	88.9	7.14#	0.07	NMT
2.917	*0.2185*	*0.9350*	*12.2*	*2.3*	*88.7*	*7.45#*	*0.08*	*NMT*
					Mean:	**6.96**	**+/-**	**0.22**

- denotes an infinite K/Ca value

PN2, J = 1.596 X 10^{-3}, single sanidine crystals								
0.454	0.0411	0.3630	12.41	68.4	72.3	1.31	0.08	UH
0.674	0.0000	0.4930	0.926	-	68.2	1.32	0.13	NMT
0.477	0.0422	0.6140	8.05	66.5	65.8	1.37	0.11	UH
0.632	0.0000	0.1540	1.19	-	81.9	1.49	0.08	NMT
0.662	0.0000	0.2120	1.16	-	80.1	1.53	0.08	NMT
0.688	0.0000	0.0721	0.959	-	86.9	1.72	0.09	NMT
					Mean:	**1.46**	**+/-**	**0.16**

- denotes an infinite K/Ca value

Appendix K: Geochronology of the Bearhead Rhyolite (cont.)

$^{40}Ar/^{39}Ar$	$^{37}Ar/^{39}Ar$	$^{36}Ar/^{39}Ar$ (X 10^{-3})	$^{39}Ar_K$ (X 10^{-15} mol)	K/Ca	$\%^{40}Ar^*$	Age (Ma)	1σ (Ma)	Laboratory
WBHP, J = 1.614 X 10^{-3}, single sanidine crystals and # = 12 sanidine crystals								
2.249	0.2064	0.3590	2.28	2.5	92.8	6.08#	0.08	NMT
2.275	0.1693	0.3199	1.70	3.0	93.3	6.18#	0.09	NMT
2.452	0.0000	0.7660	0.901	-	88.0	6.27	0.14	NMT
2.364	0.1199	0.2230	4.23	4.3	94.6	6.51#	0.04	NMT
2.449	0.0000	0.2240	1.08	-	94.5	6.73	0.10	NMT
2.475	0.0000	0.2390	0.860	-	94.4	6.79	0.14	NMT
2.448	0.0000	0.0504	1.01	-	96.6	6.87	0.13	NMT
2.372	0.0508	2.8420	6.37	55.3	72.4	6.89	0.17	UH
2.401	0.1248	1.9710	3.84	22.5	78.9	6.98	0.26	UH
2.451	0.0066	-0.1080	1.43	77.9	98.5	7.02	0.10	NMT
					Mean:	**6.63**	**+/-**	**0.35**

- denotes an infinite K/Ca value

CY1, J = 1.620 X 10^{-3}, single sanidine crystals and # = 3 to 4 sanidine crystals								
2.161	0.0212	0.3000	11.6	132.8	92.7	5.85#	0.11	UH
2.166	0.0069	0.2480	15.2	409.5	93.5	5.91	0.10	UH
2.151	0.0000	0.1800	10.1	-	94.3	5.92	0.12	UH
2.181	0.0043	0.2630	9.57	647.2	93.3	5.94	0.14	UH
2.152	0.0059	0.0890	22.9	475.0	95.6	6.00	0.08	UH
2.153	0.0000	0.0910	11.8	-	95.5	6.00#	0.11	UH
2.242	0.0056	0.3820	16.4	504.6	91.9	6.01	0.09	UH
2.137	0.0002	0.00001	19.2	16149.4	96.7	6.03#	0.08	UH
2.144	0.0063	0.0090	40.1	449.3	96.7	6.05	0.06	UH
2.145	0.0000	0.0000	20.2	-	96.8	6.06#	0.08	UH
2.155	0.0058	0.0110	30.5	481.7	96.7	6.08	0.07	UH
					Mean:	**5.99**	**+/-**	**0.07**

- denotes an infinite K/Ca value

SEAP1, J = 1.610 X 10^{-3}single sanidine crystals and # = 5 to 10 sanidine crystals								
2.935	0.0186	1.8670	7.44	151.0	78.9	6.70#	0.19	UH
2.714	0.0000	0.9900	9.77	-	86.7	6.82#	0.15	UH
3.015	0.0089	1.9150	9.92	314.2	78.9	6.90#	0.13	UH
3.008	0.0000	1.7170	8.82	-	80.8	7.05#	0.13	UH
3.132	0.0000	1.9690	4.25	-	79.2	7.19#	0.21	UH
2.945	0.0091	1.2900	8.00	307.9	84.7	7.23#	0.19	UH
3.264	0.0000	2.2710	5.72	-	77.3	7.31	0.17	UH
					Mean:	**7.03**	**+/-**	**0.23**

- denotes an infinite K/Ca value

Appendix K: Geochronology of the Bearhead Rhyolite (cont.)

$^{40}Ar/^{39}Ar$	$^{37}Ar/^{39}Ar$	$^{36}Ar/^{39}Ar$ (X 10^{-3})	$^{39}Ar_K$ X 10^{-15} mol)	K/Ca	$\%^{40}Ar^*$	Age (Ma)	1σ (Ma)	Laboratory
CYF1, J = 1.578 X 10^{-5}, single sanidine crystals								
2.213	0.0058	0.0040	20.3	487.8	96.9	6.09	0.10	UH
2.233	0.0055	0.0220	19.3	510.0	96.7	6.14	0.08	UH
2.243	0.0049	0.0450	17.9	577.7	96.4	6.14	0.09	UH
2.237	0.0058	0.0090	33.1	483.1	96.8	6.16	0.07	UH
2.264	0.0058	0.0760	29.0	482.3	96.0	6.17	0.07	UH
2.245	0.0062	0.0130	20.3	454.3	96.8	6.18	0.08	UH
2.265	0.0065	0.0020	23.3	434.6	97.0	6.24	0.09	UH
					Mean:	**6.16**	**+/- 0.05**	
NBC1, J = 1.601 X 10^{-3}, 6 to 13 sanidine crystals								
2.472	0.1904	0.4430	9.51	14.8	92.4	6.59	0.11	UH
2.439	0.0220	0.1720	25.1	127.7	95.1	6.69	0.10	UH
2.491	0.1023	0.2680	10.7	27.5	94.3	6.77	0.11	UH
2.469	0.0633	0.1540	10.3	44.4	95.5	6.80	0.17	UH
2.453	0.0438	0.0630	11.5	64.2	96.5	6.83	0.14	UH
2.477	0.0000	0.0280	8.75	-	96.9	6.92	0.15	UH
					Mean:	**6.77**	**+/- 0.11**	
- denotes an infinite K/Ca value								
SM1, J = 1.541 X 10^{-3}, single sanidine crystals and # = 3 to 17 sanidine crystals								
2.575	0.0006	0.2820	33.1	4878.5	94.1	6.72	0.08	UH
2.503	0.0066	0.0110	18.3	428.7	97.1	6.74#	0.10	UH
2.484	0.0213	-0.0970	13.8	131.7	98.4	6.78#	0.10	UH
2.518	0.0487	-0.0030	16.2	57.7	97.4	6.80#	0.09	UH
2.484	0.0000	-0.1600	19.3	-	99.1	6.83	0.09	UH
2.493	0.0000	-0.1280	22.6	-	98.7	6.83#	0.09	UH
2.483	0.0000	-0.2390	11.7	-	100.0	6.89#	0.10	UH
					Mean:	**6.80**	**+/- 0.06**	
- denotes an infinite K/Ca value								
NHC, J = 1.624 X 10^{-3}, single sanidine crystals								
2.310	0.0009	0.1320	8.23	299.3	95.4	6.44	0.15	UH
2.445	0.0107	0.5640	11.7	261.5	90.4	6.46	0.11	UH
3.091	0.0125	2.7570	9.06	225.1	71.4	6.46	0.14	UH
2.345	0.0105	0.1640	9.94	184.3	95.0	6.52	0.13	UH
2.333	0.1219	0.0920	13.6	23.1	96.2	6.57	0.09	UH
2.331	0.0087	0.0500	11.8	323.9	96.4	6.57	0.11	UH
2.325	0.0094	0.0150	13.3	300.4	96.9	6.59	0.11	UH
2.348	0.0110	0.0780	19.7	256.6	96.1	6.60	0.07	UH
2.593	0.0120	0.8400	16.8	233.5	87.8	6.66	0.08	UH
					Mean:	**6.54**	**+/- 0.08**	

Appendix K: Geochronology of the Bearhead Rhyolite (cont.)

$^{40}Ar/^{39}Ar$	$^{37}Ar/^{39}Ar$	$^{36}Ar/^{39}Ar$ (X 10^{-3})	$^{39}Ar_K$ (X 10^{-15} mol)	K/Ca	$\%^{40}Ar^*$	Age (Ma)	1σ (Ma)	Laboratory
CP, J = 1.594 X 10^{-3}, ~80 sanidine crystals, # = 3 sanidine crystals, '+ = single sanidine crystal								
2.352	6.7870	0.0320	7.2	414.0	96.8	6.75#	0.16	UH
2.503	0.0362	0.2161	18.8	14.1	94.8	6.81	0.06	NMT
2.412	0.0175	-0.1540	11.7	160.6	99.1	6.92+	0.13	UH
2.580	0.0476	0.3397	22.5	10.7	93.6	6.93	0.06	NMT
2.599	0.0603	0.3556	18.8	8.5	93.5	6.98	0.06	NMT
2.590	0.0565	0.2960	10.6	9.0	94.1	7.00	0.06	NMT
					Mean:	**6.90**	**+/-**	**0.09**
31B, J = 1.590 X 10^{-3}, single sanidine crystals and # = 3 to 9 sanidine crystals								
2.793	0.0177	1.2280	47.3	28.8	84.6	6.76#	0.05	NMT
2.591	0.1309	0.5197	16.4	3.9	91.8	6.81#	0.06	NMT
2.378	0.0123	0.2670	20.4	227.9	94.1	6.81	0.09	UH
2.615	0.0105	0.5519	33.8	48.8	91.2	6.82#	0.05	NMT
2.382	0.0444	0.3170	17.2	63.3	93.7	6.82#	0.10	UH
2.701	0.0146	0.8243	33.4	34.9	88.5	6.84#	0.06	NMT
2.398	0.0000	0.0320	17.8	-	96.8	6.86	0.09	UH
2.634	0.0128	0.5667	35.4	39.8	91.1	6.87#	0.06	NMT
2.604	0.0170	0.4589	30.3	30.1	92.2	6.87#	0.06	NMT
2.401	0.0024	0.1820	30.5	1153.5	95.1	6.87	0.09	UH
2.682	0.0323	0.7077	31.2	15.8	89.7	6.89#	0.06	NMT
3.039	0.0303	1.9100	36.8	16.8	79.2	6.90#	0.06	NMT
2.411	0.0000	0.4040	18.5	-	92.7	6.90	0.09	UH
2.428	0.0041	-0.0210	16.5	683.9	97.5	6.95	0.10	UH
2.427	0.0064	0.0600	11.8	441.7	96.5	6.95	0.11	UH
2.454	0.0000	0.0100	11.7	-	97.1	7.03	0.11	UH
2.460	0.0055	-0.0650	10.1	512.1	98.0	7.04#	0.01	UH
2.469	*0.0000*	*0.0370*	*14.7*	-	*96.8*	*7.07#*	*0.10*	*UH*
					Mean:	**6.89**	**+/-**	**0.07**
Italics denote an analysis whose age lies outside of 2σ of the mean age; - denote infinite K/Ca value								
CB, J = 1.573 X 10^{-3}, ~8 sanidine crystals								
2.460	0.0164	0.1919	18.2	31.1	94.9	6.62	0.05	NMT
2.502	0.0137	0.2297	23.0	37.2	94.6	6.70	0.05	NMT
3.454	0.0288	3.3870	28.9	17.7	69.1	6.76	0.06	NMT
					Mean:	**6.69**	**+/-**	**0.07**
NAP, J = 1.586 X 10^{-3}, 4 to 5 sandine crystals								
2.297	0.0105	0.5430	8.15	268.5	90.9	6.56	0.15	UH
2.378	0.0321	0.2370	5.22	87.6	94.5	6.79	0.20	UH
2.425	0.0000	0.0950	7.63	-	97.8	6.93	0.15	UH
					Mean:	**6.76**	**+/-**	**0.19**

- denotes an infinite K/Ca value

Appendix K: Geochronology of the Bearhead Rhyolite (cont.)

$^{40}Ar/^{39}Ar$	$^{37}Ar/^{39}Ar$	$^{36}Ar/^{39}Ar$ (X 10^{-3})	$^{39}Ar_K$ (X 10^{-15} mol)	K/Ca	%$^{40}Ar^*$	Age (Ma)	1σ (Ma)	Laboratory
EBHP, J = 1.624 X 10^{-3}, single sanidine crystals								
2.415	0.0137	3.0800	6.31	205.5	71.2	7.06	0.15	UH
2.415	0.0254	2.0640	9.27	110.6	78.1	7.06	0.12	UH
					Mean:	**7.06**		
9202P, J = 1.586 X 10^{-3}, single sanidine crystals and # = 19 sanidine crystals								
2.216	0.0130	0.3390	10.5	216.5	93.0	6.33	0.11	UH
2.250	0.0877	0.7180	4.77	32.0	89.1	6.43	0.22	UH
2.265	0.0142	0.2520	7.16	197.8	94.1	6.47	0.29	UH
2.271	0.2618	1.2870	4.33	10.7	84.0	6.49#	0.20	UH
					Mean:	**6.43**	**+/- 0.07**	

Appendix K: Geochronology of the Bearhead Rhyolite From Previous Studies

Sample	Rock Type	Material Dated	Method	Age (Ma)	1σ
Rhyolite of Lower Peralta Canyon[1]	BHR	sanidine	$^{40}Ar/^{39}Ar$	6.91	0.06
2	BHR	unknown material	K/Ar	5.8	[illegible]
F82-77[3]	BHR	whole rock	K/Ar	6.2	
GF82-117[3]	BHR	whole rock	K/Ar	6.[illegible]	
GF82-1[3]	BHR	whole rock	K/Ar		0.[illegible]
4	BHR	unknown material	K/Ar		0.1
Corresponds to sample SCC or SBC from this study[5]	BHR	unknown material	K/Ar		0.2
F83-19[3]	BHR	whole rock	K/Ar	[illegible].1	0.4
2	BHR	unknown material	K/A[illegible]	7.5	0.3
JG80-47c[3]	BHR	whole rock	K[illegible]	8.7	0.7
Tuff of Canada Canada[6]	PT	sanidine	[illegible]	6.75	0.09
Tuff of Canada Canada[5]	PT	sanidine		6.79	0.05
Tuff Epsilon[7]	PT	sanidine	[illegible]r	6.81	0.02
Tuff of Colle Canyon[6]	PT	sanidine	[illegible]Ar	6.86	0.13
Tuff of West Mesa[6]	PT	sanidi[illegible]	[illegible]/^{39}Ar	6.96	0.10

[1]McIntosh and Quade (1995)

[2]Vainman and Baldridge (unpublished, 1985 in Gardner et al., 1986)

[3]Gardner and Goff (1984

[4]Gardner and Goff (unpu[illegible], 1985 in Gardner et al., 1986)

[5]Silberman et al. (written co[illegible]munication, 1976 in Leudke and Smith, 1

[6]McIntosh and Quade (19[illegible])

[7]McIntosh (unpublished from G.A. Smith, personal communication)

APPENDIX L

$^{40}Ar/^{39}Ar$ Sample Preparation

$^{40}Ar/^{39}Ar$ dating was completed at the University of Houston and New Mexico Institute of Mining and Technology. The $^{40}Ar/^{39}Ar$ analysis portion of the jaw-crushed sample was sieved and the fraction from 0.25 to 0.60 mm in diameter was reserved. Around 30 to 40 unaltered sanidine crystals were picked from the reserved fraction and washed in an ultrasonic bath of 1 M HF for 30 minutes to remove groundmass and specifically, glass. The crystals were then rinsed 3 times with distilled water and left to dry in a fume hood for 24 hours. The crystals were packaged in an aluminum foil capsule (averaged 3 mm height) and sealed in a 6 mm ID evacuated pyrex tube. Neutron fluence monitors (Australian National University 92-176, Fish Canyon Tuff sanidine) were placed within the tube at 6 mm intervals. Synthetic K-bearing glass (obtained from B. Turrin, U.S. Geological Survey) and optical grade CaF_2 were also included to monitor neutron induced argon interferences from K and Ca, respectively. The filled tubes were then packaged in an Al container for irradiation at the University of Michigan Ford Reactor. Samples were irradiated in two tubes for 10 hours in the L67 position on the core edge of the 1 MW TRIGA type reactor.

University of Houston Laboratory Methods

Irradiated crystals together with CaF_2 and K glass fragments were placed in a Cu sample tray in an ultrahigh vacuum extraction line and were fused using a 10 W CO_2 laser. Correction factors for interfering neutron reactions on K and Ca were determined by repeated analysis of K glass and CaF_2 fragments. Measured $(^{40}Ar/^{39}Ar)_K$ values were 0.06884 ± 0.00039. Ca correction factors were $(^{36}Ar/^{37}Ar)_{Ca} = 0.0002311 \pm 0.0000087$ and $(^{39}Ar/^{37}Ar)_{Ca} = 0.0007173 \pm 0.0000198$. J factors were determined by fusion of 3-7 (most frequently 4) individual crystals of Fish Canyon Tuff 92-176 sanidine, which gave reproducibility of ± 0.3 to 1.0 % (ave. ± 0.5 %) at each standard position. Variation in neutron flux along the 80 mm length of the Si irradiation tubes was ~ 3.1 % for the first tube and 4.4 % for the second. An error in J of 0.5% was used in age calculations. No significant neutron flux gradients were present within individual packets of crystals, as indicated by excellent reproducibility of the single crystal fluence monitor fusions.

Samples were positioned on a motorized sample stage and viewed during fusion by a CO_2 laser by a video camera system. Reactive gases were removed by a 50 L/s SAES getter prior to being admitted to a MAP 215-50 mass spectrometer by expansion. The relative volumes of the extraction line and mass spectrometer allow ≈80% of the gas to be admitted to the mass spectrometer. Peak intensities were measured using a Johnston electron multiplier by peak hopping through 7 cycles; initial peak heights were determined by linear regression to the time of gas admission. Mass spectrometer discrimination and sensitivity were monitored by repeated anlaysis of atmospheric argon aliquots from an on-line pipette system. Measured $^{40}Ar/^{39}Ar$ ratios ranged from 295.4 ±

to 299.3 ± 0.9 (1σ) with an average of 297.7 ± 0.98; thus discrimination corrections of 0.99684 ± 0.00074 to 1.00009 ± 0.00099 were applied to measured isotopic ratios. The sensitivity of the mass spectrometer was ≈ 5.1 X 10^{-17} mol/mV. Line blanks were checked after each 3 analyses and averaged 3.19 X 10^{-17} moles for mass 40, 9.40 X 10^{-17} moles for mass 39, 3.54 X 10^{-17} moles for mass 38, 3.85 X 10^{-17} moles for mass 37, and 1.98 X 10^{-17} moles for mass 36. Discrimination, sensitivity, and blanks were relatively constant over the period of data collection. Computer automated operation of the sample stage, laser, extraction line, and mass spectrometer as well as final data reduction and age calculations were completed using Macintosh-based software written by A. Deino (University of California, Berkley). An age of 27.9 Ma (Steven et al., 1967; Cebula et al., 1986) was used for the Fish Canyon Tuff sanidine 92-176 fluence monitor in calculating ages for samples.

New Mexico Institute of Mining and Technology Laboratory Methods

Sanidine phenocrysts were fused using a CO_2 laser. Reactive gases were removed by a 50 L/s SAES getter prior to being admitted to a MAP 215-50 mass spectrometer by expansion. The relative volumes of the extraction line and mass spectrometer allow ≈ 66% of the gas to be admitted to the mass spectrometer. Peak intensities were measured using a Johnston electron multiplier by peak hopping through 7 cycles; initial peak heights were determined by linear regression to the time of gas admission. Mass spectrometer discrimination and sensitivity were monitored by repeated analysis of atmospheric argon aliquots from an on-line pipette system. Measured $^{40}Ar/^{39}Ar$ ratios

ranged from 294.57 ± 1.39 to 293.3 ± 0.91 (1σ) with an average of 293.9 ± 1.15; thus discrimination corrections of 1.00171 ± 0.00078 to 1.00080 ± 0.00118 were applied to measured isotopic ratios. The sensitivity of the mass spectrometer was ≈ 3.0 X 10^{-17} mol/mV. Line blanks were checked after each 3 analyses and averaged 5.70 X 10^{-17} moles for mass 40, 4.0 X 10^{-17} moles for mass 39, 0.3 X 10^{-17} moles for mass 38, 0.8 X 10^{-17} moles for mass 37, and 2.6 X 10^{-17} moles for mass 36. Discrimination, sensitivity, and blanks were relatively constant over the period of data collection. Computer automated operation of the sample stage, laser, extraction line, and mass spectrometer as well as final data reduction and age calculations were completed using Macintosh-based software written by A. Deino (University of California, Berkley). An age of 27.9 Ma (Steven et al., 1967; Cebula et al., 1986) was used for the Fish Canyon Tuff sanidine 92-176 fluence monitor in calculating ages for samples.

Appendix M: Partition Coefficients for Rhyolite Petrogenetic Modeling

Element	Quartz	Sanidine	Plagioclase	Biotite	Zircon	Allanite	Apatite	Magnetite
Sc	0.00	0.03	0.17	15.50	68.70	49.40	0.00	8.90
Rb	0.00	0.31	0.024	5.30	0.00	0.00	0.00	0.00
Sr	0.00	4.00	24	0.53	0.00	100.00	2.00	0.15
Y	0.00	0.10	0.07	1.00	60.00	100.00	40.00	1.00
Zr	0.00	0.05	0.36	1.80	6400.00	2.00	0.10	8.00
Cs	0.00	0.008	0.05	2.40	0.00	0.00	0.00	0.00
Ba	0.00	10.00	3.5	3.70	0.00	0.00	2.00	0.00
La	0.00	0.067	0.26	3.55	16.90	2362.00	20.00	26.00
Ce	0.00	0.027	0.14	3.49	16.80	2063.00	35.00	22.90
Sm	0.00	0.0025	0.021	1.76	14.40	756.00	63.00	12.49
Eu	0.00	5.1	4.90	0.87	16.00	122.00	30.00	2.80
Tb	0.00	0.013	0.005	1.20	37.00	235.00	20.00	7.50
Yb	0.00	0.0025	0.15	0.69	527.00	24.50	25.00	1.00
Lu	0.00	0.003	0.12	0.80	642.00	22.00	25.00	0.91
Hf	0.00	0.020	0.096	0.68	3742.00	9.80	0.10	1.80
Ta	0.00	0.0007	0.13	1.30	47.50	1.90	0.00	1.13
Th	0.00	0.0030	0.002	1.74	76.80	420.00	2.00	13.10
U	0.00	0.002	0.15	0.19	340.50	14.00	0.00	0.21

Higuchi and Nagasawa (1969); Schnetzler and Philpotts (1970); Nagasawa and Schnetzler (1971); Arth (1976); Mahood and Hildreth (1983); Michael (1983); Nash and Crecraft (1985); Stix and Gorton (1990).

VITA

Graduate College
University of Nevada, Las Vegas

Leigh Justet

Address:
8373 Yamhill Street
Las Vegas, Nevada 89123

Degrees:
Bachelor of Science, Geoscience, 1996
University of Nevada, Las Vegas

Special Honors:
Barrick Fellowship
EPSCoR/WISE Scholarship
DoE/EPSCoR Young Scholar
Bernada E. French Scholarship
Robert Orr Scholarship in Mineralogy
UNLV Alumni Scholarship

Publications:
Using the geochemistry of the Callahan Chert, Callahan, CA to indicate its deositional environment, in prep.

Effusive eruptions from a large shallow magma chamber?: The geochronology and geochemistry of the Bearhead Rhyolite, Jemez volcanic field, New Mexico, in prep.

Thesis Title: The geochronology and geochemistry of the Bearhead Rhyolite, Jemez volcanic field, New Mexico

Thesis Examination Committee:
Chairperson, Terry L. Spell, Ph. D.
Committee Member, Eugene I. Smith, Ph. D.
Committee Member, Rodney V. Metcalf, Ph. D.
Graduate Faculty Representative, Kathleen A. Robins, Ph. D.
Thesis Reader, Philip R. Kyle, Ph. D., New Mexico Institute of Mining and Technology